Chemical and Biochemical Analysis Using Scanning Force Microscopy

Hajime Takano, Jeremy R. Kenseth, Sze-Shun Wong, Janese C. O'Brien, and Marc D. Porter*

Ames Laboratory—USDOE, Microanalytical Instrumentation Center, and Department of Chemistry, Iowa State University, Ames, Iowa 50011

Received February 24, 1999 (Revised Manuscript Received June 3, 1999)

Contents

* To whom correspondence should be addressed. Phone: (515) 294-6433. (Fax) 515-294-3254. E-mail: mporter@porter1.ameslab.gov.

I. Introduction

Like all essential sciences, analytical chemistry continues to reinvent itself. Many of the recent breakthroughs, several of which are described in this thematic issue of the Journal, are a direct result of improvements in instrumentation (e.g., optical[1−13] and electrochemical hardware[14−21]), the advent of new materials (e.g., nanoparticles[22−30]), or the development of methods to manipulate and characterize ever smaller-sized samples (e.g., miniaturized analytical hardware[31−38]). These advances are not only pushing analytical figures of merit (e.g., sensitivity, limits of detection, and analysis time) to new levels, but also enabling the analyst to characterize samples in environments (e.g., the intracellular media of a single cell and the local order of the architecture at the surface of reversed chromatographic stationary phases) not possible with the technology of only a few years ago.

Microscopy is also undergoing a remarkably innovative period, deriving in large part from the invention by Binnig, Rohrer, and Gerber of the scanning tunneling microscope in 1982[39] and the creation of the atomic force microscope by Binnig, Quate, and Gerber in 1986.[40] The atomic force microscope is also known as the scanning force microscope, and we will follow this nomenclature throughout this review. In their most established modes of operation, the scanning tunneling and scanning force microscopes have been applied to image the periodic two-dimensional architecture of surfaces. The early successes in the imaging of the atom-by-atom spacings of the Si(111)−(7×7) reconstruction,[40] Au(111),[41] and aromatic adsorbates,[42] the molecular spacing of organized organic films,[43,44] and the topography of DNA[45−50] are a few examples. These techniques have the ability to image, interrogate, and manipulate systems at length scales and interaction forces that control the organization of molecular assemblies. It is this ability that has captured the imagination of scientists around the world.

There are a number of techniques that have the capability to resolve the spatial chemical composition of interfaces (e.g., secondary ion mass spectrometry[51−53] and scanning electron microscopy[54,55]). These techniques, however, have operative resolutions at micrometer length scales. In addition, the chemical content provided by scanning tunneling microscopy (STM)- and scanning force microscopy (SFM)-based imaging has been limited until a few years ago largely to scanning tunneling spectroscopy (STS)[56] and

10.1021/cr9801317 CCC: $35.00
Published on Web 09/04/1999

Hajime Takano is currently a Postdoctoral Associate working under the direction of Marc D. Porter at the Microanalytical Instrumentation Center, Ames Laboratory–USDOE at Iowa State University. He received his Bachelor of Engineering degree from the Tokyo Institute of Technology (TIT) in Japan in 1992 and his Master of Engineering degree from TIT in 1994. He received his Ph.D. in biomolecular engineering from TIT in 1997 under the direction of Masamichi Fujihira, where his thesis research involved the study of organic surfaces using friction force microscopy. While pursuing his Ph.D., he was a Research Fellow of the Japan Society for the Promotion of Science from 1995 to 1997. His research interests involve micro- and nanotribology, the study of molecular interactions and spontaneously adsorbed monolayers, and the development of novel liquid chromatographic techniques.

Jeremy R. Kenseth is a Ph.D. candidate in the Department of Chemistry at Iowa State University. He received his Bachelor of Science degree in chemistry from the University of Wisconsin–La Crosse in 1995 and was awarded the American Chemical Society Outstanding Senior Chemistry Major Award, La Crosse–Winona Section. His doctoral research in the lab of Dr. Marc Porter has focused on the characterization and applications of spontaneously adsorbed monolayers of sulfur-containing molecules at gold surfaces using infrared spectroscopy and scanning probe microscopy. Recent work has involved the development of miniaturized immunodiagnostics utilizing scanning probe microscopy. He was the recipient of a 1998 Phillips Petroleum Research Fellowship.

near-field scanning optical microscopy (NSOM).[57−60] Both techniques have proven invaluable in a wide range of investigations. However, STS requires a conductive substrate for electron tunneling, and NSOM is applicable only to samples with large optical cross-sections. Because the origins of many macroscopic phenomena in the life, physical, and analytical sciences (e.g., protein folding, heterogeneous catalysis, and chemical separations) are controlled by the molecular level interactions at condensed-phase interfaces, efforts in several research laboratories[49,50,61−64] have explored the merits of SFM as a tool for surface chemical analysis.

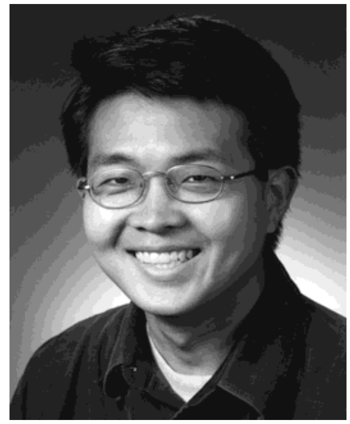

Sze-Shun (Season) Wong is currently a Ph.D. candidate in analytical chemistry working under the direction of Marc D. Porter at Iowa State University. He received his B.S. in chemistry and environmental studies from Bemidji State University in Bemidji, MN, in 1994. His thesis research focuses on high-resolution compositional mapping of monolayers and polymer films using scanning force microscopy and the characterization of mixed monolayers using electrochemistry and vibrational spectroscopy.

Janese C. O'Brien is currently a Ph.D. candidate in analytical chemistry working under the direction of Marc D. Porter at Iowa State University. She received her B.S. degree in chemistry from Creighton University in Omaha, NE, in 1993 and her M.A. in chemistry from the University of South Dakota in Vermillion, SD, in 1995. At Iowa State, she has been the recipient of a graduate research fellowship sponsored by Phillips Petroleum and the Kenan Award sponsored by Union Carbide. Her thesis research focuses on the design of miniaturized bioanalytical sensor platforms for interrogation by scanning probe microscopy and the characterization of electrically conductive sol–gels derived from transition metal alkoxides.

The following sections in this paper review the developments of this emerging characterization technique. For this purpose, the remainder of the review is divided into four sections. The first section overviews fundamental issues in SFM-based analysis, including instrumentation, methods for tip modification, and substrate preparation. The next section describes how SFM has been applied to chemical analysis, using an idealized force curve as a backdrop to illustrate various forms of chemical analysis performed in the approach and retraction portions of the curve. Compositional mapping using adhesion, friction, and tapping mode imaging are also discussed. The third section explores how SFM can be used as an analytical tool in the biochemical arena. This section parallels the previous one in that adhesion, friction, and tapping mode imaging are featured. However, this section adds topography as a detection

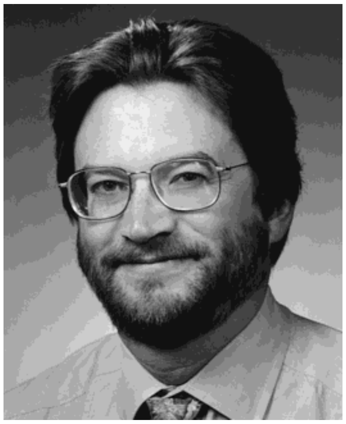

Marc D. Porter is currently a professor of chemistry at Iowa State University and is the Director of its Microanalytical Instrumentation Center. He received B.S. and M.S. degrees in chemistry from Wright State University in 1977 and 1979, respectively. After an industrial stint, he studied under the guidance of Professor Ted Kuwana at The Ohio State University and obtained his Ph.D. in analytical chemistry in 1984. His graduate work focused on new ways to characterize electrode materials. He then joined the research group guided by Dave Allara at Bell Communications Research as a postdoctoral associate and explored structural and electrochemical issues in self-assembled monolayers. His research interests include surface analytical chemistry, monolayer assemblies, chip-scale instrumentation, analytical separations, bioassays, and chemically selective microscopies.

modality in that changes in the size and shape of an adsorbed analyte can be exploited as a means for identification and quantitation. This intriguing concept is also highlighted in the fourth and last section by discussing the advances in hardware that are needed and being developed to enhance the utility of SFM as a technique in the analytical sciences.

II. Fundamental Issues in SFM

A. Instrumentation

A number of excellent reviews of SFM are available, ranging from broad introductions to focused discussions of fundamental principles and instrument design issues.[65−67] This section briefly introduces the instrumental and operational aspects of SFM, building a basis for how the different imaging mechanisms can be exploited in analysis.

1. Hardware

A scanning force microscope consists of four major components: a cantilever-mounted tip, a piezoelectric micropositioner, a cantilever deflection sensor, and an electrical feedback mechanism for the micropositioner. The most popular mode of detecting cantilever deflection, which is depicted in an instrument schematic in Figure 1A, uses an optical lever and a quadrant, position-sensitive photodiode. This detection system can be used to follow the normal displacement (vertical motion) and the torsion (lateral motion) of the cantilever simultaneously. In Figure 1B, a scanning electron micrograph of a commercially available, microfabricated silicon nitride (Si_3N_4) cantilever with a pyramidal tip is shown. Since normal spring constants (k_N) for cantilevers are 0.01−100 N/m and instrumental sensitivities for normal deflection are ~0.01 nm, the corresponding limits in force

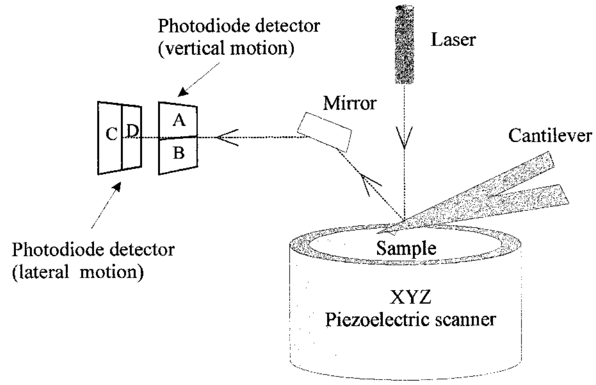

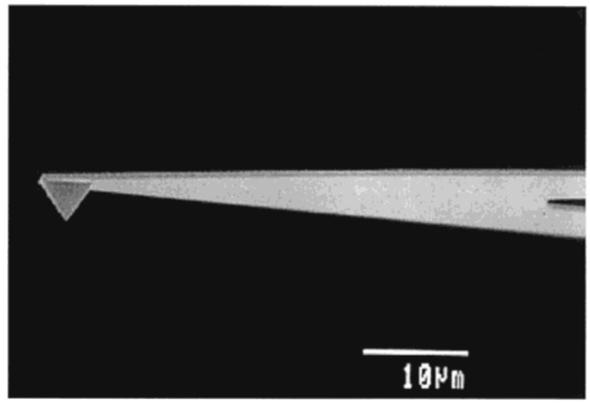

Figure 1. (A, top) Schematic of the principal components for an optical lever type scanning force microscope. The laser beam is reflected off of the back of the cantilever onto a quadrant, position-sensitive photodiode. The normal bending and the torsion of the cantilever can be detected simultaneously. (B, bottom) A scanning electron micrograph of a Si_3N_4 cantilever with a pyramidal tip.

detection are 10^{-13}−10^{-8} N.[66] These limits reflect a combination of the thermal excitation of the cantilever as well as optical and electrical noise.

2. Measurement Modes

One of the valuable approaches for chemical and biological analysis by SFM is characterization of the force−distance curve, often referred to simply as the force curve. Figure 2 shows idealized force−distance curves in the presence (A) or absence (B) of tip−sample adhesion. The force curve is obtained by plotting the vertical displacement of the cantilever, which is monitored by the vertical segments of the photodetector, as a function of the separation distance between the tip and the sample. The cantilever displacement (Δz) is then converted into force (F_N) according to the relationship

$$F_N = k_N \Delta z \quad (1)$$

The force curve is an approach−retract cycle where the sample first approaches the tip (i.e., the sample moves in a positive z-direction) and is subsequently retracted from the tip. Details of force curve analysis are described in a later section.

The most popular instrumental mode of the scanning force microscope is the contact mode (Figure 3A), where the tip is brought into physical contact with the sample. The micropositioners are slaved to the

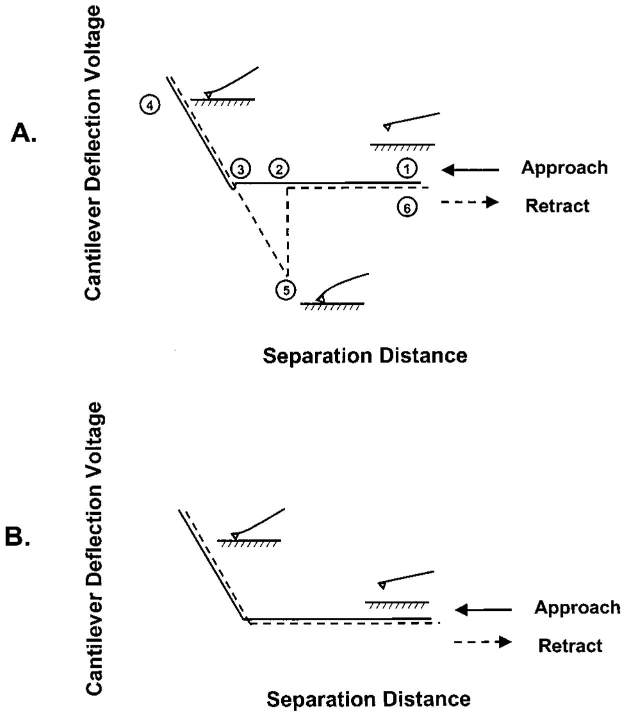

Figure 2. (A) An idealized force−distance curve for an adhesive contact. (1) At large tip−sample separations, there is no detectable interaction force. (2) As the separation distance decreases (i.e., the sample moves in the positive *z*-direction), various long- and short-range forces can be measured as summarized in Table 1. (3) At some separation, the gradient of interaction energy exceeds the restoring force of the cantilever and the tip jumps to contact with the surface. (4) As the sample moves further in the positive *z*-direction, a positive linear cantilever deflection is observed as the tip and sample move together. As the sample moves in the negative *z*-direction, a similar cantilever deflection line is traced as the tip and sample remain in contact. (5) As the tip moves further in the negative *z*-direction, the restoring force exerted by the bending of the cantilever overcomes the adhesive force of the tip−sample microcontact and the tip breaks away from the sample. (6) The cantilever has returned to its noninteracting, equilibrium position. (B) An idealized force−distance curve obtained in the absence of any tip−sample interactions (e.g., in liquid).

feedback electronics to maintain a preset imaging parameter (e.g., force) which is monitored by the vertical deflection sensor while the sample is scanned under the tip, or vice versa. Two-dimensional plots of the feedback signal are then used to develop a topographic image of the sample. A map of surface composition, for example, can be constructed if there are differences in topography that can be directly correlated with compositional and/or other structural expectations.

To this point, we have focused on imaging mechanisms that rely on deflections of the tip with respect to the surface normal. However, the force generated as the tip is moved laterally across the sample surface can also be used as an imaging mechanism. The top of Figure 4 represents how an optical beam deflection system can detect the torsional deflection of a cantilever. The lateral force applied to the tip causes a torsion of the cantilever, which is monitored by the lateral segments of the photodetector. Thus, the detector sensitivity to the twist of the cantilever,

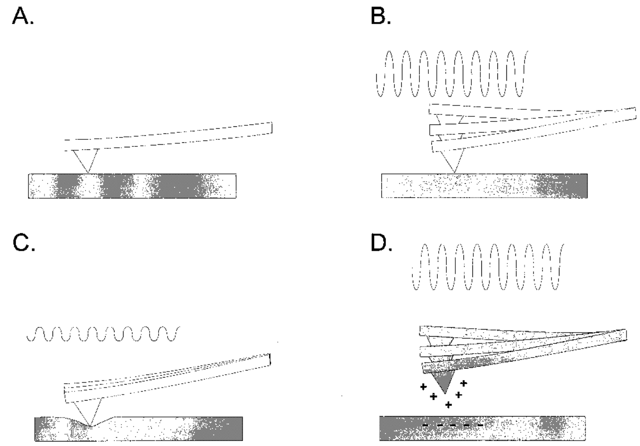

Figure 3. Modes of operation for SFM. (A) Contact mode detects topography, adhesion, elasticity, and friction of a sample. (B) Tapping mode is sensitive to topography and adhesion of the sample. (C) Force modulation mode is responsive to the elasticity and viscosity of the sample. (D) Electric force mode measures the potential difference between the tip and sample and the dielectric properties of the sample.

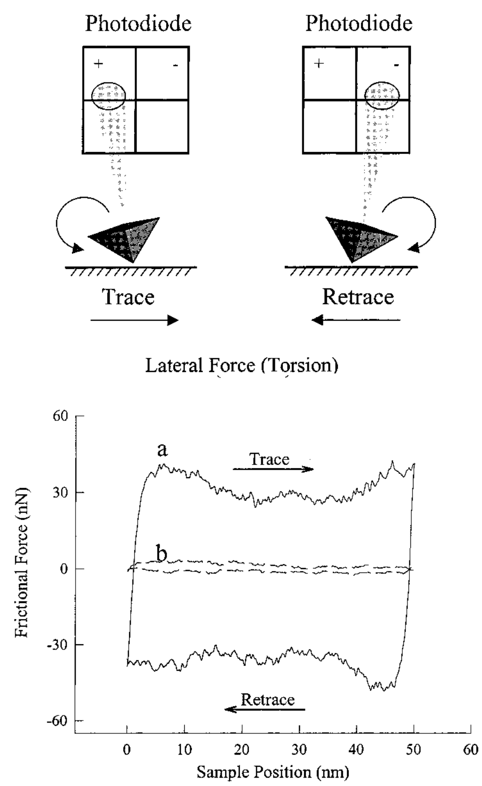

Figure 4. Friction force measurements with SFM. (Top) As the sample is scanned laterally, the cantilever experiences a torsion that deflects the laser beam laterally. (Bottom) Friction loops collected using an uncoated Si_3N_4 tip for (a) a bare Au(111) surface and (b) an octadecanethiolate (ODT)-modified Au(111) surface. The friction at ODT/Au(111) is considerably less than that at uncoated Au(111), indicative of the lubrication properties of the adlayer.

coupled with the torsional force constant of the cantilever (k_t, typical value 1−500 N/m), can be correlated with the friction force at the tip−sample microcontact.[67,68] A plot of torsion with respect to the movement of the sample when scanned against the major axis of the cantilever results in a "friction loop". Friction loops for a bare gold surface and gold modified with an octadecanethiolate monolayer are shown in the bottom of Figure 4. The difference in the magnitudes of the trace−retrace plots is indicative of the energy dissipated in the scan; the smaller difference of the thiolate-coated gold is diagnostic of the boundary lubricant properties of the long-chain monolayer.

Although friction-based SFM has been used extensively for chemical mapping analysis, there are occasions where lower imaging forces, such as in the characterization of soft biological and polymer materials, are required. That is, highly compliant samples may be destructively and therefore unreliably imaged at the shear forces operative in contact mode imaging. Tapping mode SFM (TM-SFM) (Figure 3B) reduces this problem by periodically "tapping" the surface with the tip as the sample is translated under the tip.[69−71] In this mode, the oscillation of the cantilever is driven at or near its resonant frequency via a piezoelectric crystal. The changes in oscillation amplitude during scanning are used to map topography. Moreover, the phase changes of the oscillation during a scan can be recorded as phase images that are related to variations in adhesion, friction, and/or viscoelasticity.[71−73]

Another SFM technique that has gained popularity is known as force modulation microscopy (FM-SFM) (Figure 3C).[74−76] In FM-SFM, a small vertical oscillation is imposed on the cantilever or sample during scanning at oscillation frequencies significantly smaller than the resonant frequency of the cantilever. In contrast to tapping mode SFM, the vertical position of the sample is modulated without breaking contact with the tip. The resulting deflection of the cantilever is then correlated with the elasticity of the tip−sample microcontact, noting that the oscillation can be modulated with a preselected amplitude and frequency depending on the elasticity of the sample.[77] Since elasticity may be affected, for example, by lateral differences in the density of a coating, it may be possible to utilize this imaging mechanism as a mapping tool, recognizing that the interpretation of the image requires considerations of a complex combination of viscoelasticity and adhesion forces.

The electric force mode of SFM is another means to map surface composition.[78−84] In its earlier form,[78,84,85] which is depicted in Figure 3D, a dc voltage is applied across a conducting tip and sample. When the tip is brought close to the sample ($\sim$100 nm), an attractive electrostatic force is induced between the tip and sample. This force can be detected simply as a cantilever deflection or as a shift in the resonance frequency of an oscillating cantilever. The magnitude of this force is a function of the potential difference and the dielectric constant of the resulting capacitor. Therefore, changes in the dielectric constant resulting from differences in the local composition of a coating can be used as a contrast mechanism for mapping.

There are also hosts of other SFM imaging modes where the tip is oscillated near resonance and changes in the amplitude, frequency, and phase of the oscillation are monitored as a function of tip−sample separation.[86,87] These three measurables are influenced by the interaction force and its gradient between the tip and sample. Magnetic force microscopy,[88−90] noncontact mode scanning force microscopy,[91−93] and some variants of electric force microscopy[78,79,84] rely on this transduction mode. Access to these interactions and material properties offers the surface scientist an unprecedented view of the surface before, during, and following modifications with organic films.

3. Resolution Issues

Each pixel in a SFM image reflects the deflection of the cantilever that is induced by the collective interactions of tens to hundreds of atoms, as described by the Hertz and Johnson, Kendall, and Roberts (JKR) theories[66,94] of continuum mechanics. This situation is the result of the size of the tip−sample microcontact, the dependence of the contact area on F_N, the size and shape of the tip terminus, and the elasticity of the sample. Organic adlayers can be particularly problematic because they are much more compliant, i.e., have a lower Young's modulus, than most inorganic materials. Thus, resolution is affected by a complex mixing of tip and sample properties. Achieving the highest possible resolution, usually a few nanometers, therefore requires sharp tips, low loads (F_N), and relatively rigid films, although in many cases atomic or molecular resolution has been demonstrated.[91−93,95−97]

4. Calibration

To ensure that the surface features and forces recorded in SFM experiments are accurate and precise, the movement of the three-dimensional piezoelectric microactuator, the spring constants of the cantilever, and the sensitivity of the photodiode must be calibrated. As with all analytical methods, the more careful the calibration, the more reliable the results. For the microactuators, calibration is usually accomplished by imaging a reference surface having features of precisely known dimensions.[65] Microgrids as well as materials such as mica, highly ordered pyrolytic graphite (HOPG), and $SrTiO_3$ crystals[98] have been used for the calibrations of the three working axes of the piezoelectric microactuator.

The values for the spring constants (k_N and k_t) must also be carefully determined. Most common SFM experiments utilize commercially available microfabricated silicon or silicon nitride cantilevers. One may calculate the normal and torsional spring constants from geometric considerations of the cantilever and the mechanical properties of the cantilever material itself.[99−102] This analysis must account not only for the possible differences in the mechanical properties of microfabricated materials with respect to the bulk material,[67,103] but also for the thickness and mechanical properties of the metal coating employed to increase optical reflectivity.[103,104] For the commonly used V-shaped cantilevers, some approximation of the cantilever geometry[105−107] (e.g., the parallel beam approximation[105,108]) or more exacting numerical methods have been used.[103,109] Even with rectangular-shaped cantilevers, knowledge of critical dimensions (e.g., cantilever thickness and tip height) is needed for an accurate determination of the spring constants.[110]

The normal spring constant can also be determined experimentally. Approaches include observing shifts in the resonance frequency of a mass-loaded cantilever,[111] measuring the resonance frequency of the thermally induced vibration of a free-standing cantilever,[104,112] or determining the resonance frequency of a mechanically driven cantilever.[103] Estimations of a normal spring constant can also be developed by the direct determination of the cantilever deflection under a known load.[67,108] These approaches can also be used to obtain information about the mechanical properties (e.g., Young's modulus) of the cantilever material[103] as well as the thickness of the cantilever.[110]

In addition to the above, the photodiode sensitivities must be calibrated in instruments employing an optical lever detection system. The photodiode sensitivity to the normal deflection of the cantilever can be determined by analyzing a force−distance curve measured with the tip in contact with a hard (i.e., noncompliant) material. Although elastic deformation at the tip−sample microcontact may be present, the contribution of this effect to normal photodiode sensitivity is usually negligible if the normal spring constant is small.

Calibration of the photodiode lateral sensitivity to the torsion of the cantilever is more challenging.[67,68] As a rough approximation, the photodiode lateral sensitivity can be estimated from the photodiode normal sensitivity, assuming that equal changes of the reflected laser beam by bending and torsion of the cantilever result in equal changes of the normal and lateral photodiode signals.[102] The photodiode lateral sensitivity can also be measured by optical methods described by Putman[113] and Marti[114] and from the static friction region of a friction loop. We note that when friction loop methods are employed, lateral elastic deformation at the tip−sample microcontact[115,116] or elastic deformation of the tip itself[115,117] often degrades the calibration. To circumvent such issues, alternative calibration approaches have been developed which are independent of photodiode lateral sensitivity and lateral spring constant.[67,68] For example, by analyzing the friction measured on a wedged surface,[68] the friction coefficient can be directly calculated independent of these variables.

Finally, since the size and shape of the tip play a major role in defining the area of the microcontact, techniques for such an evaluation are also needed to analyze SFM data. These methods include the direct imaging of the tip with an electron microscope, as well as using the tip to image surfaces containing features with sharp contrast[118,119] such as the surface of $SrTiO_3$ crystals.[98,120] Other methods rely on reconstruction of the tip from images obtained of uniform latex spheres[121] or colloidal gold clusters.[122]

In view of the complications in calibration, we recommend the use of the same tip in instances where the variability in the contacts between samples may be problematic. It is also valuable to use samples patterned with an internal standard to simplify some characterizations. Nevertheless, a successful comparison of results from different laboratories requires strict attention to calibration procedures.

B. Tip Modification

Although still in its adolescence, the modality of SFM has already greatly expanded beyond its original function of topographic imaging. These variants are being applied to a wide array of areas, ranging from biology to semiconductors, data storage media to polymers, and integrated optics to lithography. The key to success, however, often lies with the quality (e.g., radius of curvature, hardness, and surface composition) of the tip. With the sophisticated semiconductor technology of today, tips can be mass produced with a fair degree of consistency in size and shape. Most commercially available tips have a radius of 30−50 nm and are made from silicon or silicon nitride (Si_3N_4). Typical Si/Si_3N_4 tips have a pyramidal geometry with an aspect ratio of 1−2. While important advances have been achieved by coating tips with hard materials such as nanocrystalline diamond,[123] many users are finding that these improvements do not adequately meet their research needs. This situation has led several laboratories to investigate avenues to enhance imaging capabilities by altering the surface composition of the tip.

The basis for altering the surface composition of a tip recognizes the importance of intermolecular forces on the outermost few angstroms of the tip−sample microcontact in SFM imaging. Most commercially available tips, however, have surfaces that are poorly controlled from a compositional perspective. This lack of control has three potential consequences. First, the surface of silicon-based tips has a large number of silanol groups, which results in a surface that can be readily altered by the adventitious adsorption of contaminants. This contamination can lead to tips with a varied surface composition. Second, uncoated tips may change shape because of wear under prolonged usage. Modifications that could reduce wear, and thus improve the quantitative repeatability of a characterization, would clearly be advantageous. Third, because the surface of an uncoated tip is hydrophilic, the strong adherence of the tip to a delicate, hydrophilic surface may damage the sample. This problem is usually encountered when the loosely connected network of many biological samples is imaged. These types of samples usually have a highly hydrophilic superstructure at their surface, which results in a strong adherence at the tip−sample microcontact and complicates the manipulation and maintenance of the applied load. Seizing control over the surface composition of the tip therefore represents an important and necessary development not only in improving the general reliability of the technique, but also in realizing new imaging concepts as well.

This section focuses on approaches for the modification of commercially available Si or Si_3N_4 tips. We note that other methods for fabricating tips with enhanced performance, such as successive reactive ion etching for high-aspect ratio tip shapes,[124] and

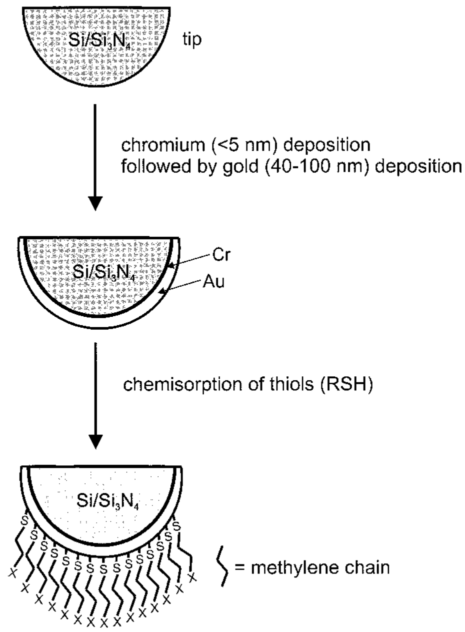

Figure 5. General scheme for tip modification using thiol-based monolayers chemisorbed on gold. The R in RSH represents an alkyl chain with terminal group X (X = CH_3, COOH, CH_2OH, NH_2, etc.).

micromachining of hollow metal tips for the many variants of SFM,[125] have been reported.

1. Alkanethiols

By far, the most popular approach to tip modification is through the immobilization of thiol-based monolayers on gold-coated tips.[85,126−128] While approaches to coating tips with polymeric materials have been reported,[129] polymer-coated tips are generally chemically and morphologically more heterogeneous than those modified with monolayer coatings such as "thiols on gold". The thiol-modification procedure is outlined broadly in Figure 5. The procedure involves the vapor deposition of a thin chromium adhesive layer (<5 nm) onto a tip followed by deposition of a thicker gold layer (usually 40−100 nm). The gold-coated tips are then immersed in a dilute (0.1−1.0 mM) thiol solution which yields a covalently bound monolayer that is the thiolate analogue of the thiol precursor.[130] These modified tips are chemically stable and mechanically robust. Indeed, an investigation of the lubrication and wear properties of such tips clearly demonstrated a lower susceptibility to wear than uncoated Si_3N_4 tips.[131] In addition, thiols with a variety of terminal functionalities are commercially available or readily synthesized. As expected, the ease and flexibility of this derivatization process has led to its extensive use in tip modification.

A potential disadvantage of this type of modification is that the radius of the tip can significantly increase because of the need for metallization. This increase may lead to a reduction in lateral resolution. Careful control of the deposition rate is therefore important. During metallization, one must also avoid heating the cantilevers because the differences in the thermal expansion coefficients of gold and Si/Si_3N_4 may cause irreversible bending of the cantilever.[128] Hadziioannou and co-workers have addressed this

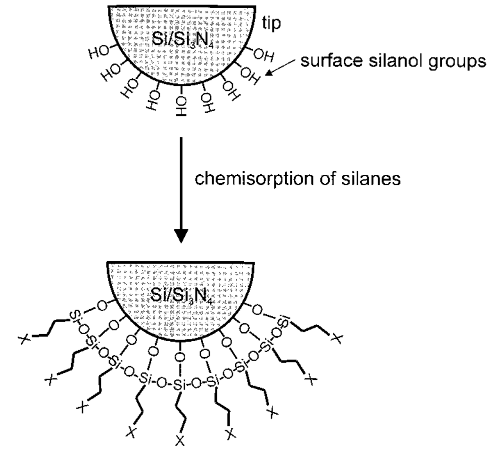

Figure 6. General scheme for tip modification using silane-based self-assembled films where X represents different terminal groups.

problem by coating both the front and back of the tips.[128] In a different approach, Beebe and co-workers removed the gold coating on commercial cantilevers and redeposited gold only at the end of the V-shaped legs.[132] This reduced the bending of the cantilever while retaining the desired optical reflectivity.

2. Organosilanes

In addition to derivatizations using spontaneously adsorbed thiols, tips can be modified with organosilane ($R_nSi(Y)_{4-n}$) adlayers (e.g., alkyltrichlorosilane (n = 1, Y = Cl) or alkyltrialkoxysilane (n =1, Y = OR)), which directly couple to the surface silanol groups of a Si or Si_3N_4 tip.[133−138] This process, illustrated in Figure 6, closely follows that used for the thiol-based modification but is often preceded by a tip-cleaning step (e.g., ozone plasma[139]). The formation of organosilane films begins with the hydrolysis of the silane precursors. Subsequent condensation reactions between the precursors and surface silanols result in the formation of a two-dimensional lateral network comprised of Si−O−Si bonds. After drying or curing, the silane film is covalently attached to the tip with a concomitant loss of water. This modification method changes the surface chemistry of a tip without the need for metallization.[134,138]

When compared to thiols, organosilanes are not used as extensively for tip modification.[140] This situation reflects a combination of problems with the silanization process, including the sensitivity of chlorosilanes to moisture as well as the difficulty in controlling the polymerization process and film thickness.[130,139] However, under the appropriate preparative conditions, adlayers that approach the degree of ordering envisioned for the thiol system can be realized. In fact, the first reports using chemically modified tips in SFM were based on the silane system.[133,135]

3. Colloidal Particles

Another popular way of constructing functionalized tips is by attaching micrometer-sized spheres directly onto the tip. This concept was first demonstrated by Ducker and co-workers who epoxied silica microspheres to tips with the aid of micromanipulators and

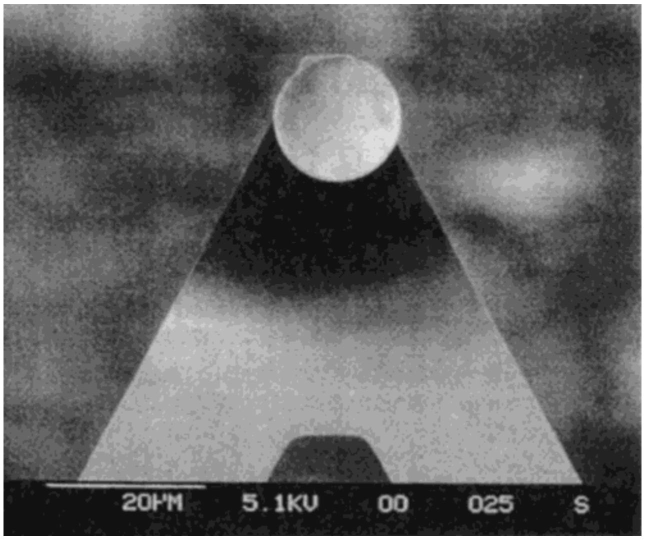

Figure 7. Scanning electron micrograph of a 16 μm polystyrene sphere attached to a SFM cantilever. Reprinted with permission from ref 144. Copyright 1993 American Chemical Society.

either an optical microscope for micrometer-sized spheres or a scanning electron microscope for smaller-sized spheres.[141,142] Kim and co-workers have reported a similar concept using C_{60}[143] as have several other groups using polymeric particles.[144,145] Figure 7 presents a scanning electron microscopy (SEM) image of a 16 μm polystyrene microsphere affixed to the end of a cantilever.[144]

At present, silica microspheres[146,147] appear to be the most favored of the particle-based modifications. This status is because (1) the surfaces of silica microspheres are relatively smooth, (2) the surface chemistry of silica is well developed, and (3) the silica surface can be readily modified. The last reason is of particular importance in biological investigations because of the wide range of covalent coupling reactions that can be used to secure peptides, proteins, oligonucleotides, and other biological materials to the surface of the sphere.

C. Substrate Preparation

The substrate plays a critical role in the successful application of SFM as an analytical tool. In this section we discuss the properties of an ideal SFM substrate and then briefly describe the preparation and attributes of several of the most commonly used substrates.

An ideal substrate should be chemically inert in the laboratory ambient, easily prepared, relatively inexpensive, readily modified by a wide range of derivatization methods, and amenable to long-term storage.[148,149] For most analytical purposes, an ideal substrate should also be composed of large, atomically flat domains. The last attribute is significant because molecular entities and other types of nanometer-sized objects can be easily obscured when a surface with a roughness on the same scale is imaged.

The importance of a smooth substrate has been documented in several recent investigations.[148−151] In our laboratory, the changes in surface topography (i.e., height) that arise from the specific binding of an antibody to a surface modified with an antigenic monolayer have predicated the need for an extremely flat surface.[152] Since changes in topography that result as a consequence of specific binding are on the order of a few nanometers, the ability to detect changes on this length scale would be compromised when using substrates with a roughness of comparable magnitude. The ability to produce substrates containing large domains with subnanometer roughness is therefore essential. Further details of this and other strategies for analysis using SFM that have comparable requirements are discussed in later sections.

1. Mica

One of the most common substrates utilized for SFM investigations is mica. Mica is extremely flat, having an average surface roughness on the order of a few angstroms over an area of a few square micrometers. It is also relatively inexpensive, and can be easily and routinely prepared. Mica therefore has several of the attributes of an ideal substrate, which have led to its use as a support for imaging a variety of molecules, ranging from DNA[153−155] to living cells.[156] However, mica is not readily modified which limits the scope of its applicability.

2. Gold

Gold, either as a thin-supported film or a bulk material, is another commonly used substrate.[53,131,157−166] Though more costly than mica, gold is remarkably inert in the laboratory ambient and can be readily derivatized by sulfur-containing compounds (e.g., alkanethiols) to create well-ordered architectures of varied composition, including those with terminal groups that can serve as coupling agents. Thin film substrates are generally prepared by vapor-depositing gold onto mica substrates,[150,166,167] which, after annealing at elevated temperatures ($\geq$300 °C), yields a roughness of only a few atomic layers that can extend hundreds of square nanometers. As expected, the deposition conditions and the duration and temperature of the annealing process play a strong role in determining the quality of the substrate.[168]

Although useful for many applications, gold surfaces with an even lower surface roughness and larger terrace size are often desired. A recently developed lift-off technique by Hegner and Wagner addresses this need.[148] This valuable development, depicted in Figure 8,[149] entails the deposition of gold onto a freshly cleaved mica substrate, which is then cut into small sections ($\sim$1 cm^2) and epoxied with the gold side down onto a glass or silicon substrate. The assembly is subsequently cured to form a mica/gold/silicon sandwich that is stable for several months. To expose the gold surface, the mica is removed either by using adhesive tape[148] or by immersing the sandwich into a solvent such as tetrahydrofuran.[149] Both processes expose the underlying gold surface that was templated during the deposition on the smooth mica surface. Therefore, the resulting gold surface is termed template-stripped gold (TSG).

A comparison of the surface formed by template stripping with that by the more conventional vapor deposition method is instructive. When prepared at

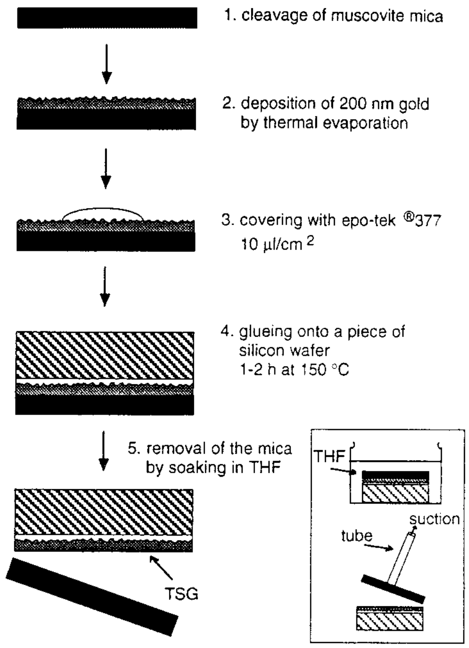

Figure 8. Procedure for preparing template-stripped gold. Reprinted with permission from ref 149. Copyright 1995 American Chemical Society.

deposition temperatures of 20−25 °C, the mean SFM-determined roughness of a TSG surface was 2.8 ± 0.1 and 3.2 ± 0.1 Å for scanned areas of 2.25 and 25 μm^2, respectively. The average terrace size of such surfaces was determined to be ∼50 nm by STM.[148] When deposited at 300 °C, the average terrace size increased to ∼500 nm by STM analysis, with an increase in SFM-determined mean roughness to 10.1 ± 0.6 and 11.4 ± 0.1 Å for 2.25 and 25.0 μm^2 scan areas, respectively. The difference in the roughness for the two different scan areas arises from a more proportionate contribution by grain boundaries to the larger area scans. In contrast, the surface prepared by the more standard vapor deposition approach at 20−25 °C had a mean SFM-determined roughness of 33.6 ± 0.4 Å over a scan area of 25 μm^2.

3. Silicon

Silicon is yet another substrate that is commonly employed in SFM investigations. Silicon, like gold and mica, is relatively inert in the laboratory ambient. While a vast literature exists on the modification of silicon with various silanes,[130] the resulting coatings are generally less ordered and their formation is less reproducible than their alkanethiol counterparts on gold. The poor reproducibility is due to, in part, the sensitivity of the silane precursors to water.

An approach that appears to address both issues entails the creation of hydrogen-passivated Si(111) surfaces, which are atomically flat and easily and reproducibly modified.[151] As characterized by STM, unmodified hydrogen-passivated Si(111) surfaces exhibit a mean roughness of 1.94 Å over a 4 μm × 4 μm area. After modification with a methyl-terminated octadecyl monolayer, the mean surface roughness was reported to be 1.59 Å for a 2 μm × 2 μm scan by SFM using a multiwalled carbon nanotube-modified tip.

4. Photolithography

In addition to the above attributes, another important issue when substrates are prepared for chemical analysis by SFM is the design of the chemical landscape. Techniques that provide for the control over the placement or delivery of chemical reagents and calibration standards onto discrete regions of a surface are critical. Ideally, this localization would be done within the typical scan area of SFM so that both reaction and calibration information can be gained in a single scan.

One method that provides for localization is photolithography. Photolithography involves the irradiation of a surface comprised of photolabile groups through a photomask, which chemically transforms the irradiated areas and results in a compositionally patterned surface. One of the more popular photolithographic systems in this area involves the photooxidation of alkanethiolate monolayers on gold.[53,164,169] With this system, ultraviolet radiation in the presence of oxygen converts the gold-bound thiolate to various oxygenated forms of sulfur (e.g., RSO_3^-).[170] These oxygenated forms of sulfur weakly adhere to gold and are readily rinsed from the surface with many organic solvents, such as ethanol, acetone, or tetrahydrofuran.

We have used transmission electron microscopy (TEM) grids as masks, where the mesh size of the grid defines the size and shape of the irradiated area. For example, irradiation of an octadecanethiolate (ODT)-modified gold surface through a 2000 mesh grid followed by ethanol rinsing creates bare gold squares 7.5 μm × 7.5 μm in dimension that are surrounded by intact ODT grids 5.0 μm wide.[152] These exposed gold squares can then be back-filled with an alkanethiol that has a different terminal group (e.g., a terminal group that can function as a coupling agent). In a parallel approach, Bhatia and co-workers exposed a glass substrate modified with a thiol-terminated silane to ultraviolet light to create surfaces that resisted protein adsorption because of the highly hydrated, anion-terminated groups formed from the photochemistry.[171,172] Ultraviolet light has also been used to remove non-thiol silanes from selective portions of a SiO_2 surface to create hydrophobic/hydrophilic surface patterns used to prepare two-dimensional antibody arrays.[173] In addition, photoactive cross-linking reagents can be used to pattern the spatial composition of a surface.[174−178] This approach has been employed for the generation of protein/enzyme nanostructures using an ultraviolet laser-generated interference pattern for the activation of photobiotin.[179] Although not extensively used at present, we expect a significant expansion in the use of this technology.[180]

5. Microcontact Printing

Another increasingly popular method for creating compositionally patterned surfaces is microcontact printing. This technique uses a custom-made polymer "stamp", usually prepared from poly(dimethylsiloxane) (PDMS), to deposit reagents onto localized areas of a surface. As originally described[181−186] and since extensively exploited,[187−189] microcontact printed surfaces are constructed by exposing a PDMS stamp to a concentrated (1−10 mM) ethanolic alkanethiol solution followed by drying under nitrogen and applying to a metal surface, generally gold. Upon contact, the alkanethiol is transferred to the gold surface, creating an alkanethiolate monolayer only in the regions of contact. If desired, the uncoated portion of the gold surface can then be back-filled with another alkanethiol by immersion into a dilute thiol solution,[182,183] or the unstamped regions can be removed by chemical etching[181] to expose the underlying substrate. In addition to gold, microcontact printing has been recently used to pattern a silver surface.[186]

Using conventional stamping techniques, feature sizes as small as 500 nm can be generated.[185] However, features ∼200 nm in size have been produced by using lateral compression. In the lateral compression technique, an "inked" stamp is placed in a vice and compressed to reduce the lateral dimensions of the relief structures on the stamp. The stamp is used while under compression to create features that are smaller than those originally created on the PDMS stamp. An example of such patterning is shown in Figure 9. A compressed stamp can also serve as a master for preparing a stamp with the same spatial definition as the compressed stamp.[184]

Microcontact printing has been used to pattern protein layers on glass,[190,191] for the creation of surfaces for the patterned formation of microcrystals or condensed vapors, and in several other applications.[182] Because of the relative ease of stamp preparation and the close correspondence of the features of the stamp to those on the master, we believe microcontact printing will become a standard methodology in this and other areas.

6. Microfluidic Networks

In addition to photopatterning and stamping protocols that provide for the placement of reagents and calibration standards onto surfaces, another method for delivering such materials to surfaces involves the creation of fluid microchannels.[192−197] Using elastomeric microchannels, Delamarche and co-workers have demonstrated the patterned delivery of immunoglobulins to discrete regions of a surface.[196,197] An array of 100 elastomeric channels 3 mm long and 3 μm wide that were separated by 0.8 μm was constructed to connect two pads serving as reservoirs for the chemical of interest. Such devices have been used to deposit immunoglobulins on various substrates at widths of 2 μm. Furthermore, channels of these dimensions consume only microliter quantities of solution, thereby minimizing the amount of sample required for array fabrication.

III. Chemical Analysis Using SFM

This part of the review is devoted to the contributions of SFM in the area of chemical analysis. This section first begins with a detailed discussion of an idealized force curve, setting the stage for the use of SFM as a chemical analysis tool. Examples are then discussed that highlight the many applications of force measurements to the chemical characterization of surfaces.

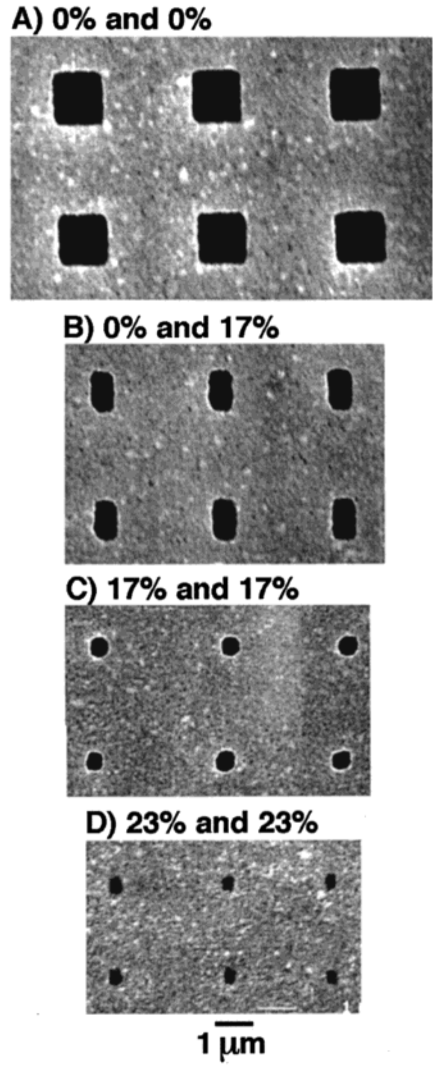

Figure 9. Scanning electron micrographs of Ag patterns (50 nm thick) that were fabricated with a PDMS stamp comprised of parallel line-shaped holes that had been compressed in the direction perpendicular to the lines. Each pattern was formed by printing twice with the direction of lines rotated by 90° before making the second print. The first number indicates the compressive strain in the vertical direction. The pattern was created by evaporating Ag onto the underlying substrate through the holes in the stamp. Reprinted with permission from ref 185. Copyright 1997 American Chemical Society.

A. Force Curve Measurements

A force curve is collected by monitoring cantilever deflection versus separation distance as the tip and surface are brought into contact and subsequently separated. The cantilever deflection can be converted to applied force through the cantilever spring constant, k_N, via eq 1. A force curve can be divided into several regions as shown in Figure 2A.

(1) The tip and sample are sufficiently separated such that there is no detectable interaction. At these separation distances, the cantilever is in its noninteracting equilibrium position.

(2) As the separation distance decreases, various long- and short-range forces, as summarized in Table

Table 1. Types of Interaction Forces and Interaction Distances in SFM

type	distance (nm)	note
long range		
electrostatic force in air	100	
double layer force in electrolyte solution	100	depends on electrolyte concentration
van der waals force	10	
short range		
surface-induced solvent ordering	5	depends on the molecular size of the solvent
hydrogen-bonding force	0.2	
contact	0.1	

1,[66] can induce a deflection of the cantilever. These forces include attractive/repulsive electrostatic interactions, which are the result of the electrical double layer formed in aqueous electrolyte, and van der Waals interactions. At very small separations in liquid media, surface-induced solvent ordering may be detected.

(3) As the separation distance decreases further, the gradient of interaction force exceeds the force constant of the cantilever and the tip jumps into contact with the surface.

(4) The tip and surface are in contact, inducing a positive deflection of the cantilever. It is in this region that elastic properties of the sample can be measured.

(5) Because of the adhesion between the tip and sample, a negative deflection of the cantilever is detected until the adhesive force is overcome by the restoring force of the cantilever and the contact ruptures. The magnitude of this negative deflection is related to the adhesion force, F_{ad}, of the microcontact. This adhesion is also referred to as rupture force or pull-off force.

(6) The tip and sample are sufficiently separated such that the cantilever returns to its noninteracting equilibrium position.

Figure 2A represents an idealized force curve when an adhesive contact is formed between the tip and sample (e.g., adhesion due to capillary forces when operating in air). On many occasions, there is no adhesion between the tip and sample, for example, when operating under liquid in the absence of specific tip−sample interactions. In such situations, a force curve resembling that of Figure 2B may be observed.

In the rest of this section, the approach portion (regions 1−3) and the adhesion force portion (region 5) of the force curve are analyzed to obtain chemical information about a variety of different surfaces in a wide range of environments.

1. Approach Curve Analysis

In this subsection we discuss the chemical information that can be obtained in the approach portion of the force curve. Specifically, electrostatic long-range interactions that result from the electrical double layer in aqueous electrolyte and short-range surface-induced solvent ordering that occurs in liquid media are discussed. Both of these interactions are measured in region 2 of the force curve depicted in Figure 2A.

a. Characterization of Double-Layer Forces. An electrical double layer forms at the interface between a charged surface and a solution containing electrolyte. The nature (i.e., composition and structure) of the electrical double layer determines several important properties of a material including its isoelectric point (IEP) and potential of zero charge (pzc). Because so many important chemical and biochemical systems and processes involve a charged surface−solution interface, studies that elucidate the structure of the electrical double layer are both technologically and fundamentally important. Much of the early work in this area relied on indirect macroscopic technologies such as sedimentation and light scattering or on measurements with a surface force apparatus.[198,199] The molecular level spatial and interaction force resolution capabilities of SFM present a means to interrogate such interfaces in a wide range of environments and to test existing theories at a level of detail previously unattainable.

In a significant work, Ducker and co-workers[141,142] were the first to demonstrate that SFM could be used to measure forces between a planar surface and tip-mounted particles. Specifically, the force between a 7.0 μm silica particle and a flat silica surface in aqueous solution was measured as a function of salt concentration and pH. Since these reports, there has been a noted increase of activity in this area. Butt[200] recently reviewed several of the key developments in this area. Therefore, a discussion of this topic is deferred to this review, noting recent studies of the interactions between silica particles and mica,[201] aluminum,[202] and various organic films.[203,204]

Although particle-modified tips are often used to evaluate double-layer interaction forces, unmodified Si_3N_4 tips can also be used. In one of the earliest works in this field, Lin and co-workers[205] measured the force between a Si_3N_4 tip and a silicon oxide surface over a pH range of 3−11. Since the IEP of silicon oxide is very low (pH $\approx$ 2), the surface is negatively charged throughout this pH range. A plot of the pH dependence of force measured at a separation distance of 17 nm showed a gradual transition from an attractive to repulsive manifold as pH increased. At a pH of 6.2, however, the double-layer interaction vanished, indicating that the Si_3N_4 surface was not charged and that the IEP of Si_3N_4 is 6.2. In similar experiments using a Si_3N_4 tip and an alumina surface, Raiteri and co-workers[206] determined the IEP of Si_3N_4 to be at pH 6.5, a finding similar to that of Lin et al. Furthermore, Huttl and co-workers[207] have examined the pH dependence of the forces between a silicon oxide tip and a silicon oxide surface.

In an important extension of the above work, Hillier and co-workers applied SFM to interrogate the electrical double layer at a surface under potential control. Although the architecture of the double layer is reasonably well understood in more macroscopic terms, this work was one of the first to probe the

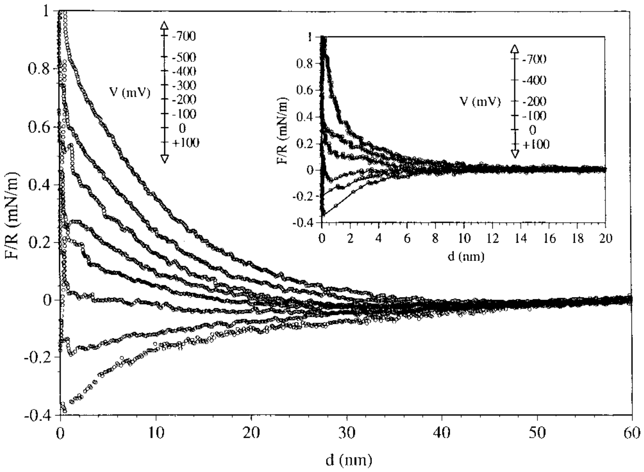

Figure 10. Force between a silica sphere and gold electrode in an aqueous 10^{-3} M solution of KCl at 25 °C and pH ≈5.5 as a function of applied potential. The curves correspond to, from top to bottom, electrode potentials of −700, −500, −400, −300, −200, −100, 0, and 100 mV (vs a saturated calomel electrode, SCE). Inset: Force data for a silica sphere and a gold electrode in 10^{-2} M KCl solution. Reprinted with permission from ref 208. Copyright 1996 American Chemical Society.

double layer around an object under potential control with nanometer resolution. Hillier and co-workers[208] measured the force between a silica sphere affixed to a tip and a gold electrode as a function of the applied potential and the electrolyte composition. At negative applied potentials, the force sensed between the tip and the gold electrode was repulsive, whereas the force was attractive at positive applied potentials. Furthermore, the separation distance at which this force was first detected was dependent strongly on the electrolyte concentration. These findings are summarized in Figure 10. In 10^{-3} M KCl, the interaction between the tip and electrode extended up to a separation distance of 30 nm. However, this interaction was measured at a separation distance no greater than 8 nm in 10^{-2} M KCl. These observations are consistent with the calculated Debye lengths for these solutions.

The dependence of force on the applied potential can be understood from electrical double-layer considerations. At potentials more negative than the pzc of gold, the surface is negatively charged and the double layer of the electrode is dominated by K^+ ions. At these potentials, the force between the gold surface and the negatively charged silica sphere, which also has a double layer comprised largely of K^+ ions, is repulsive. However, at applied potentials positive of the pzc, the electrode is positively charged and its double layer is now comprised largely of Cl^- ions. In this situation, an attractive force is then measured between the electrode and tip. Fits of the experimental and theoretical force (calculated using a nonlinear Poisson−Boltzmann equation) calculated between a silica sphere and gold electrode in 10^{-3} M KCl at pH ≈ 5.5 revealed that a model that assumes a constant surface charge, rather than a model that assumes a constant surface potential, more accurately reflects the data at separation distances greater than 10 nm. At separation distances less than 10 nm, both models fail to predict the experimental results because issues such as surface roughness and the role of other forces, which dominate at short separation distances, come into play. Understanding what factors (i.e., constant surface charge versus constant surface potential) contribute to the forces between charged surfaces in aqueous electrolyte will only add to our understanding of other solid/solution interface systems.

In an extension of the above work, Hu et al.[147] measured the forces between a silica sphere-modified tip and a TiO_2 surface under potential control. These results showed that the potential of zero force (pzf) corresponded well with the flat-band potential (V_{fb}) of TiO_2, an n-type semiconductor, in solutions where the pH was close to the IEP of titania. However, at pH values far from the IEP, the pzf was significantly different from the V_{fb}. Hu et al. theorized that the surface charge induced by the applied potential could not be distinguished from that caused by adsorbates, giving rise to the observed deviation.

Arai and Fujihira[209] added a new element to SFM investigations of the electrical double layer. In their experiments, a Si_3N_4 tip was used to determine the force−distance curve with a gold surface under potential control in aqueous sodium hydroxide (pH 10.9). Below its pzc, gold is negatively charged, and since the uncoated Si_3N_4 tip was negatively charged at pH 10.9, the interaction between the tip and electrode should be repulsive. In contrast, at potentials above the pzc the interaction should be attractive. Somewhat suprisingly, repulsive forces were observed at applied potentials above and below the pzc, that is, from −200 to −140 mV and from −50 to +50 mV (versus NHE, the normal hydrogen electrode). Furthermore, a plot of force versus applied potential at a constant separation distance exhibited a minimum at approximately −100 mV, which corresponds to the pzc of gold under these conditions.

To determine the origin of this unexpected observation, the interactions between a gold-coated tip and a gold electrode were characterized. In this case, both surfaces were held at +20 mV, a potential well positive of the pzc for gold in this electrolyte system. In a finding consistent with the data obtained with an unmodified tip, the observed force was repulsive. Furthermore, a minimum near −140 mV was found in a plot of force versus applied potential. The repulsive nature of all the force curves was therefore ascribed to the specific adsorption of hydroxide ions at gold electrodes, a well-known occurrence. These adsorbates impart a negative charge at the gold−solution boundary, which enriches the surrounding solution layer with cations. This argument also explains the detection of repulsive forces using the unmodified tip. Gewirth has recently reviewed this and related electrochemical aspects of SFM.[210]

In addition to monitoring the electrical double layer formed at unmodified surfaces in solution, the double layer arising from adsorbed films containing ionizable groups can also be interrogated using SFM. The first experiments on such systems were conducted by Ishino and co-workers.[211] As now discussed, several research groups have markedly extended these pioneering studies.

The Lieber laboratory has monitored force as a function of separation distance at various ionic strengths for surfaces modified with alkanethiolate monolayers containing ionizable groups. By varying the ion concentration, the thickness of the charged layer surrounding the ionized groups can be manipulated to enhance or suppress the extent of the electrostatic interactions between an ionizable surface and a tip. Vezenov and co-workers[212] reported that, at a constant pH, the repulsive force measured between a tip and sample surface which were both modified with COOH functionalities extended further into solution as the ionic concentration decreased and became more short ranged as the ionic concentration increased. We note that estimations by Vezenov et al. of the surface potential from their force−distance plots agree well with the surface potential model of Reiner and Radke.[213]

In similar work, van der Vegte and Hadziioannou[214] examined force−distance curves to ascertain the effect of electrolyte concentration on the electrical double layer formed between a tip and surface, both of which were modified with COOH functionalities. The experiments were conducted at pH 6.4 to ensure that the terminal groups on both the tip and surface were partially ionized. The manifestation of the electrical double layers formed at these two surfaces was therefore detected as a repulsive force. The repulsive force, as measured over a wide range of electrolyte concentrations, followed the theoretical Debye length calculated for this system, a further confirmation of the reliability of this important theoretical description of ionic solutions.

The Bard laboratory has used SFM to gain chemical insight into the nature of the electrical double layer. Hu and Bard[215] used a Si_3N_4 tip modified with a silica sphere to probe the electrical double layer formed with the contacting solution confined between both COOH-modified and unmodified gold surfaces. This investigation was motivated, in part, by observations that the pK_a of surface-immobilized acids and bases often vary widely from their solution counterparts. At an unmodified bare gold surface (pH 6), an attractive force was measured between the silica sphere, which was negatively charged at pH 6 and surrounded by a cation-rich electrical double layer, and the gold surface. This finding was ascribed to the formation of a positive image charge in the gold, which was subsequently surrounded by an anion-rich electrical double layer. However, the force curve for the same tip and a gold surface that was modified with a COOH-terminated alkanethiolate monolayer revealed the presence of an electrostatic repulsion.

To convert these results into a framework that could be interpreted in a fashion similar to a titration curve, Hu and Bard compared their experimental data to theoretical predictions of the forces between two dissimilarly charged surfaces obtained by using a nonlinear Poisson−Boltzmann equation.[208] On the basis of the known potential for silica, the surface electrostatic potentials of the monolayer-modified surfaces were calculated as a function of pH. The resulting plot, which was sigmoidal in shape, is directly analogous to a surface titration curve. The plot revealed a p$K_{1/2}$ (the solution pH at which the surface potential is midway between its plateau at high and low pH) near 8.0, a value that is ~3.5 pK units higher than that reported for carboxylic acids in bulk solution.[216] They proposed that this deviation was the result of strong lateral intermolecular hydrogen bonds formed between neighboring molecules on the surface. Such bonding had been shown by infrared spectroscopy to result in a significant shift in the carbonyl stretching mode to lower energy, an indication that hydrogen bonding causes protons to be held more tightly to the monolayer surface.[217] Furthermore, Hu and Bard theorized that ionization of these protons would be energetically unfavorable because it would lead to electrostatic repulsion between neighboring groups.

Force−distance curves were also examined by Hu and co-workers[218] in an attempt to unravel the evolution of the electrical double layer during mono- and multilayer film growth. Using a similar experimental setup, a tip modified with a silica sphere was used to monitor the growth of aluminum(III) alkanebisphosphonate layers on gold. The probe tip carried a negative charge, resulting in a surrounding cation-rich electrical double layer. Before exposure to Al^{3+} ions, the force between the tip and sample was repulsive, indicating that both the tip and monolayer surface were negatively charged at the experimental pH and surrounded by cation-rich electrical double layers. After exposure to Al^{3+} ions, force measurements indicated an attractive interaction between the two surfaces, as Al^{3+} ions electrostatically bound to the negatively charged oxygen−phosphorus network. The layer-by-layer growth was monitored from the reversal of the interaction force for up to 10 layers. The observed force dependence was attributed to the nature of the electrical double layer of each of the two surfaces. Similar experiments were obtained after both single- and double-stranded DNA was adsorbed to aluminum-exposed phosphonate monolayers.

In a particularly interesting work, Larson and co-workers[219] used SFM to monitor the real-time evolution of the electrical double layer in the presence of an aggressive adsorbate. Using a tip modified with a gold-coated tungsten sphere and a gold substrate, the electrical double layer was examined in a sodium citrate solution (pH $\approx$ 7.8). Initially, both surfaces were coated with a layer of adsorbed citrate ions and the force between the two surfaces was repulsive, a finding consistent with the presence of cation-rich electrical double layers near both the tip and surface. When the contacting solution was changed to 4-(dimethylamino)pyridine (DMAP), the repulsive force decreased for ~15 min, after which a slightly attractive double layer was observed. These findings are illustrated in Figure 11. The evolution of the observed force reflected the gradual displacement of adsorbed citrate ion by DMAP, which changed the net charge within the double layer. Assuming a first-order rate law, Larson and co-workers determined the change in the electrical double-layer charge to be -1.32×10^{-4}, -9.15×10^{-4}, and -6.06×10^{-3} s^{-1} for DMAP concentrations of 10^{-4}, 10^{-3}, and 10^{-2} M, respectively.

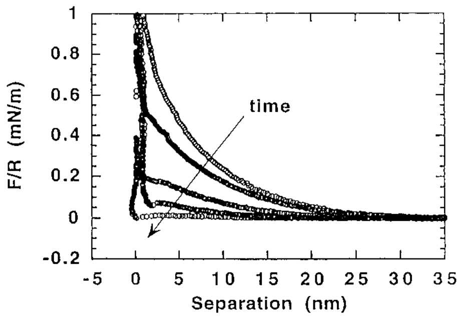

Figure 11. Normalized force–separation curves for the interaction between a gold-coated tungsten sphere and a gold surface in the presence of trisodium citrate (10^{-4} M) and DMAP (10^{-3} M) at pH 10.5. Times after injection of DMAP for the curves are 0, 2, 5, 9, and 14 min. After ~15 min, the initial repulsive force has decayed to near zero, and the interaction then becomes attractive. Reprinted with permission from ref 219. Copyright 1997 American Chemical Society.

b. Measurements in the Discrete Region. In addition to measurement of the electrical double layer, the noncontact region of a force curve can also be used to access issues about surface-induced solvent ordering. Solvent ordering causes a change in the short-range solvation forces acting between two surfaces. Therefore, when placed in close proximity to a surface in solution, a tip can be employed to measure forces arising from solvent ordering. Using the surface force apparatus, Israelachvili and co-workers evaluated the mechanical consequences of these forces.[220,221] However, SFM provides superior spatial resolution, allowing a more exacting measurement of discrete ordering events. We note that the portion of the force curve that contains information about solvent ordering is sometimes referred to as the discrete region.

In an early work by O'Shea et al.,[222] a Si_3N_4 tip was employed to monitor solvation forces near a graphite surface. When octamethylcyclotetrasiloxane (OMCTS) or 1-dodecanol was used as a solvent, a periodic oscillation in the force curve was observed as the tip approached the surface at a constant velocity. This periodicity, detailed in Figure 12A,B results from the tip encountering layers of ordered solvent, pushing through the layer via an increase in the applied force, and then moving toward the surface unimpeded, resulting in a decrease in applied force until the next molecular layer of ordered solvent is encountered. The periodicity of the oscillation is diagnostic of the size of the ordered solvent molecules. The magnitude of the oscillation, which increases as the tip approaches the surface, is indicative of an increase in solvent ordering as the tip approaches the surface. Since the oscillations were heavily dependent on the size and shape of the tip, as well as the approach velocity, this type of experiment may be adaptable to probe details about the fluid dynamics at the wall–fluid boundary of flowing streams or the lubricant order at the moving read head–disk interface.

With OMCTS (Figure 12A), the periodic oscillations were superimposed upon an attractive force profile, whereas those with 1-dodecanol (Figure 12B) were superimposed upon a repulsive profile. It was speculated that the different force curves may be due, in part, to the surfactant nature of 1-dodecanol. Previous STM studies of 1-dodecanol on graphite revealed that the solvent molecules pair with one another by hydrogen bonding to create highly ordered, two-dimensional films.[223] This increased ordering may result in a more densely packed solvent layer near the surface that may explain the repulsive nature of the force curve.

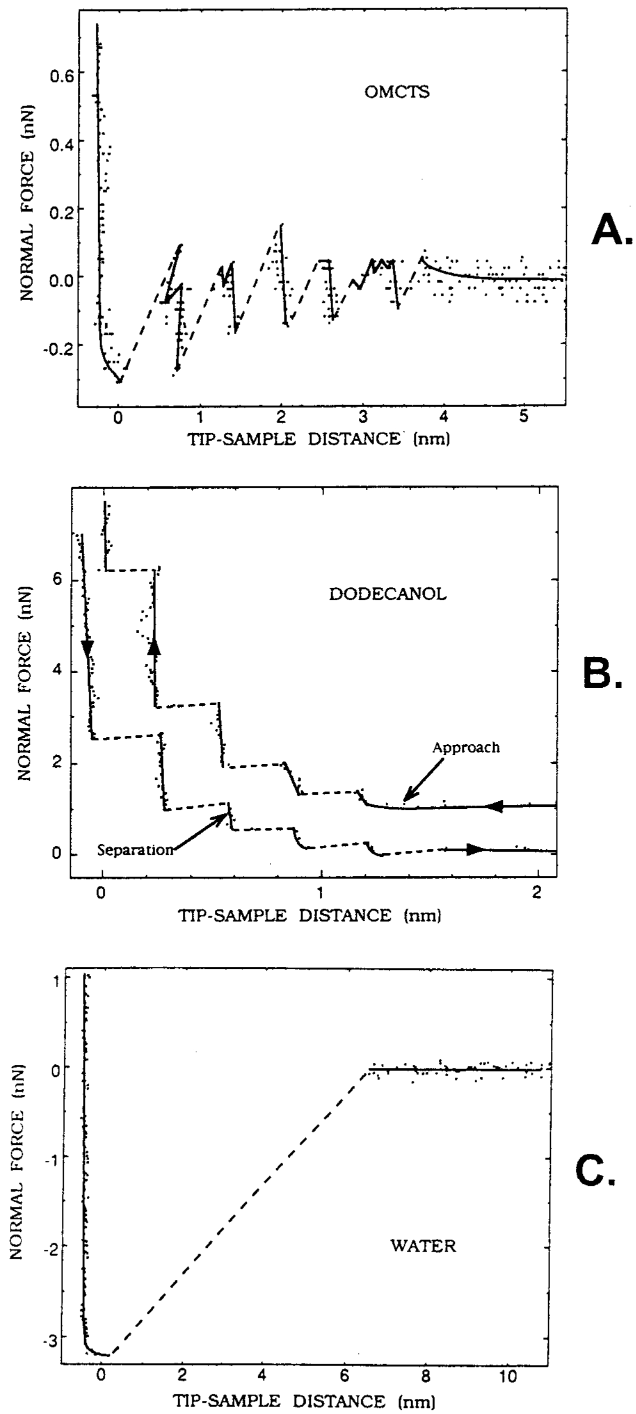

Figure 12. Variation of the normal force acting on a Si_3N_4 tip as a function of tip–sample separation for HOPG immersed in (A) OMCTS, (B) dodecanol, and (C) water. Reprinted with permission from ref 222. Copyright 1992 American Institute of Physics.

In contrast to OMCTS and 1-dodecanol, the normal force did not vary as the tip approached a graphite surface in water, as shown in Figure 12C. In fact, the tip jumps to contact with a large attractive force. Though speculative, this observation may arise from the hydrophobic, nonwettable nature of graphite. Since a Si_3N_4 tip is often hydrophobic because of adsorbed contaminants, its approach to the surface may actually repel the water from the space between the tip and surface, making an observation of discrete solvent molecular ordering intractable.

In an extension of this work, O'Shea et al. used a modified scanning force microscope to measure solvation forces with a much higher sensitivity.[224] To realize this improvement, an external magnetic field was used to oscillate a magnetically coated tip, driving the tip at much smaller amplitudes than accessible when excited acoustically. These smaller amplitudes yielded higher resolution images because of the smaller asperities on the tip. With 1-dodecanol as a solvent and a mica surface, an oscillation period of 0.37 ± 0.7 nm was observed, which is consistent with the alkyl chains of the solvent molecules lying parallel to the substrate. This important improvement opens the door to obtain information about the orientation of solvent molecules at an interface. Indeed, Han and Lindsay have recently exploited this concept in an investigation of solvent and adsorbate ordering that detailed the mechanical properties of the interface in terms of the decay length of the Young's modulus.[225]

To summarize briefly, the noncontact portion of the approach curve contains valuable chemical information that can be used to advance our understanding of a wide variety of systems. Insights into the nature of the electrical double layer as well as the degree of solvent ordering induced at the sample–solution interface, including the orientation of solvent molecules, can be gained, all of which will have important implications in areas such as lubrication and wear, electrochemistry, and fluid mechanics.

2. Adhesion Force Measurements

In this section we discuss the chemical information that can be obtained by measuring the adhesion force, F_{ad}, as the tip and sample break contact. This process is illustrated in region 5 of Figure 2A and can be used to probe the interactions that act at the microcontact in a variety of environments. We begin by describing the formulizations that relate adhesion force to interfacial properties, such as surface free energy.[94] We then develop the experimental correlation between these aspects and specific chemical interactions.

a. Theoretical Considerations. The work of adhesion, W_{132} (i.e., the work required to separate surface 1 and surface 2 in medium 3 per unit area), is related to interfacial energies by

$$W_{132} = \gamma_{13} + \gamma_{23} - \gamma_{12} \tag{2}$$

where γ represents interfacial energy, 1 and 2 refer to the two surfaces, and 3 refers to the contacting medium. When measurements are performed between symmetric contacts (i.e., $\gamma_1 = \gamma_2$) in medium 3, eq 2 becomes

$$W_{131} = 2\gamma_{13} \tag{3}$$

If measurements are performed in a vacuum or in inert gas, the interfacial energy γ_{13} is simply the surface free energy, γ_1. In this case, W_{132} reduces to W_{12}, which represents the work of adhesion for an asymmetric contact and equals $\gamma_1 + \gamma_2 - \gamma_{12}$. Similarly, W_{12} is the work of cohesion for a symmetric contact and is given as $2\gamma_1$.

By applying continuum mechanics to the interactions at the SFM microcontact (i.e., a sphere in contact with a flat surface), the experimentally determined adhesion force can be related to the work of adhesion.[66] There are two readily tractable approaches: DMT (Derjaguin, Muller, and Toporov) theory[226] and JKR (Johnson, Kendall, and Roberts) theory.[227] The former assumes that the interfacial forces act only over a finite range and that there is no contact between the tip and sample upon rupture. The latter considers that only short-range interfacial forces are operative and that a finite contact area exists upon rupture. Both are based on instances where the contact load is small, a situation where interfacial forces are important. As such, the adhesion force from DMT theory is given as

$$F_{ad} = 2\pi R W_{132} \tag{4}$$

where R is the radius of the tip. The expression developed by JKR theory is

$$F_{ad} = 1.5\pi R W_{132} \tag{5}$$

These formulations provide a basis for relating the work of adhesion and the interfacial energies to the adhesion forces obtained by microcontact rupture experiments, i.e., the pull-off portion of the force curve. However, as recently discussed, the experimental variability in the adhesion data precludes a clear diagnosis of the relative merits of the two formulations.[228] We note that JKR theory more realistically depicts the flow of the contact material via a necked region at the instant of contact rupture.[229]

Since JKR theory considers the existence of a finite contact area when the microcontact ruptures, SFM-measured adhesion forces can be used to estimate the number of molecular contacts at the instant of rupture. The contact radius, a, is defined in JKR theory by

$$a = (1.5\pi R^2 W_{132}/K)^{1/3} \tag{6}$$

where K is the effective elastic modulus of the microcontact and is given as

$$1/K = 3/4\,[((1 - \nu^2_{tip})/E_{tip}) + ((1 - \nu^2_{sample})/E_{sample})] \tag{7}$$

In this equation, E is the Young's modulus and ν is the Poisson ratio of the tip and sample materials.

b. Measurements in Dry Environments. In experiments that laid the foundation for this type of characterization, adhesion forces between alkanethiolate-modified probe tips and similarly modified gold

Table 2. Surface and Interfacial Free Energies Estimated from SFM-Based Adhesion Data

microcontact	monolayer	γ (mJ/m^2)	environment	ref
CH_3/CH_3	thiol, C_9-C_{11}	30	dry air	230
NH_2/NH_2	thiol, C_9-C_{11}	50		
COOH/COOH	thiol, C_9-C_{11}	114		
NH_2/COOH	thiol, C_9-C_{11}	−516		
CH_3/ethanol	thiol, C_{18}	2.5	ethanol	237
COOH/ethanol	thiol, C_{11}	4.5		
CH_3/COOH	thiol, C_{18}, C_{11}	5.8		
CH_3/CH_3	thiol, C_{11}	22	various solvents	228
COOH/COOH	thiol, C_{10}	≥55	various solvents	238
$CONH_2/CONH_2$	thiol, C_{10}	≥55		
OH/OH	thiol, C_{11}	≥40		
CH_3/ethanol	thiol, C_{12}	2.5	ethanol	128
OH/ethanol	thiol, C_{12}	3.0		
NH_2/ethanol	thiol, C_2	2.8		
COOH/ethanol	thiol, C_{11}	4.5		
$CONH_2$/ethanol	thiol, C_{11}	5.3		
CH_3/OH	thiol, C_{12}	4.4		
CH_3/NH_2	thiol, C_{12}, C_2	3.8		
CH_3/COOH	thiol, C_{12}, C_{11}	4.8		
$CH_3/CONH_2$	thiol, C_{12}, C_{11}	6.1		
OH/NH_2	thiol, C_{11}, C_2	−1.9		
OH/COOH	thiol, C_{11}, C_{11}	−1.7		
OH/$CONH_2$	thiol, C_{11}, C_{11}	−2		
NH_2/COOH	thiol, C_2, C_{11}	−2.4		
$NH_2/CONH_2$	thiol, C_2, C_{11}	0.6		
COOH/$CONH_2$	thiol, C_{11}, C_{11}	−6		

substrates were determined in dry air by Thomas and co-workers.[230] For systems modified with the same terminal group on both the tip and sample, the normalized adhesion force (reported as F_{ad}/R, where R is the radius of the tip) for a CH_3-terminated contact (0.4 ± 0.2 N/m) was less than that for a NH_2-terminated contact (0.7 ± 0.2 N/m); both were less than the adhesion force measured for a COOH-terminated contact (1.4 ± 0.3 N/m). This trend is consistent with the relative weakness of the van der Waals interaction present between CH_3-terminated surfaces in comparison to the hydrogen-bonding interactions for NH_2- and COOH-terminated contacts. This investigation also reported an adhesion force of 4.3 ± 0.4 N/m for the contact formed between tip−sample combinations having a COOH terminal group and a NH_2 terminal group.

Equation 4 can be used to calculate the surface free energies from these data. Importantly, the resulting surface free energy for a CH_3-terminated contact (30 mJ/m^2) is consistent with that obtained using a surface force apparatus[231] and by contact angle measurements.[232] The result from the SFM rupture experiment was also consistent with the value predicted from Lifshitz's theory,[94] arguing that the adhesive force of CH_3-terminated surfaces can be attributed solely to van der Waals interactions.

Surface free energies of 50 and 114 mJ/m^2 were obtained for the NH_2-terminated contacts and COOH-terminated contacts, respectively; Table 2 summarizes these data along with those from pull-off experiments discussed in the next subsection. Assuming that the surface free energy at these contacts consists only of van der Waals and hydrogen-bonding terms and that the van der Waals term equals that found for the CH_3-terminated surface, hydrogen-bonding energies for the NH_2 and COOH groups can be estimated. On the basis of the molecular packing density of this type of thiolate monolayer (0.2 nm^2 per molecule), hydrogen-bonding energies of 5.4 and 21 kJ/mol were obtained for the NH_2 group and the COOH group, respectively. These results were smaller than the expected values of 14 and 58 kJ/mol[233] and may reflect the presence of intramonolayer (e.g., side-to-side) hydrogen bonds or steric restrictions associated with the close-packed film structure.

In addition to hydrogen-bonding interactions, pull-off experiments were conducted to characterize the acid−base interactions at a NH_2/COOH contact. From these data (F_{ad}/R = 4.3 ± 0.4 N/m) and the surface free energies of the NH_2 group and the COOH group, the interfacial free energy at the contact between the NH_2 group and the COOH group was estimated to be −516 mJ/m^2. The negative sign for interfacial free energy indicates the presence of a comparatively strong bond between the NH_2 and COOH groups.

c. Measurements in Organic Solvent. Force measurements carried out in the ambient can be difficult to interpret because capillary forces resulting from adsorbed water molecules on the tip and sample are often an order of magnitude higher than forces resulting from specific chemical interactions.[139,234−236] Because of the challenges faced in excluding the presence of adsorbed water or other contaminants in experiments conducted in dried gas environments, most investigations of interaction forces are performed under liquids. Adhesion forces in water, especially between ionizable terminal groups, are affected by the pH and ionic strength of the solution. Furthermore, the interactions at the contact are a complex combination of double-layer as well as van der Waals interactions, and the results of such experiments will be discussed in a later section. Experiments, however, can be designed that simplify interpretations of the results by using organic solvents (e.g., ethanol), thereby greatly minimizing contributions from ionization effects. Experiments can therefore be carried out that can begin to more clearly relate the adhesion detected at the microcontact in terms of surface free energies and specific chemical interactions.[126,134,135,237−239] We note that using a contacting medium may obscure the detection of intermolecular forces between some types of terminal groups.[238]

In the first exploration in this area, silane chemistry was used to create surfaces terminated in various chemical functionalities.[135] In ethanol, an adhesion force of ~4 nN was detected between a CH_3-terminated Si_3N_4 tip and a CH_3-modified silicon substrate, whereas the adhesion force for the same tip and an uncoated surface of silicon oxide was effectively zero. This difference is consistent with the expected immiscibility of a CH_3-terminated tip and uncoated silicon oxide.

In an important followup investigation,[134] tips and substrates were modified with adlayers terminated with either CH_3 or CF_3 groups, and the adhesion forces in three different contacting liquids (i.e., ethanol, octane, and perfluorooctane) were determined to investigate the role of the solvent in adhesion measurements. The average adhesion forces at a CH_3-modified substrate for a CH_3-terminated tip and for a CF_3-terminated tip in ethanol were 3.5 and 0 nN, respectively. At a CF_3-terminated substrate in ethanol, the adhesion forces measured were 0 nN for a CH_3-terminated tip and 15.4 nN for a CF_3-terminated tip. These differences substantiate the above immiscibility arguments in that adhesion between immiscible groups is small or may even be repulsive. However, the nature of the solvent can significantly affect the adhesion between the tip and surface. Indeed, when the measurements were performed in octane and perfluorooctane, the adhesion forces between a CH_3-terminated tip and a CH_3-terminated substrate were found to be 0 and 52 nN, respectively. In contrast, the respective adhesion forces between a CF_3-terminated tip and a CF_3-terminated substrate were 21 and 0 nN in octane and perfluoroctane, respectively.

These data can be summarized as follows. In general, interactions between immiscible materials are either very small or repulsive. Furthermore, when the contacting medium is miscible with the terminal groups at the microcontact, the force required to separate the tip and substrate is small. On the other hand, the force necessary to separate the tip and sample is large when the contacting liquid is immiscible with the terminal groups at the microcontact.

Sinniah and co-workers[238] emphasized how understanding the influence of the solvent in regulating adhesive interactions is critical to the interpretation of measurements performed in liquid media. Using a wide range of terminal groups (i.e., CH_3, CH_2OCH_3, CO_2CH_3, $CONH_2$, COOH, and CH_2OH) on both the tip and sample, adhesion forces between like chemical functional groups were measured in water, ethanol, and *n*-hexadecane. Water had the most pronounced effect, with adhesion forces scaling directly with solvent exclusion and the greatest adhesion found between hydrophobic surfaces. In ethanol, the adhesive forces were substantially smaller, but still sufficient to distinguish a CH_3-terminated surface from the more hydrophilic surfaces. In hexadecane, the adhesive forces were negligible for all tip–sample combinations.

Frisbie et al.[126,237] extended these results by conducting a similar set of experiments. Figure 13 shows force–distance curves obtained in ethanol between a COOH-terminated tip and a COOH-terminated sample, a COOH-terminated tip and a CH_3-terminated sample, and a CH_3-terminated tip and a CH_3-terminated sample.[237] The trend in terms of an increase in adhesive interactions at the tip–sample microcontact was COOH/COOH > CH_3/CH_3 > COOH/CH_3. Interactions between hydrogen-bonding partners, i.e., the COOH/COOH combination, were greater than those for the non-hydrogen-bonding CH_3 groups. The smaller adhesion force on the COOH/CH_3 system was due to the immiscibility of the CH_3- and COOH-terminated surfaces. These experiments also confirmed the value of performing a high number of repetitive measurements and statistically analyzing the results to quantify the differences and uncertainties in these types of studies.

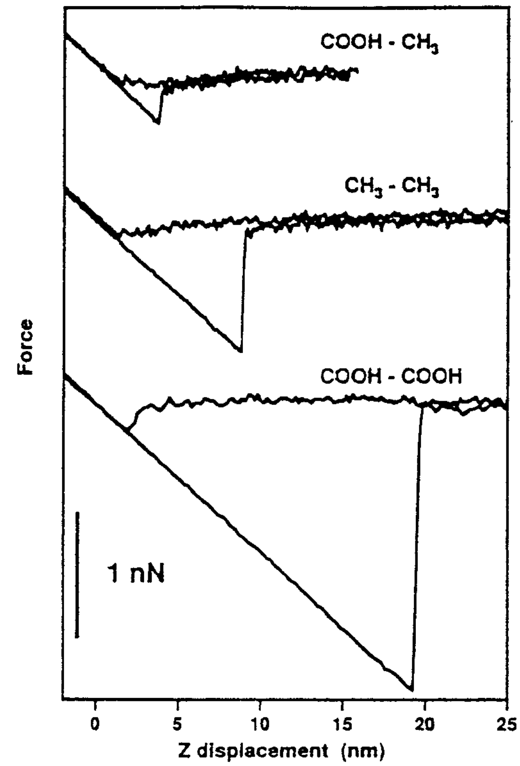

Figure 13. Representative force–distance curves recorded for COOH/CH_3, CH_3/CH_3, and COOH/COOH tip–sample functionalizations (~60 nm tip radius). All data were obtained in neat ethanol. Reprinted with permission from ref 237. Copyright 1995 American Chemical Society.

Noy and co-workers[237] evaluated the applicability of JKR theory to SFM-based adhesion measurements. On the basis of an estimated tip radius of 60 nm and the reported interfacial free energy between a CH_3-terminated monolayer and ethanol (2.5 mJ/m^2), the adhesion force between CH_3-terminated groups in ethanol was calculated to be 1.2 nN. This value agreed reasonably well with the experimental value of 1.0 ± 0.4 nN. Thus, JKR theory provides a very effective means for the interpretation of the nanometer-scale adhesion measurements tractable with SFM. Table 2 summarizes the findings of many of the above experiments.

d. Single Molecular Interaction Forces. The first work to report the observation of discrete quantized adhesive interactions between a SFM tip and a surface was that of Hoh and co-workers.[240] They observed adhesive forces in multiples of ~0.01 nN, and proposed such interactions were due to either the rupture of hydrogen bonds between the silicon nitride tip and a glass surface, or the presence of ordered water layers near the surface. Since then, other methods have been employed to study single molecular interaction forces, including JKR theory and Poisson statistics.

As noted, JKR theory via eq 6 provides a basis to determine a contact radius at the instant of rupture, and therefore a means to estimate the number of molecular contacts. At issue then is how to determine the value of the effective elastic modulus (K in eq 7) for systems composed of organic coatings that are

Table 3. Single Molecular Interaction Forces Estimated from SFM-Based Adhesion Measurements

microcontact	medium	adhesion forces (nN)	contact area[a] (nm^2)	number of molecules[b]	single molecular interaction force (pN)	data analysis method	ref
CH_3/CH_3	ethanol	1.0	3.1	15	66[c]	JKR model	228, 237
COOH/COOH	ethanol	2.3	5[c]	25	92[c]		
CH_3/CH_3	water	12.5	10	50	250[c]	JKR model	238
CH_3/CH_3	ethanol	2.3	10	50	46[c]		
CH_3/CH_3	n-$C_{16}H_{34}$	0.07	10	50	1[c]		
OH/OH	water	5.38	3.1	7	768[c]	JKR model	138
CH_3/CH_3	ethanol	0.9	2.2[c]	11[c]	81	JKR model	128
OH/OH	ethanol	0.9	1.8[c]	9[c]	101		
COOH/COOH	ethanol	1.3	2.2[c]	11[c]	114		
COOH/COOH	water				16.6	statistical analysis	242
COOH/COOH	1-propanol				57.1		
CH_3/CH_3	water				658	statistical analysis	245
CH_3/CH_3	1-propanol				281		
OH/OH	water				119	statistical analysis	244
OH/OH	1-propanol				302		

[a] Calculated using eq 6. [b] Calculated using 0.2 nm^2 for the area per adsorbed thiolate on gold[128,228,237,238] and 0.43 nm^2 per adsorbate for the silane monolayer.[138] [c] Estimated from the reported data.

supported on materials with markedly different mechanical properties. Investigations using monolayer films simplify this issue since the thickness of the organic adlayer is much less than that of the supporting material. Thus, K is dominated by the properties of bulk gold (i.e., 64 GPa[241]) for microcontacts formed by the assembly of thiolate monolayers on gold-coated tips and substrates.

Using these considerations, Lieber's laboratory reported a contact area at rupture of 3.1 nm^2 for a CH_3/CH_3 contact.[126,237] Assuming that a thiolate monolayer on gold is closely packed (i.e., 0.2 nm^2 per adsorbate), 15 molecular pairs were in contact at rupture. From the adhesion force of 1.0 nN, a single molecular interaction force of 66 pN can be estimated. Table 3 summarizes a collection of such data for several types of contacts and surrounding environments from several research laboratories.

There is another intriguing approach to extracting information about the interactions between single molecules from SFM-measured adhesion.[242−245] This approach uses Poisson statistics to obtain single molecular interaction forces from a large ensemble of repeated determinations. It assumes that (1) the detected adhesion force is the sum of a finite number of discrete chemical interactions, (2) these interactions form randomly and are all similar in magnitude, and (3) there is no upper limit of possible interactions at the contact. As a consequence, the mean of the distribution (μ) equals the product of the number of interactions (m) and the adhesive force of the individual interaction (F), where the variance (σ^2) is mF^2. Thus, σ^2/μ gives the value of the adhesive force between a single pair of molecules (F(pr)), and a plot of σ^2 vs μ should be linear with a slope of F(pr) and a zero intercept.

Adhesion forces between thiolate-modified gold-coated tips and samples were measured in water, 1-propanol, and hexane.[242] The magnitude of single hydrogen bonds between COOH groups on the tip and surface was determined to be 16.6 ± 1.8 pN in water, 57.1 ± 10.3 pN in 1-propanol, and 70.6 ± 2.4 pN in hexane. Extrapolation of the plot of interaction forces per molecular pair as a function of the dielectric constant of the medium, ϵ, to $\epsilon = 1$ yields the hydrogen-bonding strength in a vacuum. Thus, the hydrogen bond strength for COOH groups is 144 ± 7 pN, which translates to a bond energy of 7.6 ± 0.4 kJ/mol. This value is slightly smaller than a typical hydrogen bond energy, which is 10−40 kJ/mol.[94] Similarly, single molecular interaction forces between OH-terminated silane molecules in a vacuum were estimated to be 362 ± 10 pN, with a bond energy of 19.5 ± 2.1 kJ/mol.[244] The results obtained by this statistical analysis are also listed in Table 3. Importantly, the magnitude of single molecular interaction forces obtained from the JKR model and the results obtained by the statistical analysis of the experimental data are in fairly good agreement, lending strong support for the use of SFM to detect the interactions between single molecular pairs.

e. Force Titrations. When measured in liquid, adhesion is a function of a large number of parameters in addition to surface composition. These parameters include the pH,[212,214,246] ionic strength,[214,246−248] and dielectric constant at an interface. Issues related to solvation and reactions at interfaces can also be important. In addition to providing insights into surface tension and compositional issues, adhesion forces can also be used to evaluate other surface parameters. In this section we discuss how these measurements can be used to monitor interfacial reactions.

One way in which adhesion measurements conducted in aqueous electrolytes can provide insights into chemical transformations at interfaces is by monitoring the extent of ionization at a surface comprised of ionizable groups. To determine the extent of ionization, a force titration curve may be constructed.[212,249,250] As implied, a force titration curve is a plot of the adhesion determined in a series of force curves as a function of solution pH, where the change in the force required to separate the tip and sample reflects a change in the ionization at the microcontact. More traditional methods for determin-

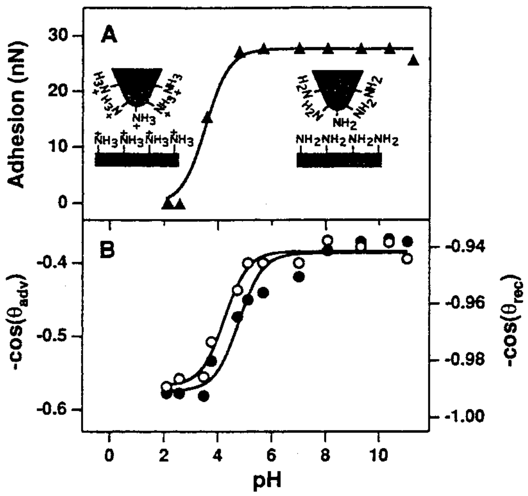

Figure 14. (A) Adhesion force between a sample and tip both functionalized with amino groups versus pH. The value of the adhesion force is the mean obtained from more than 200 single measurements. (B) Negative cosines of the advancing (open circles) and receding (filled circles) contact angles of phosphate buffer drops on a sample modified with APTES as a function of pH. Reprinted with permission from ref 212. Copyright 1997 American Chemical Society.

ing surface ionization (e.g., contact angle measurements) are macroscopic in content. In contrast, SFM is sensitive on a nanometer length scale, thereby allowing characterizations of surfaces that are chemically heterogeneous. We note that the ionization state of surface ionizable groups can also be determined by monitoring the approach portion of the force curve, as discussed earlier.

Several laboratories have conducted force titration curve measurements;[212,214,251,252] two of the most active are those of Lieber and Hadziioannou. Vezenov and researchers in the Lieber laboratory investigated the adhesion between tips and samples modified with monolayers terminated with a variety of functionalities as a function of several parameters such as pH and ionic strength.[212] Figure 14A reports the sigmoidal-shaped force titration curve obtained between a Si_3N_4 tip and a silicon surface, both modified with the amine-terminated polymer (3-aminopropyl)triethoxysilane (APTES), as a function of pH. Low adhesion forces were observed near pH $\approx$ 2; between pH 2 and pH 4, the measured adhesion increased sharply and then leveled off at pH $\approx$ 5. The curve obtained by SFM analysis was in reasonable agreement with that obtained from traditional contact angle measurements on the same amine-terminated surface (Figure 14B). A similarly shaped force titration curve was found by van der Vegte and Hadziioannou for a gold-coated tip and surface both modified with 2-aminoethanethiol.[128]

However, a force titration curve displaying the opposite trend, i.e., high adhesion at low values of pH and low adhesion at high values of pH, was reported by Zhang and co-workers for a gold-coated SFM tip and surface both modified with 4-aminothiophenol (4-ATP).[251] Zhang et al. speculated that the trend in the 4-ATP force titration curve may have arisen from the delocalization of the positive charge on the amine groups at low pH via the phenyl ring.

When Vezenov and co-workers calculated surface pK_a values from their force titration curve and contact angle measurements (3.9 and 4.3, respectively), the values were 6−7 pK units lower than the solution values for such systems.[216] Two possible explanations for this discrepancy were put forth: (1) poor solvation of the positively charged surface amine functionalities at low pH or (2) relatively high adhesion forces at higher values of pH. Such high adhesion forces at high values of pH could indicate disorder within the silane monolayer that exposes methylene groups to the surface. This disorder could, in part, shift the measured surface pK_a to lower values.

Furthermore, when examining the effect of pH on the adhesion force measured between a tip and surface both modified with 11-mercaptoundecanoic acid, Vezenov and co-workers also measured a sigmoidal-shaped force titration curve.[212] As expected, the curve shows a trend opposite to that observed in the amine-terminated system; that is, the acid-terminated system revealed high adhesion forces at low values of pH and low adhesion forces at high values of pH. This result was also in agreement with that obtained by van der Vegte and Hadziioannou for the same acid-terminated thiol.[128] In contrast, He and co-workers obtained a peak-shaped curve for the same acid-terminated thiol at gold.[249] The reason for this discrepancy is presently unclear. In contrast to the amine system, the pK_a of 5.5 $\pm$ 0.5 extracted by Vezenov from the force titration curve obtained from the acid-terminated monolayer system is within 0.75 pK unit of that reported for carboxylic acids in water.[253] van der Vegte and Hadziioannou estimated a pK_a of ~4.8 for their system, which is in good agreement with that of Vezenov.

In addition to reporting force titration data for carboxylic acid- and amine-terminated tips and surfaces, van der Vegte and Hadziioannou reported a force titration curve for a gold tip and gold surface both modified with a PO_3H_2-terminated alkanethiolate monolayer.[214] To our knowledge, this is the only report of a force titration curve involving a diprotic acid. This curve is presented in Figure 15. The curve clearly detects two well-separated ionization events, i.e., $PO_3H_2 \rightarrow PO_3H^-$ and $PO_3H^- \rightarrow PO_3^{2-}$. The calculated surface pK_a values for these events (4.6 and 11.6) are shifted 2−3 pK units higher than those reported for free organic phosphonic acids in solution (~3 and ~8).[253,254] Following earlier speculation, the discrepancy was ascribed to unfavorable ionic solvation effects, or the buildup of excess surface charge, or a combination of both.

f. Monitoring Other Types of Chemical Reactions. Hadziioannou and co-workers recently demonstrated another way to apply SFM-based adhesion to monitor chemical transformations at surfaces.[189] This investigation used amide-modified tips to monitor in real-time the conversion of OH- and COOH-functionalized surfaces into butyl-terminated surfaces upon exposure to butyl isocyanate. A set of data is presented in Figure 16. We note that the terminal groups on the tip hydrogen bond to OH- or COOH-functionalized surfaces, but only weakly interact with the much

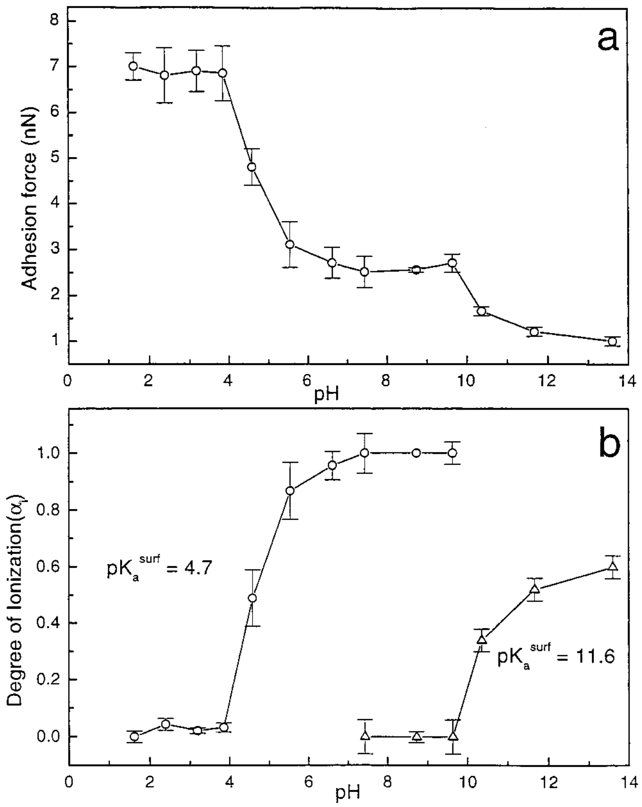

Figure 15. Force titration curve for a PO_3H_2-functionalized tip and a PO_3H_2-functionalized surface. (a) Adhesion force titration curve at constant ionic strength. (b) Degree of ionization, α_i, as a function of pH calculated from the adhesion forces. Reprinted with permission from ref 214. Copyright 1997 American Chemical Society.

lower surface free energy butyl-terminated surfaces. Initially, a large adhesion force was observed between the tip and sample. After the addition of butyl isocyanate, the gradual conversion of the terminal OH or COOH groups to butyl groups occurred and the subsequent adhesion between the tip and sample diminished, reflecting a decrease in the extent of hydrogen bonding between the two surfaces. Differences in the rates and extents of conversion, both of which traced mechanistic considerations, between the OH- and COOH-terminated surfaces could also be detected. The difference in reaction times most likely stems from the different chemical mechanisms taking place at each surface. The OH functionalities are converted into urethane moieties whereas the acid functionalities are converted to amides with the loss of carbon dioxide. The progress of these reactions was monitored by friction force microscopy and is illustrated in a later section. This work demonstrated that SFM can be used to perform real-time chemical analysis.

Several laboratories have explored the use of adhesion to monitor electrochemical processes. Green et al. demonstrated the ability to monitor in real-time the electrochemical transformations of a redox active surface species.[160] More specifically, a gold-coated probe tip modified with an octadecanethiolate monolayer was used to probe the change in the adhesion of a surface modified with a ferrocene-terminated alkanethiolate monolayer on gold as the applied potential was cycled over a range that oxidized and

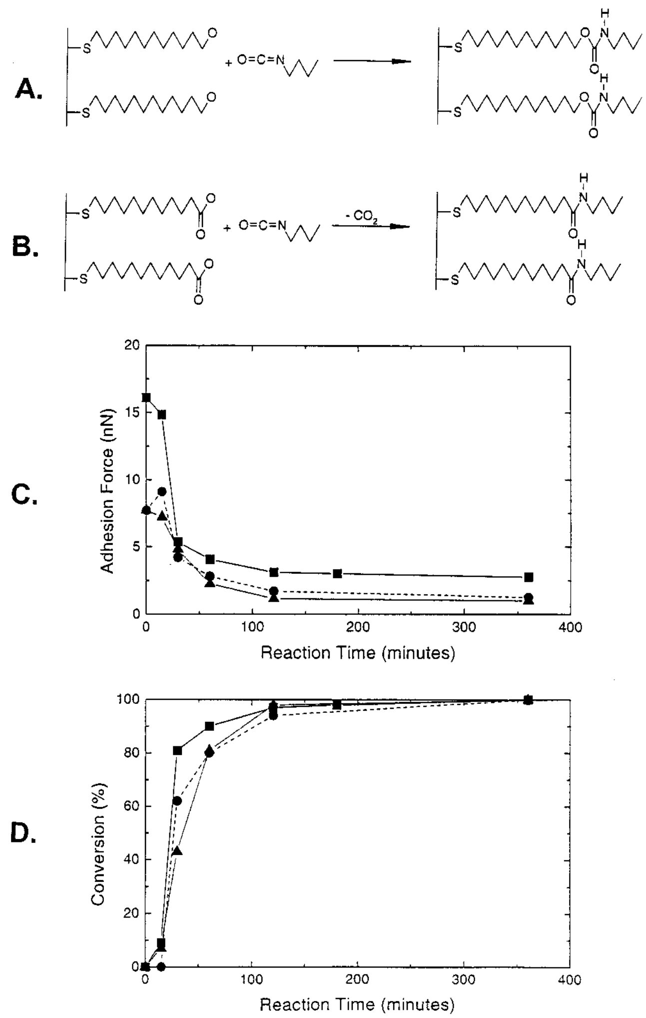

Figure 16. Surface chemical reactions probed with SFM. Reaction schemes of (A) an OH-terminated surface and (B) a COOH-terminated surface exposed to butyl isocyanate. (C) Decrease of adhesion force at an amide-modified tip as measured with SFM during the reaction of an OH-modified surface with catalyst (■), a COOH-terminated surface with catalyst (●), and a COOH-terminated surface without catalyst (▲). (D) “Microscopic” conversions calculated from these adhesion forces. Reprinted with permission from ref 189. Copyright 1997 American Chemical Society.

then rereduced the ferrocenyl group. The force required to separate the two surfaces was simultaneously measured through a series of force−distance curves. The voltammetric curve and resulting series of force curves are shown in Figure 17.

As the surface was cycled between the oxidized (cationic and more hydrophilic) and the reduced (neutral and more hydrophobic) forms of the ferrocenyl group, the adhesion between the tip and the surface changed and tracked the electrochemically induced transformation. For example, the adhesion (7.6 ± 0.5 nN) at the beginning of the anodic sweep decreased markedly by the end of the anodic sweep (∼1.2 ± 0.5 nN). Upon scan reversal, the adhesion returned to an average value of 6.4 nN. A comparison of a plot of adhesion versus applied potential to a plot of fractional surface coverage versus applied potential revealed that the changes in adhesion tracked the redox transformation of the immobilized ferrocenyl group.

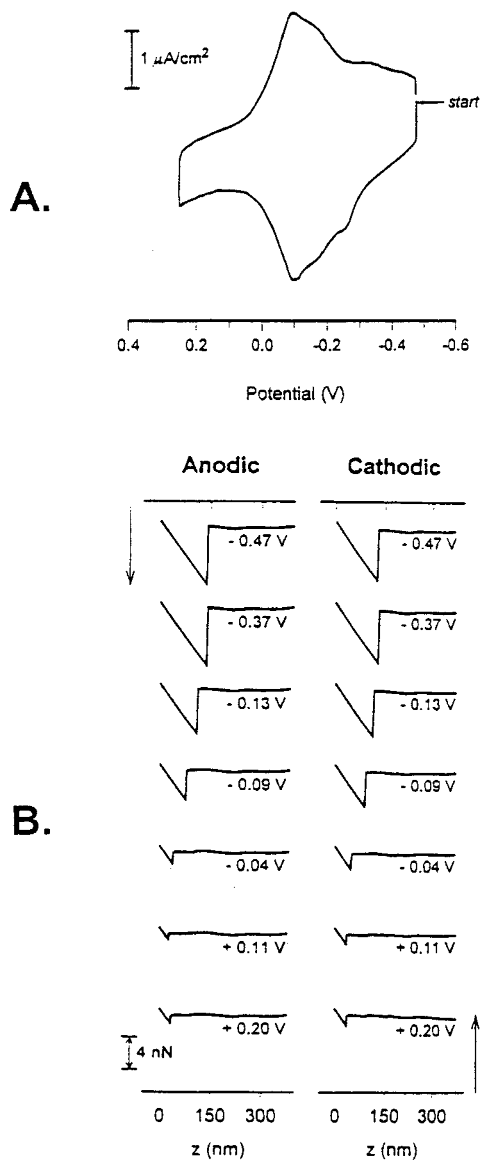

Figure 17. Real-time monitoring of an electrochemical transformation via adhesion-based SFM. (A) Cyclic voltammetric current−potential curve in the SFM cell for a ferrocene-terminated alkanethiolate monolayer chemisorbed on Au(111) in 1.0 M $HClO_4$. The applied potential is referenced against a pseudo-platinum reference electrode (+0.6 V vs SCE) and swept at a scan rate of 10 mV/s. (B) Force curves obtained during the cyclic potential scan in (A). The probe tip was a gold-coated Si_3N_4 tip modified with a monolayer of octadecanethiolate. Reprinted with permission from ref 160. Copyright 1996 American Chemical Society.

The change in adhesion upon the electrochemical transformation of the ferrocenyl headgroup was related to a change in the miscibility of the terminal groups at the two surfaces. That is, the reduced, more hydrophobic form of the ferrocenyl group is more miscible with the hydrophobic terminal group on the tip than is the oxidized, less hydrophobic ferrocenyl group. An earlier investigation of electrowetting phenomena by Abbott et al. on a similar redox system supports this assertion.[255] Thus, the decrease in adhesion indicated an increase in interfacial free energy between the probe tip and the sample surface and a decrease in the miscibility of the two surfaces at the microcontact.

Hudson and Abruña have also examined the use of adhesion measurements in electrochemical systems.[256] In this case, an electroactive polymer film (i.e., poly(vinylferrocene), PVF) was deposited onto a gold-coated tip and a gold electrode. At an applied potential where the film was held in its reduced, neutral form, the average adhesion force was 12.2 ± 0.3 nN. Upon oxidation to its cationic form, however, the measured adhesion force decreased to 3.2 ± 0.4 nN. This observation was attributed to differences in solvation energies in that the oxidized form of the film was more highly solvated than the reduced form of the film. Thus, the ability to break the microcontact was easier when the more solvent compatible form of the film was ruptured.

The ability to change the chemical composition of a tip in real-time opens the door for analyzing a variety of surfaces with the same tip. For example, Hudson and Abruña demonstrated that a tip modified with the neutral form of PVF interacts more strongly with surfaces terminated with CH_3 groups than those terminated with COO^- groups.[256] Conversely, tips modified with the oxidized form of PVF reversed the observed dependence. Therefore, the use of a SFM tip that can have its interfacial properties readily altered presents a potentially exciting strategy in evaluating surface structure and composition at reduced length scales, i.e., microminiaturized surface chemical analysis.

Taken together, the above results extend SFM into the arena of chemical analysis. Generally, changes in surface free energy are evaluated by contact angle measurements, a bulk wetting phenomena. However, the high degree of spatial resolution attainable by SFM can, to a degree, be viewed as extending surface free energy measurements to surfaces that contain microdomains of different surface free energies, thereby gaining insights into surface composition and structure.

B. Compositional Mapping

As discussed earlier, a wealth of information (i.e., adhesion, elasticity, and topography) can be gained by examining force curves. Up to this point, the discussion has been limited to chemical analysis performed at a single point within the $x-y$ plane of a surface. A natural extension of this analysis is the collection of information while the tip is scanned across the surface, thereby generating compositional maps of the above properties on a surface. In this portion of the review we discuss different strategies for mapping surface composition using SFM. In the first section we discuss force mapping, which involves the collection of individual force curves at discrete points across a surface. The next section deals with friction mapping, where the torsion of the cantilever is monitored while contact with the surface is maintained at a constant force. In the third and fourth sections we discuss briefly the compositional mapping of surfaces using the tapping and electric force modes of SFM, respectively. We note that it is also possible to map the viscoelastic properties of surfaces using force modulation SFM (FM-SFM);[69,257] this topic lies outside the scope of this review.

1. Force Mapping

Force mapping can be conducted by monitoring the approach portion of the force curve (regions 1−3 in Figure 2A) or the retraction portion of the force curve (region 5 in Figure 2A). Experiments performed in the approach portion of the force curve can be used to map electrostatic forces, while studies performed in the retraction portion are often used to map the adhesion properties of surfaces. Force mapping using the retraction portion of the force curve is the more commonly employed method and is discussed first. We note that force mapping has also been applied to numerous biological systems; results from these studies are presented in a later section.

One of the earliest demonstrations of the ability of SFM to map adhesion forces across surfaces was by Miyamoto and co-workers.[258] Using tips fabricated from tungsten, Si_3N_4, Al_2O_3−TiC, and diamond, adhesion forces were measured while scanning across uncoated and lubricant-coated (~2 nm thickness) hard disks. As expected, the measured adhesion forces were much lower in the presence of the lubricant. Somewhat surprisingly, tips fabricated from SiC showed very little adhesion even in the absence of the lubricant. These findings, though not fully understood, demonstrated the ability of SFM to map the distribution of adhesion forces across a surface, thus enabling studies aimed at delineating any heterogeneity in the chemical and physical properties of surfaces.

The effect of surface topography on the measured adhesion has been investigated.[259,260] A decrease in adhesion was found for localized regions of high curvature as observed in the topography of an undoped polycarbonate film, presumably due to a decrease in the area of the tip−sample microcontact.[260] Similar conclusions were reported for force maps of chromium films deposited on glass substrates, where adhesion contrast was observed only at boundaries between the metal and glass regions.[259] Thus, the influence of the surface topography must be accounted for when force maps of surfaces are collected.

Force mapping has also been employed to examine the adhesion properties of various monolayer systems.[248,261] In an early study, two types of monolayer systems were prepared: a Langmuir−Blodgett (LB) monolayer film coated on glass and subsequently polymerized by ultraviolet light, and a thiolate monolayer on a gold surface.[248] When imaged in air with a Si_3N_4 tip, the adhesion for the LB film was found to be lower than that of uncoated glass, as expected, because of the hydrophobicity of the coating terminus relative to the glass substrate. The adhesion force was found to depend on the contact area as discussed above. When portions of a pentadecanethiolate monolayer were mechanically removed from a gold surface, a clear difference in adhesion was observed between the monolayer film and the underlying glass substrate when examined in deionized water. Though not understood, the addition of ionic species to the solution, however, resulted in a loss of contrast in the adhesion image, in agreement with earlier reports.[262]

Further studies in this laboratory involved the use of force mapping to examine the orientational differences of crystalline and amorphous phases of a LB monolayer with a resolution of ~20 nm.[261] Spatial arrangements of functional groups are important in many processes, such as lubrication or biological recognition. The monolayer film consisted of a mixture of two phases: a liquid-crystalline phase where the tip only interacts with the terminal CH_3 groups, and a liquid-expanded phase where the tip interacts with the slightly less hydrophobic CH_2 groups of the alkyl chain. Importantly, the ratio of the adhesion forces of the two different phases agreed with predictions of the interactions of the two types of contacts through interfacial free energy considerations. The two different phases both form hard, fairly rigid structures, so differences in elastic contributions to the observed adhesion force were deemed insignificant. It was therefore concluded that the image contrast was associated with the difference in interfacial free energies of the two types of functional groups, suggesting the possibility of using adhesion for mapping orientational differences.

Rosa and co-workers have utilized SFM to map the elastic, electrostatic, and adhesive properties along with the topography of different polymer surfaces.[263,264] Topography, elasticity, and adhesion were investigated for a filler-enhanced polymer as a function of different strain states.[264] Filler-enhanced polymers are of great interest due to their combination of polymeric elasticity and filler reinforcement. However, the microscopic origins of the durability and strength of these systems are not well understood. In characterizing a natural rubber filled with carbon black, elasticity images verified that the carbon black filler was mechanically harder than the rubber and was randomly oriented in clusters within the unstrained polymer. Upon straining the polymer, linear structures appeared parallel to the strain direction and were assigned to the inhomogeneous deformation of the rubber. The filler clusters also aligned in the strain direction. While the elasticity images probed both surface and bulk properties, the adhesion images reflected only the surface interactions between the tip and sample. Thus, it was possible to discriminate between coated and uncoated filler clusters in the adhesion images. Images of the unstrained polymer showed the filler regions possessed a lower adhesion than the rubber matrix. Upon straining the polymer, the overall adhesion noticeably decreased; the decrease was explained by a decrease in adhesive contacts of the oriented polymer chains. Thus, the adhesion force images provided insight into the strain-induced changes in the polymer structure that may explain the changes in their bulk properties.

Up to this point, only force mapping using the retraction portion of the force curve has been discussed. However, recently several laboratories have extended the use of force mapping to monitor the approach portion of the force curve to map the electrostatic properties of surfaces.[263,265,266] The surface charge of a mica surface partially covered with a charged polymer was imaged in air by examining the attractive force at a tip−surface separation of 100 nm under relatively low humidity (24%).[263] Under these conditions, a lower attraction was observed on the uncoated mica regions presumably due to a lower surface charge than that of the polymer.

Other groups have conducted force mapping in solution to examine electrical double-layer interactions on patterned surfaces.[265,266] Miyatani and coworkers[265] successfully obtained maps of electrical double layers on patterned surfaces of SiO_2 and Al_2O_3. The patterns were imaged with a Si_3N_4 tip in a NaOH solution at a pH of 8.6. At this pH, both the tip (IEP $\approx$ 6.2) and the SiO_2 regions (IEP $\approx$ 2) of the surface were negatively charged and therefore possessed a double layer of Na^+ ions. In contrast, the Al_2O_3 regions (IEP $\approx$ 10) were positively charged and contained a double layer of OH^- ions. Force maps of the surface were consistent with the expectation of repulsive double-layer forces between the tip and the SiO_2 regions and attractive double-layer forces between the tip and the Al_2O_3 regions. Indeed, the ability to map the spatial distribution of charged solution–surface interfaces should lead to a greater understanding of many important chemical and biological processes dependent on ionizable surface functional groups.

Force mapping has seen limited use in the chemical analysis of surfaces thus far. However, continued improvement in techniques designed to decrease data acquisition times and increase image storage capabilities will likely result in widespread use of this powerful SFM technique. The remainder of this section deals with the development of methods to allow for the collection of force maps at scanning speeds comparable to those of conventional SFM modes.

A key figure of merit in force mapping experiments is resolution. Although force–distance curves can be measured and stored at high densities, this process can be very time-consuming and can require an extensive amount of memory for large-area, high-resolution maps. Therefore, a compromise exists between image acquisition time and the total number of force curves collected to produce the image. The number of force curves that can be collected per unit time is related to the oscillation frequency of the z-piezo during approach and retraction. Ideally, this frequency should be maximized to decrease analysis time.

However, it is often necessary to operate the z-piezo at lower oscillation frequencies (10–100 Hz) and collect many points along each force curve (i.e., higher sampling intervals).[259,267–272] If the sampling interval for each force curve is too large, errors can occur in the determination of adhesion since the actual jump away from the contact point may not be accurately sampled. This situation is especially true when force maps of biological samples are collected, where small adhesion forces are commonly measured and nonspecific interactions may contribute substantially to the observed adhesion force.[270] Thus, for most biological applications, as discussed later in section 4, long image acquisition times (>15 min per image) are required. In addition, the majority of these studies exported the collected force curve data to analysis and/or image generation programs, further increasing total acquisition times.[259,267,268,271,272] The inability to evaluate image quality in real-time and make any necessary fine-tuning to instrumental parameters to optimize data collection is problematic to such methods.

To decrease the overall data collection analysis time, a great deal of work has centered around the development of techniques to collect force–distance curves and display force maps online at regular SFM scan speeds.[248,261,263,264,266,273] The majority of these techniques are based on the continuous cycling of the vertical movement of the z-piezo at relatively high frequencies (0.1–5 kHz) while scanning. In combination with timing electronics to store data at particular tip–sample separations in each force curve, it is possible to extract information regarding topography, elasticity, adhesion, and/or electrostatic force simultaneously.

An alternative method for collecting spatial adhesion information of a surface is through the generation of a so-called “differential lateral deflection” (DLD) image.[273] These images are attained by the subtraction of friction trace and retrace images, but only qualitatively resemble those from standard force maps. Thus, while DLD imaging allows for acquisition of spatial adhesion information with reduced times and at greater pixel densities, quantitative information is not obtainable with this method.

van der Werf and co-workers have described a method of force mapping that employs high z-piezo sampling frequencies.[248,261] In this method, a triangular waveform is applied to the z-piezo at frequencies up to 0.55 kHz. The tip and sample are brought into contact until a preset cantilever deflection is reached, at which point the z-piezo voltage is stored in a sample/hold circuit and then the retraction cycle is initiated. A peak detector records the adhesion value in the retraction cycle, allowing for the display of adhesion force online at scan rates approaching those of conventional SFM modes.

By applying sinusoidal modulation to the z-piezo during force mapping in a so-called “pulsed force” mode (PFM), it is possible to obtain force curves at a much higher frequency (up to 5 kHz) than those of triangular methods.[263–265] When triangular modulation is applied at frequencies above 0.1 kHz, mechanical harmonics are generated that destabilize the piezo, the cantilever holder, or the cantilever itself.[263] This problem is avoided by applying a sinusoidal modulation. Using PFM, topography, local stiffness, and adhesion can be mapped simultaneously. At a typical modulation frequency of 1.5 kHz, an image of 256 $\times$ 256 points can be obtained in $\sim$2.5 min, which is comparable to conventional modes of SFM.

The ability of these newly developed force mapping methods to collect and display real-time adhesion information in two dimensions represents a powerful addition to the arsenal of SFM techniques. The next section of this review deals with another method for mapping the chemical properties of surfaces, friction force microscopy.

2. Friction Mapping

In this section we describe the application of SFM-based friction measurements to the mapping of

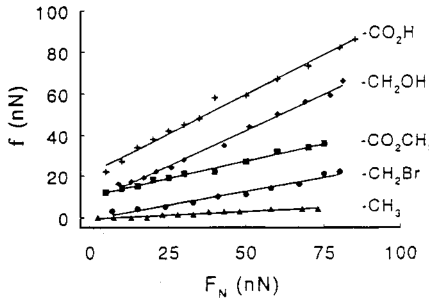

Figure 18. Friction (f) vs contact load (F_N) for the same uncoated Si_3N_4 tip and a series of monolayer-coated surfaces that were prepared by chemisorption of different functionalized alkanethiols ($X(CH_2)_nSH$, where $n = 15$ for CO_2H, CH_2OH, and CO_2CH_3, $n = 17$ for CH_3, and $n = 20$ for CH_2Br). Reprinted with permission from ref 127. Copyright 1995 American Chemical Society.

surface composition and related architectural details of organic thin films. Most of the examples, as a consequence of their value as model test platforms, involve organized monolayer or multilayer films. We first begin by examining single-component or multicomponent systems whose frictional properties do not change with time (i.e., static systems). At the end of this section, we discuss the use of friction mapping to examine dynamic processes, such as chemical reactions. We note that several reviews covering other important topics in this area such as polymer imaging and characterization are available.[69,274−280] Therefore, discussions related to the friction mapping of polymers are not included here.

a. Static Systems. The identity of the functional groups at the outermost few angstroms of microscopic contacting areas, i.e., the surface free energies, determines the contrast when the frictional properties of a surface are mapped.[281−283] This dependence is confirmed by characterizations in dried, high-purity argon of the friction force between an uncoated Si_3N_4 tip and a variety of end-group-derivatized alkanethiolate monolayers deposited at gold-coated surfaces. Plots of friction (f) versus contact load (F_N) for a single Si_3N_4 tip and a series of monolayer surfaces with varied terminal groups are presented in Figure 18.[127] These data showed that the chemical identity of the terminal groups at the tip−sample microcontact has a profound effect on the resulting friction. These plots also revealed that the dependence of f on F_N is linear, with the coefficient of friction (i.e., the slope of the plots) increasing as the surface free energy of the terminal group increased. This clear correlation between friction and the surface free energy of the tip−sample microcontact provides a basis for chemically sensitive compositional mapping.

The dependence of f on terminal group identity was also examined by studying the effect of tip composition. Examples of such findings are shown in Figure 19 for three different tips (COOH, CH_3, unmodified) and two different samples (COOH and CH_3). For all tip−sample combinations, f again exhibited a linear dependence on F_N. The largest friction was found at the COOH−COOH contact (Figure 19A), followed by the CH_3−CH_3 contact (Figure 19B) and, last, by the COOH/CH_3 and CH_3/COOH contacts (parts A and B, respectively, of Figure 19). Thus, the maximum friction occurred at microcontacts composed of the same terminal groups. These dependencies, which are also in agreement with the trends observed between adhesion and terminal group identity,[126] suggest that the careful selection of tip composition may provide a platform for an enhanced friction contrast when different terminal groups are imaged.

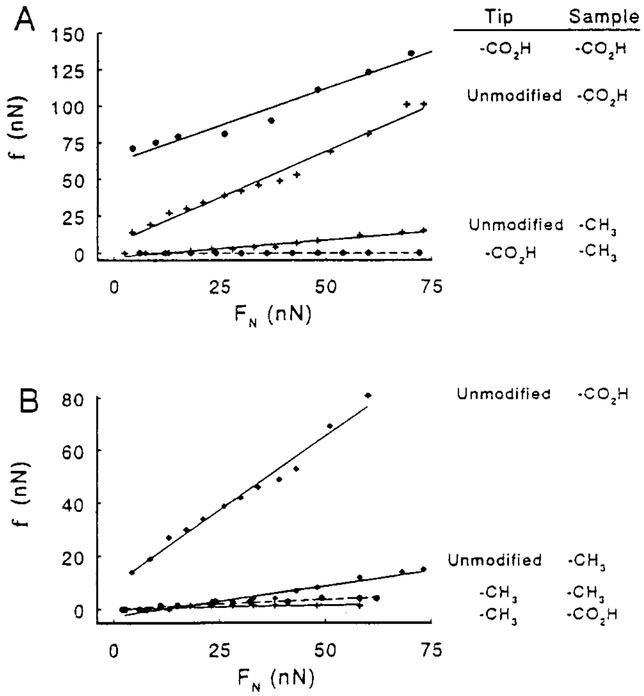

Figure 19. Friction (f) vs contact load (F_N) for a number of different tip−sample combinations. The terminal group functionality of the tip and sample for each data set is specified at the right of the plots, where the number of CH_2 groups in the alkanethiolate chain is listed in Figure 18. All unmodified tips are Si_3N_4 surfaces. (A) f vs F_N for unmodified tips and COOH tips in contact with CH_3 and COOH surfaces. (B) f vs F_N for unmodified tips and CH_3 tips in contact with CH_3 and COOH surfaces. Reprinted with permission from ref 127. Copyright 1995 American Chemical Society.

Having developed a basis for the dependence of f on terminal group identity, the issue now becomes how to create a surface composed of a controlled distribution of different terminal groups. The terminal groups should be distributed at dimensions such that the potential of this SFM characterization technique to resolve features at a nanometer-length scale can be assessed. To investigate this capability, Green and co-workers[127] prepared samples of a spatially segregated, partially formed bilayer structure comprised of mercaptohexadecanoic acid (bottom layer) and stearic acid (top layer). This type of architecture is depicted in Figure 20 and forms as a consequence of head-to-head hydrogen bonding of the carboxylic acids. Thus, the topographic differences can be used to identify whether the tip is in contact with the high surface free energy COOH terminal group of the layer chemisorbed to gold or with the low surface free energy CH_3 terminal group of the second layer.

Figure 20 shows topographic and friction images obtained with an unmodified Si_3N_4 tip for this type

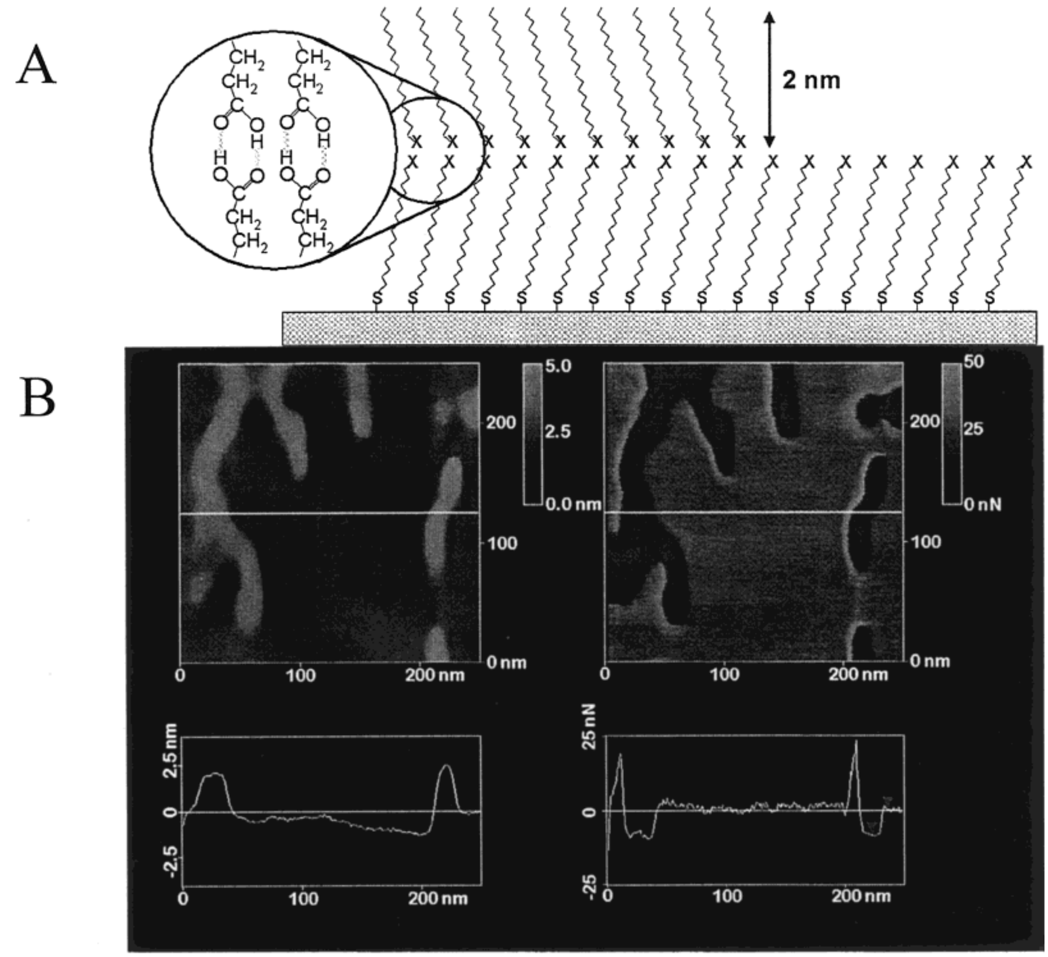

Figure 20. (A) Idealized depiction of a partially formed bilayer comprised of a mercaptohexadecanoic acid monolayer chemisorbed to a gold surface (bottom) and a stearic acid layer (top). (B) 250 nm × 250 nm SFM topographic and friction force images of partially formed bilayers comprised of mercaptohexadecanoic acid (bottom layer) and stearic acid (top layer) as depicted in (A). Height data and friction data were collected simultaneously. The left is a topographic image and the right is a friction image of a bilayer using an unmodified Si_3N_4 tip. The normal force between the tip and sample was ~10 nN. The topographic features observed in the cross-section on the bottom left are ~2 nm in height, and the friction variation on the bottom right is ~15 nN. Reprinted with permission from ref 127. Copyright 1995 American Chemical Society.

of surface. The topographic image revealed that the size and separation of the domains for the second layer were on the order of nanometers. Importantly, the friction image displayed the correspondence expected from the plots in Figure 18 in that the friction detected at the COOH terminal groups was greater than at the CH_3 terminal groups. Furthermore, an analysis of the image revealed a mapping resolution of ~10 nm, as judged from the distance clearly separating the two architectures. These findings firmly establish the ability of SFM-based friction measurements to map the terminal group composition at a very high level of resolution. Similar results have been reported, for example, by Frisbie et al.[126] using photolithographically patterned samples and by Wilbur et al.[183] using patterns formed by microcontact printing. In addition, Zhou and co-workers[284] have shown that friction can be employed at a semiquantitative level through correlations with the relative surface coverage of mixed monolayers determined by X-ray photoelectron spectroscopy.

Hayes et al.[161] and Lio et al.[285] have used this capability to study the phase distribution of mixed monolayers. Hayes et al. reported friction measurements for a mixed monolayer of 4-aminothiolphenolate (4-ATP) and octadecanethiolate (ODT) on gold.[161] Interestingly, at low coverages of 4-ATP, the phenolate existed as small, discrete islands imbedded in an ordered film of ODT. At higher coverages of 4-ATP, however, both distinctly separated phases and mixed regions of the two components were observed. These results were evaluated in terms of mixing thermodynamics to delineate the electrochemical behavior of 4-ATP as a function of coverage.

Koutsos and co-workers used SFM to study a mixed-monolayer system comprised of dodecanethiol and thiol-derivatized polystyrene chemisorbed on gold from mixed toluene solutions.[286] From the assessment of the topographic and friction images, islands of 3.9 nm diameter were identified as individual collapsed polymeric chains embedded in the dodecanethiolate monolayers. This investigation demonstrated the ability of SFM to map more complex surface structures.

In a particularly intriguing application by Werts and co-workers, thiol-modified tips were used to characterize a star copolymer (polystyrene (PS) and poly(2-vinylopyridine) (PVP)) to examine the resolu-

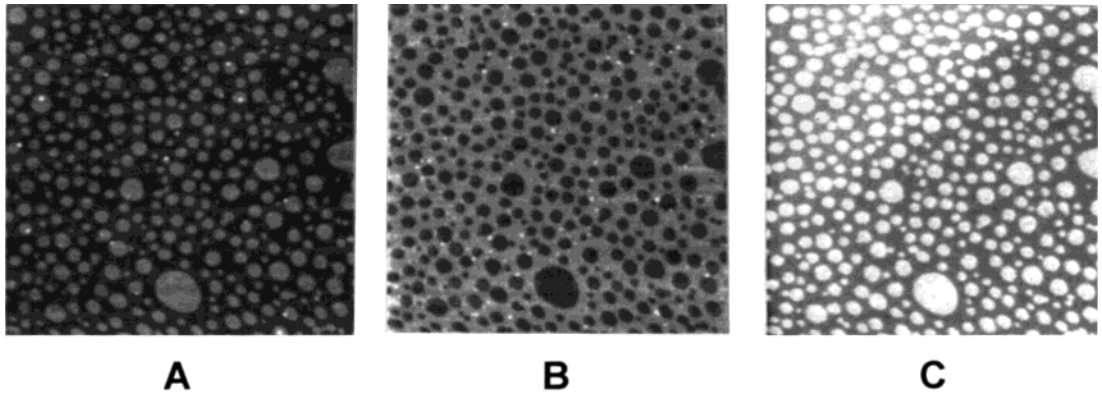

Figure 21. Simultaneous SFM images (3 μm × 3 μm) of topography (A), friction (B), and elasticity (C) for a monolayer film prepared from a 1:1 molar mixture of BA and PFECA at pH 6.6. (A) Topography map with islandlike hydrocarbon domains ~80 nm (bright regions) in diameter on the fluorocarbon film. (B) The friction map shows lower friction (dark) on hydrocarbon islands and 3× higher friction (bright) on the fluorocarbon underlayer. (C) The elasticity map shows a higher Young's modulus (brighter) on the hydrocarbon domains. The relative difference in elasticity is 0.1 ± 0.03 GPa. Reprinted with permission from ref 289. Copyright 1994 American Chemical Society.

tion capabilities of the friction mapping technique.[287] This capability was realized when imaging was done with a COOH-modified tip but not with a CH_3-modified tip. With a COOH-modified tip, features as small as 5 nm could be distinguished. Such resolving power arises from the fact that the friction coefficient for a COOH-modified tip on PVP is 3 times larger than that on PS. The difference in the friction coefficients for a CH_3-modified tip on PVP and PS is, in contrast, much smaller. This result not only shows that chemically sensitive mapping can be applied to complex polymeric structures, but also demonstrates the role of the friction coefficient in determining the observed resolution. That is, the greater the difference in the friction coefficients between different surface phases, which defines the magnitude of the contrast, the higher the possible imaging resolution.

Friction measurements have also been applied to characterize organized multilayer structures prepared by the Langmuir−Blodgett (LB) technique. In the LB technique, organic monolayers of amphiphilic molecules are first organized at the air−water interface and then transferred to solid substrates to form mono- or multilayer architectures. This technique can also be used to create layers where the composition alters within a layer as well as between layers.

Overney and co-workers were the first to apply SFM to study phase-separated LB films.[288,289] Indeed, this work was the first to realize the potential of SFM as a high-resolution analytical technique for compositional mapping. One set of experiments was carried out using an unmodified Si_3N_4 tip to probe LB films formed from a 1:1 mixture of behenic acid (BA) and a partially fluorinated carboxylic acid ether ($C_9F_{19}C_2H_4{-}O{-}C_2H_4{-}COOH$) (PFECA) both bound ionically to a common cationic polymer and transferred onto silicon surfaces.[289]

Figure 21 presents three types of images for this system: topography (A), friction (B), and elasticity (C). Although the details of the formation and structure of the LB film are not fully understood, the topographic image showed that the transferred film was composed of two regions, each with a different height. The height difference indicated that the small domains (~80 nm in diameter) were composed of behenic acid amphiphiles sequestered as a partial bilayer film on top of the fluorinated amphiphile layer. The observed friction image showed a clear correspondence with the domains in the topographic image, demonstrating the capability of friction as a contrast mapping technique. However, elasticity differences may also contribute to the detected frictional contrast as revealed by an observed difference in the rigidity of the two architectures. This finding reflects the dependence of friction measurements on contact area. A softer material (i.e., a material with a lower Young's modulus) yields a higher contact area and therefore a higher frictional force.[158]

Mechanical issues were also found to play an important role in the friction contrast as well as the adhesion contrast detected for phase-separated domains of LB films from disteroylphosphatidylethanolamine (DSPE) and dioleoylphosphatidylethanolamine (DOPE).[290] It was speculated that the friction contrast resulted from the relative molecular disorder of the two phases as well as the area of microcontact established between the tip and each phase. Bar et al.[158] have carefully elucidated how differences in cohesive interactions, which affect elasticity, at structures of the same packing density can contribute to the observed adhesion and friction. Other researchers[291−293] have also shown that information related to adsorbate orientation and packing density can affect the observed friction. Investigations using SFM to evaluate the interplay between chain length and friction and wear of thiol- and silane-based monolayers have also been conducted.[131,285,294,295]

To investigate whether friction contrast due solely to orientation differences could be observed by SFM, Wong and co-workers[187] used uncoated tips to map the orientation differences of the terminal CH_3 groups of gold-bound *n*-alkanethiolates. Figure 22 depicts the idealized structural features of the system employed. The origin of the friction difference between the tip and different terminal group orientations arises from the increase in surface free energy when the dipole moment of the methyl end group is canted more from the surface normal when the number of methylene groups in the chain (*n*) is even

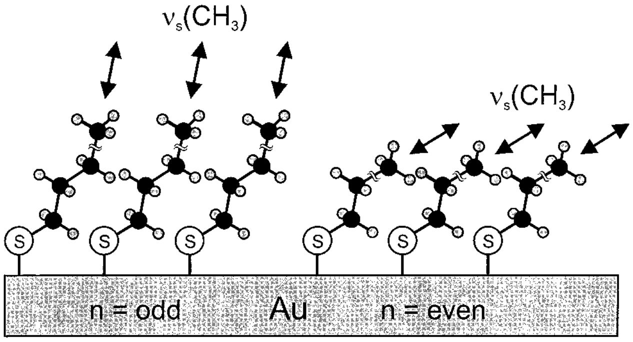

Figure 22. Idealized structures for *n*-alkanethiolate monolayers chemisorbed at gold. The structure on the left is for an adlayer with an odd number of methylene groups in the alkyl chain, whereas that on the right is for an adlayer with an even number of methylene groups in the alkyl chain. The spatial dispositions of the dipole moment of the terminal methyl groups are approximated by the crossed arrows. Reprinted with permission from ref 187. Copyright 1998 American Chemical Society.

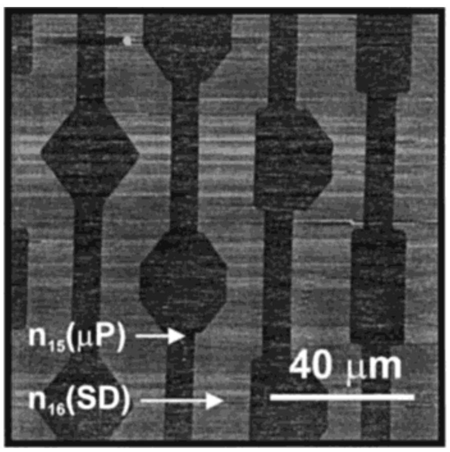

Figure 23. 120 μm × 120 μm friction image using a Si_3N_4 tip (brighter contrast corresponds to higher friction) of an *n*-alkanethiolate monolayer patterned on smooth gold by microcontact printing (μP) of hexadecanethiol ($n_{15}(\mu P)$), followed by solution deposition (SD) of heptadecanethiol (n_{16}(SD)). Reprinted with permission from ref 187. Copyright 1998 American Chemical Society.

($\sim$53°) compared to when *n* is odd ($\sim$26°). Because of this difference, friction is expected to be higher at an adlayer where *n* is even than where *n* is odd.

Figure 23 shows that these differences in orientation can be mapped by friction imaging. This image is of a surface created by microcontact printing (μP) a monolayer of hexadecanethiolate ($n_{15}(\mu P)$) in a predefined pattern on a gold surface, followed by the solution deposition (SD) of heptadecanethiol (n_{16}(SD)) to fill in the areas not coated by the stamping process. The image shows that the domains of n_{16}(SD) have a higher friction than those of $n_{15}(\mu P)$, demonstrating the ability to apply friction to orientation mapping. Last et al.[296,297] and Nisman et al.[298] have recently developed this capability on other surface systems.

McKendry and co-workers[299] were the first to report the use of SFM to discriminate between chiral molecules immobilized on surfaces. By attaching acylated phenylglycine T, which is chiral, to a tip via a long, flexible tether, differences in both the adhesion and friction for an array of immobilized madelic

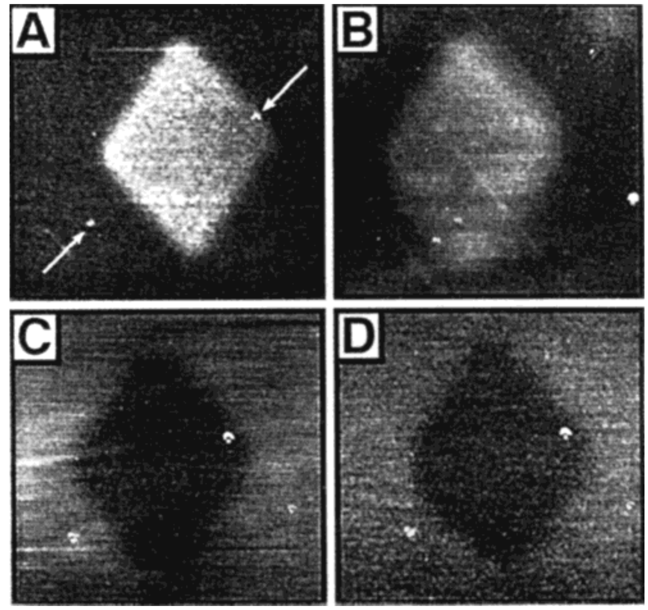

Figure 24. Friction images using a COOH-modified tip of a patterned monolayer sample where the inner square contains a COOH-terminated monolayer and the surrounding area consists of an OH-terminated monolayer. The images were recorded with pH values of (A) 2.2, (B) 4.8, (C) 7.2, and (D) 10.3. Each of the four images corresponds to 30 μm × 30 μm areas. The brighter regions correspond to areas of higher friction. Reprinted with permission from ref 212. Copyright 1997 American Chemical Society.

acid enantiomers were detected. This discrimination mechanism reflected a combination of hydrogen-bonding and $\pi-\pi$ interactions that formed transient diasteromeric complexes between the tip and the two surface-bound enantiomers. Impressively, the chiral sensitivity of SFM was demonstrated by scanning across a patterned surface with two micrometer wide alternating stripes of *R*, *S*, or racemic mandelic acid. While no height difference was found in the topographic images, friction differences were clearly evident when using a tip modified with only one enantiomer of phenylglycine T. No frictional difference was observed when using a tip modified with the racemate. The ability to discriminate chiral materials may allow SFM to become an important technique in the pharmaceutical arena where chirality is of fundamental importance.

b. Dynamic Systems. In this section we discuss the use of friction mapping to examine dynamic processes. Vezenov et al.[212] demonstrated that the friction between a tip and sample can be affected by the changes in solution pH. Using a COOH-modified tip and surfaces composed of COOH or OH terminal groups, friction was found to be not only dependent on the chemical identity of the terminal group, but also sensitive to the changes in ionization state induced by alterations in solution pH. As expected, changes in pH resulted in differences in the friction detected at the ionizable COOH surface, but not at the nonionizable OH surface.

Figure 24 shows the effect of pH on the observed friction of a sample photolithographically patterned with COOH terminal groups in small square-shaped domains surrounded by OH terminal groups. Using a COOH-modified tip, the friction contrast for the two

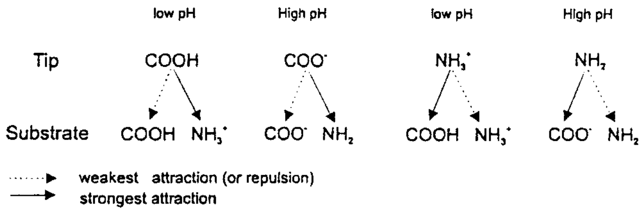

Figure 25. Scheme depicting the strength of tip−substrate interactions for ionizable terminal groups at high and low pH. Reprinted with permission from ref 128. Copyright 1997 American Chemical Society.

different domains changed with pH. At pH 2.2 (A) and 4.8 (B), the friction at the COOH domains was greater than that at the OH domains. The contrast, however, inverted as the pH increased to 7.2 (C) and 10.3 (D). Though not shown, the contrast change occurred between pH 5 and pH 6, which is close to the pK_a for the surface-bound COOH groups. Interestingly, these changes were detected only when using a COOH-modified tip. That is, imaging with an uncoated Si_3N_4 tip did not reveal a pH-dependent contrast, a compelling argument for the value and versatility that may be obtained by controlling the surface composition of the tip.

van der Vegte and co-workers carried out a related study on chemically specific tip−surface interactions in their exploration of the chemical imaging of terminal groups.[128] Building on an examination of the type and strength of the interactions between the protonated and deprotonated forms of COOH and NH_2 groups from adhesion measurements and the correlations with plots of f vs F_N, the dependencies in Figure 25 were developed. These results, which can be interpreted on the basis of electrostatic and hydrogen-bonding considerations, were used successfully as a basis for the prediction of the expected contrast in the friction images for compositionally patterned surfaces.

Werts and co-workers[189] used friction to monitor the conversion of OH or COOH terminal groups to butyl groups by reaction with butyl isocyanate. These reactions were also monitored in real-time with adhesion measurements, as discussed earlier. Using a tip terminated with an amide group and a CH_3/COOH patterned surface or a CH_3/OH patterned surface, the gradual conversion of the COOH or OH groups to CH_3-terminated groups was monitored. Figure 26 contains images documenting the conversion of a CH_3/COOH patterned surface prepared by microcontact printing during exposure to butyl isocyanate. As is evident, the friction of the COOH regions slowly decreased with exposure time, with the conversion completed in 360 min. Interestingly, the friction across the different regions was indistinguishable after 360 min, indicating that the conversion was effectively homogeneous across the surface.

Wang et al.[300] used SFM to evaluate the tip-assisted base hydrolysis of an ester-terminated alkanethiolate monolayer on Au(111). As proposed, contact imaging accelerated the base hydrolysis of an ester functionality buried a few angstroms below the boundary between a thiolate adlayer formed on gold and 10 mM KOH. That is, the tip mechanically disrupted the steric barrier imposed by the neighboring adsorbates, facilitating access by OH^- to the buried acyl carbons. The in situ topographic and friction images in Figure 27 present the results obtained after a 1.0 μm × 1.0 μm area located to the right of the center of the images was continuously scanned for 1 h. There was no detectable difference between the scanned and unscanned areas in the topographic image. There was, however, a subtle, but detectable increase in the friction in the area scanned repetitively. This increase was consistent with that observed on a fully hydrolyzed sample, confirming the viability of tip-assisted hydrolysis in nanofabrication.

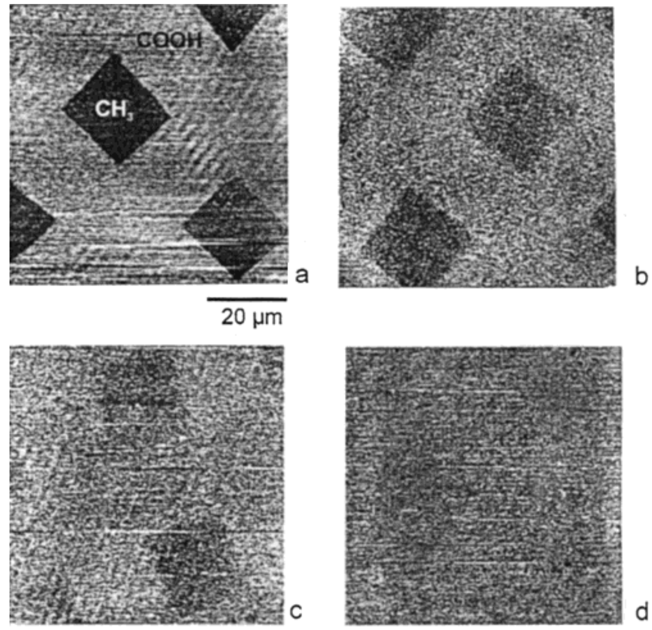

Figure 26. Friction force images (70 μm × 70 μm) using an amide-coated tip and a CH_3/COOH patterned surface before and after the reaction with butyl isocyanate. The bright areas represent regions of high friction. The disappearance of contrast is observed when the acid surface is converted into a CH_3-terminated surface. Before reaction (a) and after (b) 30 min, (c) 90 min, and (d) 360 min. Reprinted with permission from ref 189. Copyright 1997 American Chemical Society.

3. Tapping Mode Mapping

The chemical sensitivity of friction mapping may become obscured in cases where the sample surface has significant topographic variations.[131,301,302] In such situations, imaging in tapping mode (TM-SFM) has been shown to be very effective in obtaining chemical information. These images are usually presented in terms of the phase shift of the tip response that is sensitive to adhesion interactions with the sample.

Using partially formed bilayers, Finot and McDermott[71] were the first to show that TM-SFM can distinguish between segregated domains of different terminal groups. The phase images demonstrated that the phase shift of an oscillating Si cantilever was sensitive to the differences in the identity of the terminal group and not to the elasticity of the organic architecture, a concern with some types of systems.[303−306] Finot et al. note, however, that their demonstration was conducted with a film designed to minimize the effects of elasticity on the measure-

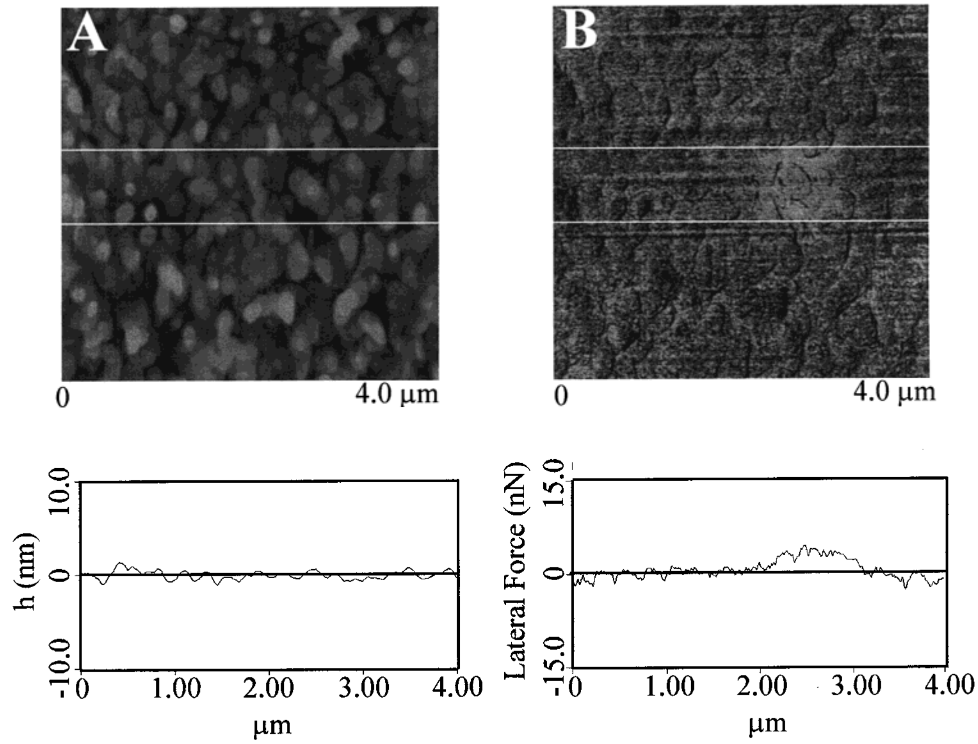

Figure 27. In situ topographic (A) and friction (B) images (4.0 μm × 4.0 μm) and cross-sections of an ester-terminated monolayer chemisorbed at Au(111) after immersion for 1 h in aqueous 10 mM KOH. The *y*-axis of the cross-sectional profiles for (A) and (B) are for height and friction, respectively. These images were acquired using an uncoated Si_3N_4 tip at a load of ∼25 nN and scan rate of 10 Hz after repetitively scanning for 1 h at a load of ∼25 nN in the 1.0 μm × 1.0 μm area that is evident to the right of the center in the friction image. Both cross-sectional plots represent the results of averaging cross-sectional analyses. Reprinted with permission from ref 300. Copyright 1997 American Chemical Society.

ment, and that the elasticity of each system should be evaluated on a case-by-case basis.

Noy and co-workers[70] have also explored the capability of TM-SFM in chemically sensitive mapping. In addition to findings in agreement with Finot et al.,[71] an examination of the effects of the contacting liquid was performed. By varying the relative composition of a water/methanol mixture, the magnitude of the phase shift could be altered according to the magnitude of solid−liquid interfacial free energies. In other words, changing the solvent composition can lead to different phase shifts for regions of different composition. Since the phase shift represents another contrast mechanism in chemically sensitive mapping, alterations in the composition of the contacting liquid offer a means to enhance contrast in a manner similar to that realized for changes in tip composition. We note that TM-SFM has also been employed to map the presence of embedded cytochrome *c* oxidase within the rolling hill topography of an electrode-supported lipid bilayer membrane.[307]

4. Electric Force Mode Mapping

Compositional mapping of surfaces can also be conducted by the electric force mode of SFM (Figure 3D).[82,83,85,308,309] In this mode, information on surface charge, contact potential, and/or dielectric constant can be obtained. This mode operates in the noncontact portion of the force curve (region 2 of Figure 2A). Therefore, the contrast observed in the electric force mode can be based purely on chemical information (i.e., surface charge, molecular dipole moment, dielectric properties) and not on the mechanical properties of the sample. Fujihira and co-workers have used this mode to characterize a phase-separated LB film, where the contact potential difference between domains composed of hydrocarbon and fluorocarbon components was imaged.[83] The contact potential difference resulted from differences in the surface dipole moments of the terminal CH_3 and CF_3 groups, serving as a means for identification.

Another interesting application of the electric force mode of SFM is the mapping of adsorbed water films on surfaces. Although a recent study using contact mode observed the transport of water between a tip and surface,[310] it is difficult to image thin water films in contact mode due to the softness of such layers and the induced capillary forces. However, the noncontact nature of the electric force mode makes this technique more amenable to these studies.

Hu and co-workers have used the electric force mode to monitor water film growth on a mica surface induced by changes in relative humidity.[84] During these investigations, the researchers found that the condensation of water on these surfaces occurred in two distinct structural phases. Up to ∼25% humidity, water film growth proceeded by forming two-dimensional clusters less than 100 nm in diameter. Above 25% humidity, a second structural phase appeared in addition to the first that formed large two-dimensional islands with geometrical shapes in epitaxial relation with the underlying mica lattice. The growth of the second structural phase was completed when the humidity reached ∼45%. The reverse process of evaporation was also imaged. We note that details concerning the condensation process of water[84,311] and glycerol[312] on mica have been reported, as well as for sulfuric acid on aluminum[313] and KOH on graphite.[314]

IV. Biochemical Analysis Using SFM

The high spatial resolution of SFM, along with its compatibility with liquid environments, has provided an unprecedented opportunity for exploring a wide range of biological problems.[49,50,61,315−320] We focus in this section on how SFM has been used as a chemical analysis tool in biological systems through the measurement of ligand−receptor interaction forces, in DNA, and in several novel formats for biological assays. The imaging aspects of SFM in the biological sciences have previously been extensively reviewed.[316]

A. Measurement of Ligand−Receptor Binding Forces

Little is known about the forces that govern ligand−receptor binding, the process responsible for the high level of molecular recognition operative in biological systems. This process often exploits sets of paired noncovalent (e.g., hydrogen-bonding) bonds that form between binding partners in a spatially defined motif. Several techniques have sufficient sensitivity (0.01−1 nN) to detect the intermolecular forces operative in ligand−receptor binding. These methods, employing surface force,[321,322] pipet suction,[323] and magnetic force[324] instruments, however, lack the spatial resolution requisite to detect an individual recognition event. Optical trapping[325−330] is sufficiently sensitive but has a dynamic range that limits the breadth of the detectable force. In contrast, SFM combines a high force sensitivity (theoretically 10^{-5} nN),[331] a high dynamic range (0.001−5000 nN),[332] and a high positional accuracy (0.01 nm) with operational compatibility in physiological environments. In addition, some types of tips have a radius of ∼10 nm, which can translate to contact areas on the order of square nanometers (see Table 3), depending on the elastic properties of the surface. As such, SFM is an attractive analytical technique for delineating isolated ligand−receptor interactions.

To determine these types of interaction forces with SFM, one of the binding pair partners is immobilized on a tip and the other on a surface. The adhesion force is then determined from the pull-off experiment depicted earlier in region 5 of Figure 2A. The interpretation of these data, however, may be complicated by contributions from nonspecific interactions. Nonspecific interactions can arise from an improper spatial orientation of the ligand and/or receptor that prohibits specific binding during the approach cycle and/or while in contact. The challenge then is to identify those interactions that are specific, as opposed to nonspecific, in nature. This separation can be accomplished by conducting control experiments where, for example, the binding site on one of the partners in the pair is blocked. Because of the often random spatial orientation of the binding partners on the tip and surface, it is usually necessary to collect several hundred individual force curves to determine a distribution of binding events.

1. Biotin–Avidin Interactions

Many of the initial investigations using SFM to probe biomolecular interactions focused on the extensively studied biotin−avidin system.[146,332−340] This well-characterized system was attractive as a starting point because of its high binding affinity ($K_d = 10^{-15}$ M), commercial availability, and well-developed immobilization chemistry.

The first report on this system[146] determined the rupture forces between a biotinylated glass microsphere (15 μm radius) that was mounted on the tip and streptavidin immobilized on mica. The average observed adhesion force (0.340 ± 0.120 nN ($n = 42$)) was notably larger than that found between biotinylated glass microspheres and a blocked streptavidin surface (0.060 ± 0.040 nN ($n = 30$)). Thus, the adhesion force detected at the contact was assigned to the force required to rupture specific biotin−streptavidin bonds. On the basis of an estimated contact area of 880 nm^2, this rupture force corresponded to no more than 10 streptavidin molecules; however, steric issues probably reduced the actual number of specific interactions to only a few binding pairs.

A parallel investigation[338] functionalized a Si_3N_4 tip with avidin and measured interactions with biotinylated agarose beads. To enhance the ability to detect an individual binding event, however, the number of available biotin sites on the agarose beads was reduced by blocking with avidin. Force curves for these experiments are presented in Figure 28, where curves A−C correspond to approach and retraction data before (curve A) and after (curve B) the agarose beads were blocked with avidin, and a magnification (curve C) of a bead blocked with avidin. The difference in the retraction portions of the force curves in (A) and (B) demonstrates the effectiveness of blocking, resulting in the ability to examine individual binding events as revealed in curve C where the adhesion force that must be overcome before breaking the microcontact is assigned to the last rupture event.

The rupture forces from more than 300 retraction experiments are summarized in the histogram in part D of Figure 28, which reveals the quantization of rupture forces in multiples of 0.160 ± 0.020 nN. This value was attributed to the interaction of a single biotin−avidin binding pair. Experiments using agarose beads modified with desthiobiotin and immunobiotin, two analogues of biotin that have lower binding affinities for avidin, supported the validity of the measurements in that the decreases observed in the rupture forces qualitatively tracked with the lower affinity constants. This line of experimentation also found that the rupture forces did not correlate with changes in free energy, but rather with the enthalpy of activation, indicating that dissociation is an adiabatic process and that any entropic changes occur after rupturing.[338] A similar conclusion was reached in an investigation of correlations between SFM-determined interaction forces and the thermo-

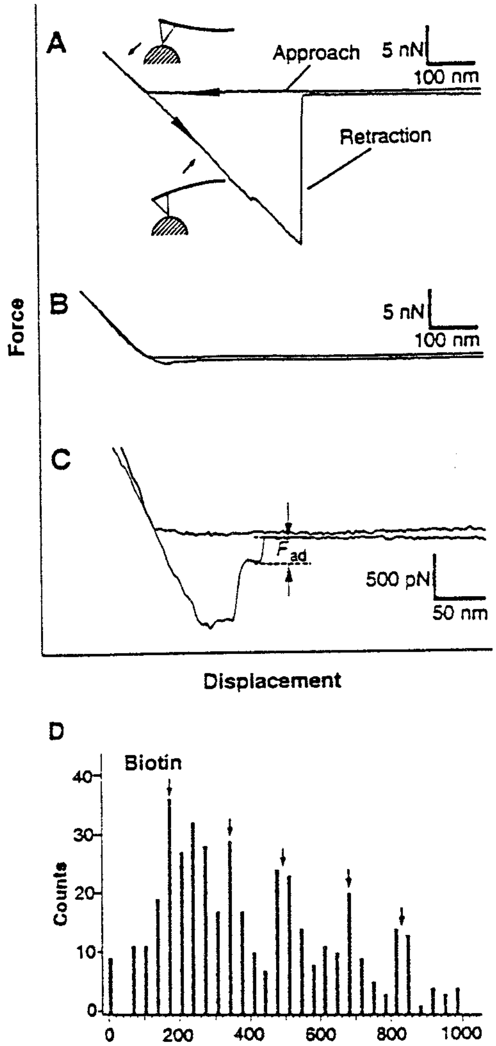

Figure 28. Force−distance curves for an avidin-modified tip interacting with a biotinylated agarose bead (A) before and (B) after blockage with an excess of free avidin. (C) Magnification of a force−distance curve on a biotinylated agarose bead approximately 95% blocked with free avidin. The detected rupture force (F_{ad}, pN) is plotted in the histogram shown in (D). Reprinted with permission from ref 338. Copyright 1994 American Association for the Advancement of Science.

dynamics of ligand−receptor binding using a biotinylated tip and surfaces modified with site-directed mutations of streptavidin.[339]

Several of the successes in characterizing this system are the result of experimental designs that attempt to minimize complications from steric effects as well as from the highly compliant nature of these types of materials. In the case of the former, for example, a bead format not only may decrease contributions to steric effects on binding by providing a more flexible surface architecture, but also may decrease the buildup of any lateral stress at the microcontact formed during the experiment.[333,337,338,341] Flexible tethers and low packing densities have also proven useful.[332,342,343] In the case of the latter, studies using a range of derivatization pathways have found that excessive applied contact loads degrade the proteinaceous coating to the point where the observed force curves are unreliable.[332,333,344,345] We note that improvements in instrumentation have also been reported that provide a higher level of control over the tip−sample separation distance during the approach portion of the force curve as well as the tip−sample contact time.[345] Although difficult to invoke as an all-encompassing guideline, contact loads greater than a few nanonewtons generally appear to be problematic with these types of systems.

An intriguing approach to determining intermolecular forces was demonstrated through the use of a "magnetic jump method".[346] A biotinylated glass surface was incubated with paramagnetic beads coated with streptavidin. A tip modified with a small magnet was advanced toward the surface until rupture of the biotin−streptavidin bond caused the bead to jump from the surface to the tip. The deflection of the cantilever at the jump point is a measure of the interaction strength of the biotin−streptavidin bond. Preliminary measurements using this technique showed a range of binding forces (0.3−3 nN), with the apparent quantization at 0.8 and 1.6 nN possibly corresponding to one and two noncovalent bonds, respectively. The forces applied using this approach were substantially less than those attainable using most commercially available instrumentation. In addition, work involving the use of magnetically coated cantilevers is underway to improve the force sensitivity of SFM.[347] Indeed, these types of methods will likely become part of the growing arsenal of SFM techniques.

Several studies have simulated biotin−streptavidin binding.[334,335] An extended molecular dynamics simulation of the force required to rupture the biotin−streptavidin complex was in good agreement with SFM-determined forces for a range of retraction velocities. Furthermore, the favorable agreement also supported a proposed multiple-pathway mechanism involving five major unbinding steps.[335] Biotin−streptavidin rupture was also examined through an adiabatic mapping technique, which revealed the role of hydrogen bonding in specific binding.[334]

The potential extension of SFM-based force measurements to industrially significant immunoassay systems is of vast technological importance. In a study of the polystyrene microtiter wells commonly employed in the enzyme-linked immunosorbent assay (ELISA) method,[340] adhesive forces of 0.410 ± 0.166 nN were observed between a biotinylated tip and a streptavidin-coated well, with no visible interaction after the well was filled with biotin. These results demonstrated the ability of SFM to measure interactions of biomolecules involved in immunoassay systems used worldwide.

2. Antigen–Antibody Interactions

The determination of antigen−antibody interactions has proven more challenging than that for the biotin−avidin family. This difficulty arises from a combination of several factors, including a lower mechanical strength, an increased heterogeneity, and the lower binding affinities of antigen−antibody systems as well as a greater binding sensitivity to steric effects.[343] These characterizations can prove particularly challenging because the compliant nature of these systems can cause the tip to roll and/or buckle during retraction, giving a false rupture indication.[348]

As previously discussed, steric issues have been addressed by increasing the tether length[342,343] and by limiting the packing density of the immobilized material.[342] In an investigation of the binding interactions between human serum albumin (HSA) and polyclonal anti-HSA, both design concepts were employed.[342] First, a coupling agent was affixed to the end of a flexible, 6-nm poly(ethylene glycol) spacer previously immobilized on a tip. Second, HSA was coupled to the spacer at a packing density that statistically limited the interaction between the tip and sample to one interaction within the tip−sample microcontact. With this approach, the detected average adhesion force for 1:1 specific binding between HSA and anti-HSA was 0.244 ± 0.022 nN, which was attributed to individual binding events between the Fab portions of the antibody and HSA. This investigation also demonstrated that the location of antigenic sites on the surface can be determined with a positional accuracy of 1.5 nm by scanning the tip laterally while collecting force scans, an exciting step toward high-resolution mapping of the recognition sites of such materials. Force mapping in biological systems will be discussed in more detail shortly.

A spacer arm was also utilized to couple biotin to bovine serum albumin to form an artificial antigen (BBSA) for probing adhesion forces with polyclonal goat anti-biotin antibodies.[343] An overall binding force of 0.112 nN was determined. However, a histogram summarizing the retraction portion of the force curves suggested that the microcontact ruptured in quantized steps, each of ∼0.060 nN. Though more speculative, an estimate of contact area argued that each rupture corresponded to the breakage of more than 1 but less than 10 interactions.

Quantized adhesion forces of $\sim 0.050 \pm 0.010$ nN were also detected in a SFM investigation of ferritin/anti-ferritin binding.[349] Even though an immunoassay system employing the capture of serum ferritin by anti-ferritin-coated microtiter wells has been developed, little is known about how the ferritin molecules are bound to the antibodies. Therefore, in instances where structural or thermodynamic data may be limited, a direct measure of the strength of the antigen−antibody bond by SFM can give glimpses into the binding process.

3. Other Protein Interactions

The measurement of adhesion forces in other protein systems has also been examined. This type of SFM analysis has been applied to examine an important aspect in immunoassays and other vital areas in the life sciences, that of protein adsorption. Chen et al. used a bovine serum albumin (BSA) coated tip and several model molecular surfaces comprised of NH_2, COOH, and CH_3 end groups to explore the dependence of protein affinity on the identity of the terminal group.[350] The hydrophobic methyl surface exhibited the highest affinity to BSA and was independent of pH; the other surfaces displayed strong pH-dependent interactions, where the contacts having dissimilar ionic charges possessed the higher affinities (see Figure 25). This study suggests the possible use of SFM in studies that systematically examine issues central to protein adhesion.

Another example used SFM to unravel issues related to the function of cell adhesion proteoglycans (APs),[351] which mediate cell recognition and aggregation through intercellular carbohydrate interactions. The structure of APs is annular in nature, consisting of rings that are about 200 nm in diameter surrounded by ∼20 polysaccharide arms which are 180 nm in length. By conducting force curve experiments at the microcontacts formed by tips and surfaces both modified with APs, the long speculated importance of the polysaccharide arms to cell aggregation was experimentally confirmed for the first time. The force curves also revealed the presence of long-range contacts between the tip and sample and the regulation of these interactions by Ca^{2+}. The former reflects an untangling of the polysaccharide arms, whereas the latter demonstrates the regulation of the interactions between arms by Ca^{2+} complexation. These findings, supported by a decrease in the observed frequency of ruptures when the carbohydrate epitopes were blocked by addition of a monoclonal antibody, strongly support the role of the cohesive interactions between the polysaccharide arms in cellular aggregation.

The interaction forces between the *E. coli* chaperonin protein GroEL and two different substrate proteins were probed by SFM in an investigation of the regulatory effects of ATP on protein adhesion.[352] As expected, the interaction forces between GroEL and each of the substrate proteins decreased upon addition of ATP. However, the adhesion force was surprisingly smaller for the native substrate proteins in comparison to denatured substrate proteins. This finding may prove of value in furthering insight into the denaturization process.

A novel approach for conducting truly "single-molecule" rupture studies of actin-heavy meromyosin (HMM) has been recently demonstrated.[353] An epifluorescence microscope integrated to a custom-built scanning force microscope was used to visualize the derivatization of the tip with a single fluorescently labeled HMM molecule. The pull-off force measured from an actin surface with the HMM-linked tip was found to be 10 times lower and rupture lengths 10 times longer than expected on the basis of other known interprotein forces. It was postulated that these results may be due to the flexible loop structure of the actin−myosin interface.

In addition to exploring issues related to interaction forces, SFM has been applied to detail the mechanical properties of protein structure by stretching molecules bound between a tip and substrate.[354−356] Using α_2-macroglobulin protein derivatized with sulfhydryl groups for immobilization on gold-coated mica and a gold-coated tip, the confined protein was mechanically stretched during a retraction cycle.[356] The force required to free the tip from the surface ranged from 0.25 to 1.8 nN and was attributed to the rupturing of noncovalent subunit interactions, while an isolated case at a higher force (2.5 nN) was assigned to cleavage of the Au−S bond. Proteins, in

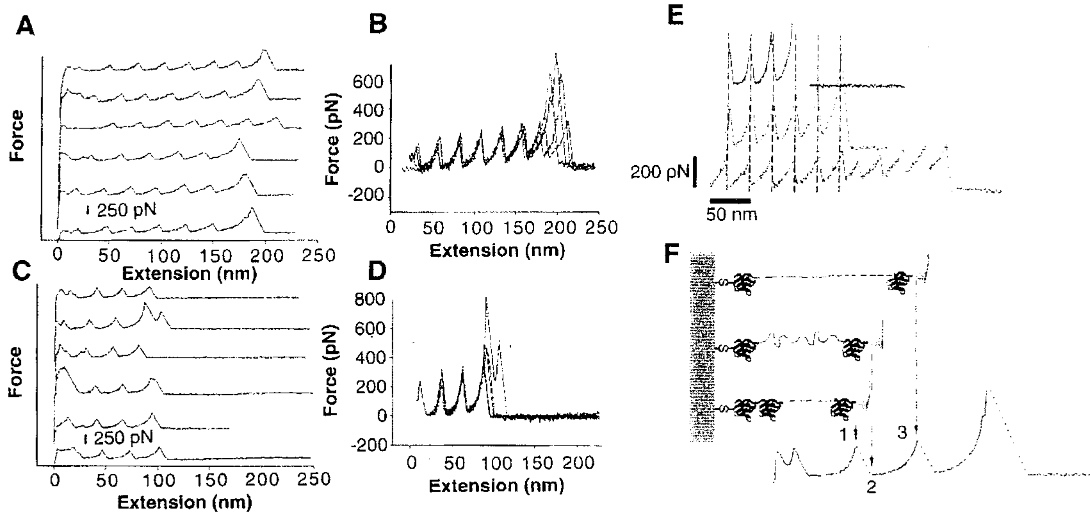

Figure 29. Stretching well-defined recombinant titin segments produces force extension curves that are consistent with the unfolding of individual Ig domains. (A) Stretching Ig8 domains produced force extension curves that contained up to eight equally spaced peaks of ascending force ranging from 0.15 nN to a maximum of 0.30 nN. (B) Force extension curves obtained from Ig8 proteins were superimposable and revealed spacing between the force peaks of 25 nm. (C) Stretching of shorter Ig4 segments produced force extension curves with a sawtooth pattern of up to four peaks. (D) Force extension curves obtained with Ig4 were also superimposable and revealed 25 nm spacings between force peaks. (E) Force extension curves obtained from all three titin forms (from top to bottom: Ig4, Ig8, and native); note the curves were superimposable. (F) A possible sequence of events for the unfolding of Ig domains; details of this mechanism are given in ref 355. Reprinted with permission from ref 355. Copyright 1997 American Association for the Advancement of Science.

some instances, could be stretched up to 400 nm before fully breaking contact, suggesting issues related to protein folding may be tractable with this methodology.

Polymeric and protein dynamics have also been examined by capturing single strands of dextran[354] or titin, the sarcomeric protein found in striated muscle,[355] between a tip and surface. The characterization of dextran yielded mechanical parameters such as segment elasticity and the Kuhn length from elongation curves (i.e., plots of force vs extension length). The extension plots for titin[355] exhibited the sawtooth patterns presented in Figure 29. The peaks in the extension plots for the native protein showed a periodicity of ∼25 nm and a restoring force of 0.150−0.300 nN. This periodicity is in good agreement with the expected length required to unfold individual Ig domains. To test this hypothesis, recombinant Ig4 and Ig8 fragments were constructed. Eight peaks were observed in the elongation plots for Ig8 and four with Ig4 as shown Figure 29. This quantization is further evidence for the sequential unfolding of individual Ig domains, demonstrating the ability of SFM to probe mechanical properties at the level of single tertiary structures.

4. DNA Interactions

The ability of SFM to characterize binding interactions has also captured the interest of those in the area of genetics. Lee and co-workers were the first to report the measurement of single molecular forces between complementary DNA molecules.[331] By attaching complementary 20 base pair oligomers of DNA to tip and silicon surfaces composed of sequences that limit pairing to every four base pairs, the results in Figure 30 were obtained. A representative force curve obtained for this system is shown in part A, with a, b, and c corresponding to the jump-to-contact, repulsive force, and jump-from-contact (i.e., the adhesion) portions of the curve, respectively. Four distinct force regimes for the jump-from-contact event were observed as shown in the histogram in part B: 0.480 (nc), 0.830 (a), 1.110 (b), and 1.520 nN (c). The lowest range (nc) was assigned to nonspecific interactions, whereas the remaining three in ascending order were attributed to interactions between 12, 16, and 20 base pairs, respectively. These data suggest that the magnitude of the interactions between the 4 and 8 base pair complements was below that of the nonspecific interactions.

A similar study using thiol-modified DNA 14-mers covalently bound to gold-coated tips and surfaces measured an average adhesion force of 0.46 ± 0.18 nN for complementary strands versus 0.10 ± 0.07 nN for noncomplementary strands.[357] Use of a mixed monolayer prepared from the thiol-modified DNA and an alcohol-modified thiol provided a balance between the surface density of the DNA strands and an effective free volume between the strands upon contact. Elongation forces were also detected when double-stranded DNA was stretched and the tension was observed as a function of tip−sample separation distance.

Rupture forces between complementary single strands of DNA were also found to be dependent on the tip−sample contact time.[337] Using a biotin-functionalized oligomer consisting of 21 thymidine residues immobilized on an avidin-coated tip, the extent of interaction with polyadenine (specific) and polycytosine (nonspecific) agarose beads was examined. At the polyadenine beads, the adhesion force reached a maximum of 4 nN after a contact time of 2 min. The adhesion force at the polycytosine beads, however, achieved a maximum of only 1.5 nN after a contact time of 5 min. Thus, observations of the evolution of the adhesion force as a function of contact

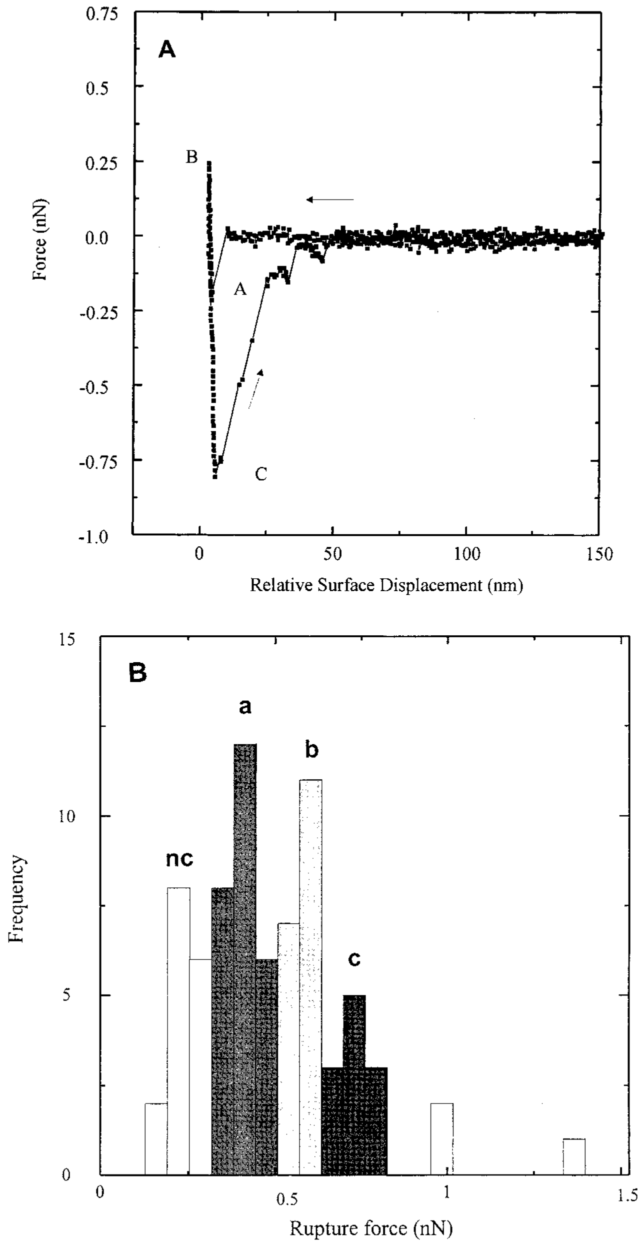

Figure 30. (A) Force−distance curves measured between $(ACTG)_5$ and $(CAGT)_5$ functionalized tips and surfaces. Points a, b, and c indicate the jump-into-contact, a region of repulsive force, and the jump-from-contact, respectively. (B) Histogram of rupture forces measured for a single pair of surfaces over a 2 h period. The distribution of rupture forces labeled nc is attributed to nonspecific surface forces. The distributions of rupture forces labeled a, b, and c are attributed to a single pair of oligonucleotides involving 12, 16, and 20 base pairs, respectively. Adhesive forces greater than 2 nN are assigned to multiple molecular interactions, and the different shadings correspond to the different groupings. Reprinted with permission from ref 331. Copyright 1994 American Association for the Advancement of Science.

time may provide a basis for assessing the dynamics of strand reorientation and alignment.

The presence of significant attractive forces measured between complementary purine- and pyrimidine-modified surfaces and tips has been exploited for recognition-based SFM imaging.[358] Molecular periodicity was observed on a thymine-coated surface while topographically imaging with an adenine-coated tip. It was postulated that this recognition capability, presumably caused by intermolecular hydrogen bonds, could be utilized as a component for the SFM-based sequencing of DNA. Together, these studies demonstrate the ability of SFM to open new avenues for exploring problems in genome research.

It is apparent from the breadth of the discussion on the biological systems studied to date by SFM-based force measurements that important, new insights can be gained into the processes that control biological recognition. Further optimization of instrumental parameters, along with improved methods of controlling biological immobilization, will clearly advance our understanding of key biological functions.

5. Force Mapping of Biological Systems

In parallel with the discussed developments of force mapping techniques in the area of chemical analysis, the determination of adhesion properties of biological systems has also been extended to the mapping of surfaces. Force mapping of these systems opens up the exciting possibility of, for example, linking the structural components of living cells to their role in biological function.

Building on a preliminary concept investigation,[259] Radmacher and co-workers mapped the adhesion forces of isolated and aggregated lysozymes dispersed across a mica surface.[267] Lysozyme is an enzyme abundant in the body whose function involves the breakdown of bacterial cell walls. Surfaces were scanned laterally while force curves were collected. From the collected force curves, maps of the point-of-contact (related to topography), adhesion force, and retraction velocity (related to viscosity) were generated using an offline analysis program and displayed by imaging software. Individual lysozymes could be detected in the adhesion image, with the resolution estimated at ∼15 nm. The adhesion force detected on the lysozyme was lower than on the mica; the retraction velocity on the lysozyme was also lower, indicating a higher viscosity. These conclusions were reached by comparisons with the point-of-contact maps. From plots of indentation versus load, the Young's modulus of a lysozyme was determined to be 0.5 ± 0.2 GPa; this value was used to calculate the contact area and then the intrinsic viscosity (800 ± 400 Pa s) of the biomaterial. This work demonstrated the ability to nondestructively extract information on the viscoelastic properties of compliant biological materials using the force mapping technique.

This effort was followed up by an in vivo investigation of the elastic modulus of human platelets.[268] Platelets play an important role in blood clotting, and elasticity may be an important part of the response mechanism. During activation, a substantial reorganization of the cytoskeletal elements and receptors of a platelet occurs. Maps of surface topography and elastic modulus were simultaneously produced for individual cells, with a resolution of ∼100 nm for the elastic modulus images. The images showed a strong correlation between the height of the cell and the elastic modulus. The elastic modulus ranged from

~1.5 kPa in the high central pseudonucleus of the cell to ~50 kPa in the lower outside cortex region. It was necessary to control carefully the loading forces exerted on the cell during the force curve measurements to avoid artifacts in the elastic modulus images. Too high of a loading force excessively compressed the cell, and the measured elastic modulus was that of the substrate.

Laney and co-workers used force mapping to examine changes in the elasticity of cholinergic synaptic vesicles in different buffers.[359] These vesicles release the neurotransmitter acetylcholine into the synaptic cleft that triggers an action potential in the postsynaptic cell. Importantly, advances in our understanding of this system may aid in devising solutions for larger problems in human health, such as Alzheimer's disease, which involves loss of cholinergic synapses. The results revealed that the centers of the vesicles were generally harder than the edges, suggesting the presence of internal structure. The centers of vesicles in calcium buffer were found to have a significantly larger mean elastic modulus than the centers of vesicles exposed to hypoosmotic buffer. Centers of vesicles exposed to isoosmotic buffer had intermediate elastic moduli. The higher elastic modulus in calcium buffer apparently results from the uptake of calcium in the internal structure of the vesicle, which may minimize cytoplasmic Ca^{2+} concentrations. These experiments also advanced several aspects of instrument control and data manipulation, including an improved feedback mechanism that maintains a constant cantilever deflection to compensate for any thermal drift between force curves, and software that plots the force at any point on a force curve.

Several research groups have used force mapping to characterize the distribution of interactions between a tip and a sample by immobilizing a ligand on a tip to image surface receptors.[269−272,342] This type of mapping is an extension of the measurement of ligand−receptor binding forces, as discussed earlier, to two dimensions.

Gaub and co-workers have used SFM to map the distribution of binding partners on a surface using so-called "affinity imaging".[270] In affinity imaging, topography, adhesion, and sample elasticity are simultaneously determined as in force mapping, but the tip is modified to have a specific affinity for a binding partner affixed to the surface. Thus, the specific interactions that occur between binding partners on the tip and surface will be manifested as an enhanced adhesion, allowing one to map the distribution of surface receptor sites. The potential of the affinity imaging technique was investigated by employing the well-studied biotin−streptavidin system. Figure 31 shows affinity images of a patterned streptavidin/gold surface imaged with a biotinylated tip. Force−distance curves were analyzed online to speed the imaging process. Typical acquisition times were ~17 min for a 128 × 128 pixel image. The topographic images in parts a and c of Figure 31 show elevated square regions, assigned to the deposited gold layer. The streptavidin regions correspond to the lower regions of the image. The adhesion image in part b of Figure 31 indicates that there is an increase in adhesion in the grid regions versus the square regions because of specific interactions between the streptavidin regions and the biotinylated tip. Parts c and d of Figure 31 are topography and adhesion images, respectively, after addition of an excess of biotin to the surface, which effectively blocks the streptavidin sites from binding to the tip; the lack of a detectable contrast in the adhesion image verifies the specificity of affinity imaging.

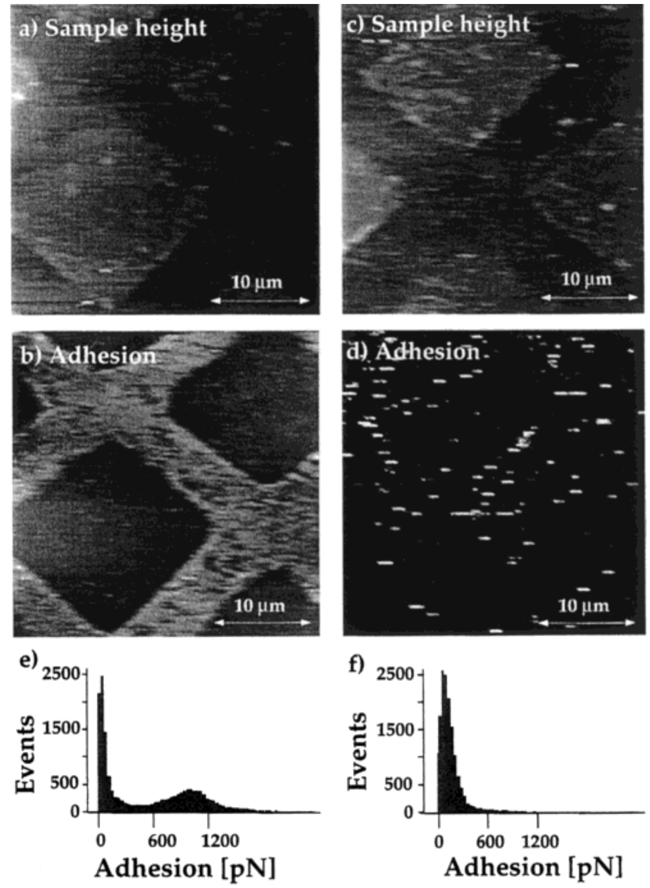

Figure 31. Affinity images of a streptavidin (grids)/gold (squares) pattern obtained with a biotin-modified tip. Topography images (a and c) and affinity images (b and d) were obtained before and after blocking with free biotin. Adhesion histograms of images b and d are shown in panels e and f, respectively. Reprinted with permission from ref 270. Copyright 1997 The Biophysical Society.

Chen and co-workers used a protein-modified tip to visualize protein adsorption on the basis of differences in adhesion on the polystyrene surfaces commonly used in immunoassays.[272] A large adhesive force was detected between the protein-coated tip and the bare polystyrene surface, presumably due to strong hydrophobic interactions. When the surfaces were coated with protein, a large decrease in adhesion was observed because of weak nonspecific protein−protein interactions. By monitoring simultaneously topography and adhesion, force maps of partially covered substrates revealed those regions of the surface covered with protein. It was also possible to monitor the dynamics of protein adsorption through decreases in adhesion over exposure time.

Further work in this laboratory used an antigen-modified probe tip to produce force maps of an antibody-coated silicon wafer.[271] Force curves were collected every 24 nm as the surface was scanned; offline data analysis was used to plot the area under each force curve, which is a direct measure of the work of adhesion. Adhesion maps of the antibody-coated surfaces revealed areas of high adhesion, presumably due to specific biomolecular interactions between the probe and surface. Flooding the surface with excess antigen resulted in adhesion maps containing considerably fewer interactions, confirming the specificity of the imaging process. These experiments represent a significant step toward developing an analytical technique capable of mapping the functionality of sensor surfaces using discrete biomolecular recognition.

One of the first attempts at mapping single-molecule force interactions was by Schindler and coworkers.[342] Through the use of a spacer arm, it was possible to acquire force−distance curves between individual antigen−antibody complexes. Maps of the location of antigen sites were developed while scanning and recording the number of binding events measured between the antigenic surface and an antibody-modified tip. Importantly, the position of antigenic binding sites could be determined with 1.5 nm positional accuracy.

The height and adhesion of single molecules of ICAM-1, an intercellular adhesive, were mapped by Willemsen et al.[269] This experiment was performed by modifying the tip with monoclonal antibody toward ICAM-1 at concentrations statistically resulting in only a single molecule within the size of the tip−sample microcontact. The use of a long flexible spacer as a tether enhanced the probability for specific binding by reducing the steric hindrance of materials linked to surfaces. Comparison of height and adhesion images revealed that the regions of highest adhesion corresponded to those of maximum height. By analyzing the high adhesion force curves in detail, it was possible to discriminate between specific and nonspecific interactions. This ability resulted from a detectable change in the slope of the retraction portion of the force curve that arises from the stretching of the spacer affixed to the antibody; there was no detectable change in the retraction slope for nonspecific interactions. The resolution of the height and adhesion images was estimated to be 20 and 5 nm, respectively. The higher level of resolution for the adhesion measurement likely resulted from the specificity of the interaction. Using this methodology, it may eventually be possible to map the individual binding sites of such molecules, a powerful addition to techniques currently used in many areas of biotechnology.

B. DNA Analysis Using SFM

Since the early 1990s, numerous investigations have applied SFM to the analysis of DNA. This section highlights the evolution of SFM from a tool used to simply interrogate the size and shape of DNA toward its use as an analytical biochemical tool in DNA assays.

As with other biological samples, effective immobilization strategies are key. The sample must be firmly affixed to the surface to prevent its movement by the probe tip and yet not be too restrictive as to interfere with the interaction of DNA with restriction enzymes, polymerases, and other important biological species. Examples of immobilization strategies include the use of divalent metal cations to couple DNA to mica,[153−155,360] electrostatic interactions to bind the negatively charged phosphate backbone of DNA to a positively charged surface,[218] covalent coupling by employing linkers such as 1-ethyl-3-(3-dimethylaminopropyl)carbodiimide (EDC)[46] and dithiobis(succinimidylundecanoate) (DSU),[163] and direct chemisorption to gold via a 5′-thiol modification.[162,163]

Hansma and co-workers were one of the first groups to report the use of SFM to image DNA.[48] Since then, our understanding of the effects of imaging conditions on the size, shape, and motion of individual DNA molecules has significantly advanced. Factors such as humidity[361] and the concentration of divalent cations[362,363] affect the observed size and shape of DNA. Recently, phase images from TM-SFM have been used to monitor the motion of individual molecules in aqueous solution.[364]

In addition, SFM has also been used to explore the topography of DNA−enzyme complexes including the orientation of histidine-tagged DNA−RNA polymerase complexes[365] as well as the complex formed between DNA and nucleases such as a mutant form of *Eco*RI[366] and DNase 1.[367] As discussed earlier, SFM has also been used to examine rupture forces between complementary and noncomplementary strands of DNA.

Recently, Fang and co-workers proposed an analytical method for solid-state DNA sizing (SSDS) using SFM.[368] Employing sizing software developed in their laboratory, SFM-based SSDS produced results equivalent to those obtained by traditional agarose gel electrophoresis for ± screening of artificial chromosomes. Furthermore, the measured lengths of small DNA fragments were within 15% of the expected length, and the observed full width at half-maximum values extracted from a distribution of multiple determinations, used to assess the precision of SSDS, were typically <10% for fragments of <200 base pairs. Intended to provide high throughput screening of DNA for sizing applications such as fingerprinting, ± screening, and genotyping with low sample costs and rapid analysis times, SSDS may open the way for the routine analytical treatment of DNA by SFM.

Bottomley's laboratory is advancing the use of SFM from a tool used to interrogate the size[153,368] and shape[361−363] of DNA to one that can be used as an analytical device in DNA-based assays. In work that set the stage for a SFM-based DNA assay, Coury et al.[369] examined the effect of intercalator addition on DNA. First, a psorlen derivative containing a biotin moiety was intercalated into dsDNA. Streptavidin-coated 5 nm gold colloids were then added and used as a label for image contrast. This work is intriguing because it demonstrates the use of SFM to visualize DNA intercalation events that are important in the understanding and development of new and better types of DNA-targeted therapies.

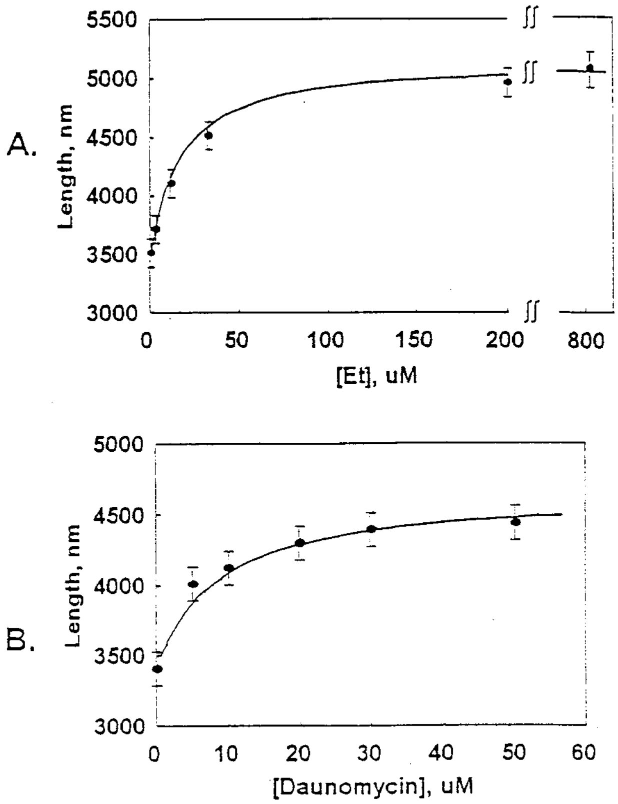

C.

Table 1. Fraction of intercalation sites occupied at varying intercalator concentrations

Intercalator	Concentration, μM	Fraction of sites occupied*
Ethidium	0	0
	0.8	0.04
	3.5	0.10
	12	0.21
	33	0.32
	200	0.45
	800	0.52
Daunomycin	0	0
	5.0	0.17
	10	0.20
	20	0.25
	30	0.28
	50	0.29

Data are based on 10,300 bp for *p*BBH b and 3.4 Å lengthening per intercalation event.
*[pBBH b] = 1.62×10^{-11} M.

Figure 32. A SFM-based assay for intercalator–DNA interactions. (A, B) DNA length versus intercalator concentration for (A) ethidium and (B) daunomycin. (C) Fraction of intercalation sites occupied at varying intercalator concentrations. Reprinted with permission from ref 370. Copyright 1996 National Academy of Sciences.

In an extension of this work, Coury et al.[370] used SFM to measure the length of a DNA–intercalator complex formed as a function of intercalator concentration. These measurements were performed without the use of colloidal labels. Figure 32 illustrates these results. Parts A and B of Figure 32 are plots of the length of double-stranded DNA (dsDNA) measured by SFM as a function of intercalator (ethidium (A) and daunomycin (B)) concentration. In both cases, the length of dsDNA increased as the intercalator concentration increased until constant values were reached, indicating the saturation of the dsDNA with intercalator. The fraction of sites occupied by the intercalator as well as the binding affinities of the intercalators to dsDNA were also determined as illustrated in Figure 32C. This work clearly demonstrates the utility of SFM as an analytical tool in DNA analysis. Results from such studies will undoubtedly provide significant, new insight into the interaction of DNA with other molecules specifically designed to bind to DNA, and may prove valuable in evaluations of the efficacy of new chemotherapeutics at the level of DNA replication.

Coury et al. also showed that SFM could be used to determine the mode of interaction between dsDNA and the drug 2,5-bis(4-amidinophenyl)furan (APF).[370] APF has shown significant activity in treating a form of pneumonia that is the leading cause of death in AIDS patients. Imaging results showed that APF interacts with DNA in a nonintercalative manner. This demonstration is important because the more traditional methods of addressing such questions (e.g., X-ray diffraction and NMR) are time-consuming and labor intensive. Knowing how ligands, such as anti-cancer drugs, interact with DNA may prove invaluable in the design of new therapies.

Perhaps the ultimate biochemical analysis that could be performed by SFM is DNA sequencing. One of the earliest efforts to visualize individual nucleotide bases with SFM was reported by Hansma et al.[371] When immobilized on a polymerized lipid, some individual nucleotide bases modified with fluorescein isothiocyanate became visible because of the resulting increase in the local topography. However, the images were of poor quality and the results somewhat speculative.

The issue of whether SFM can be used for DNA sequencing has, in fact, become an extensively debated topic. Hansma and co-workers argued in 1991 that SFM may prove faster as a sequencing method than traditional gel electrophoretic methods.[47] For example, a gel sequences up to 500 nucleotides in about a day, whereas SFM could potentially scan 400–800 nucleotides in a 40 nm × 40 nm scan area in 10 s.

In an authoritative analysis of this topic, Pope et al. argued that the structure of dsDNA itself poses an inherent problem in sequencing by SFM.[372] The individual base pairs, residing in the interior of the molecule, are inaccessible to the probe tip; only the phosphate backbone exterior, common to all dsDNA molecules, is accessible. On the other hand, the structure of single-stranded DNA (ssDNA) is more amenable to SFM interrogation. However, the tendency of ssDNA to form complex structures with itself via intrastrand hydrogen bonding often precludes routine access of the tip to the nucleotide bases. This complication, along with the need for improvements in sample preparation and other issues, led Pope et al. to conclude that DNA sequencing by SFM "...will be impossible".[372]

Two new operating modes of SFM, however, have recently been introduced which may advance sequencing efforts. Han and co-workers reported the use of cryo-SFM where imaging is performed under liquid nitrogen vapor.[373] When operated at these reduced temperatures, imaging resolution is greatly

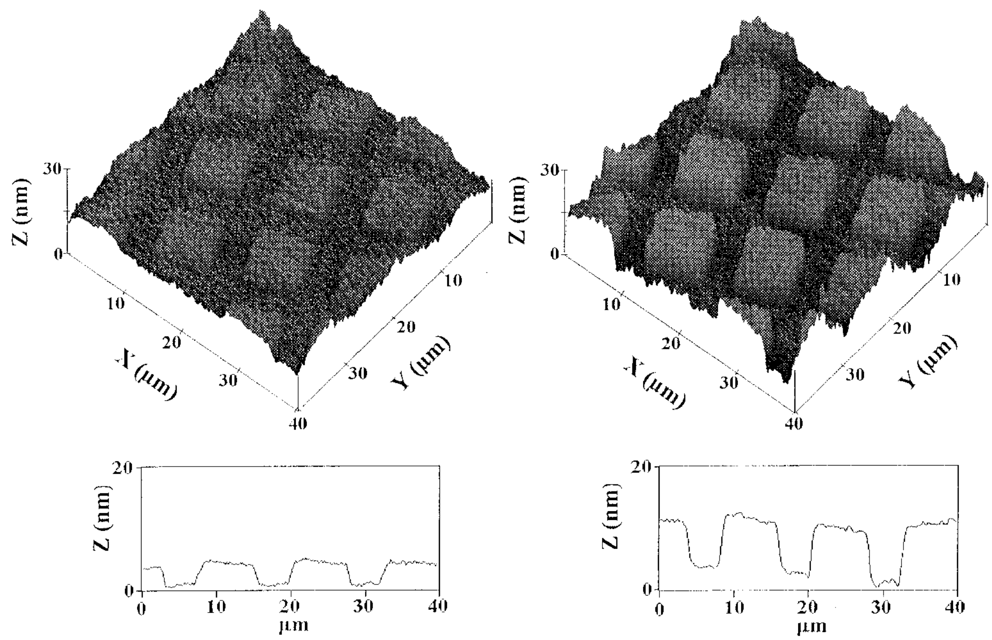

Figure 33. An immunoassay based on SFM-observed height changes using an uncoated Si_3N_4 tip. SFM height images (40 μm × 40 μm) of a rabbit IgG array in (left) 50 mM PBS and 1% (v/v) Tween 80 and in (right) binding buffer with 0.1 mg/mL goat anti-rabbit IgG and 1% (v/v) Tween 80. The cross-sectional analysis was performed by averaging the individual line scans contained in the area of a single row of the array. The images were obtained at an F_N of ~2 nN and a scan rate of ~6 Hz. Reprinted with permission from ref 152. Copyright 1998 American Chemical Society.

enhanced.[374] Indeed, the width of DNA, which is typically reported to be 6−10 nm when imaged at room temperature,[372] is less than 3 nm when imaged using cryo-SFM. Furthermore, thermally excited movements of the sample are reduced, thereby minimizing any tip-induced damage to the sample.

Another exciting development toward DNA sequencing is hydration scanning tunneling microscopy (HSTM). With HSTM, biological molecules are imaged on insulating substrate surfaces under high humidity conditions and low tunneling currents. Because STM is inherently a higher resolution measurement and a noncontact measurement, high-resolution images can be obtained while tip-induced sample damage is avoided. In this mode, Heim and co-workers imaged plasmid DNA with 3 nm resolution.[375] Improvements in this technique will have a profound impact in this area.

C. Assays Using SFM

The high spatial resolution of SFM, which is capable of detecting individual antigen−antibody binding events through the measurement of height[376] or rupture forces,[342] has implications for use in conducting highly sensitive immunoassays. Through the parallel processing of reactants confined to micrometer-sized addresses, SFM-based assays provide the possibility of reducing sample volume, cost, and analysis time.

The concept of an immunoassay based on probe microscopy was first proposed by Sorin et al. in the early 1990s, using STM to image gold colloids bound to immune complexes formed on conductive substrates.[377] It was a few years, however, before the tenets of the concept were adapted for use with the many imaging modalities of SFM.

An immunoassay based on the measured distribution of heights of individual human serum albumin (HSA) molecules, anti-HSA antibodies, and specific antigen−antibody complexes adsorbed on mica was examined.[376] Since the antigen (0.62 nm), antibody (1.91 nm), and immunocomplex (3.03 nm) differed in measured heights by a sufficient amount, histograms of measured heights were able to detect the formation of specific immunocomplexes, with an estimated detection limit of 50 binding events/μm^2. Although only preliminary, the ability of SFM to study interactions between single molecules was demonstrated.

Another study utilized SFM to probe a surface consisting of streptavidin bound to a photolithographically patterned array of biotin for use as a possible method to define spatially receptor sites for the observation of ligand−receptor force interactions.[378] A height of ~4 nm was observed for the streptavidin-modified areas over the base substrate, whereas the underlying biotin layer was only ~0.8 nm in height.

Our group has recently demonstrated the ability of SFM to conduct height-based immunoassays in situ and in real-time using compositionally patterned antigen arrays.[152] Substrates composed of micrometer-sized square regions of antigen addresses were prepared by reacting rabbit IgG to a gold-bound coupling agent. These antigen-modified addresses were separated by grid regions that were composed of a hydrophobic octadecanethiolate monolayer. The addition of Tween 80 surfactant to the buffer solution upon the addition of goat anti-rabbit IgG antibody resulted in the absence of nonspecific protein adsorption to the grid regions. This absence allowed the grid regions to function as an internal reference plane for the increase in height observed upon antigen−antibody binding in buffer solution, as shown in Figure 33. An approximate doubling in height of the

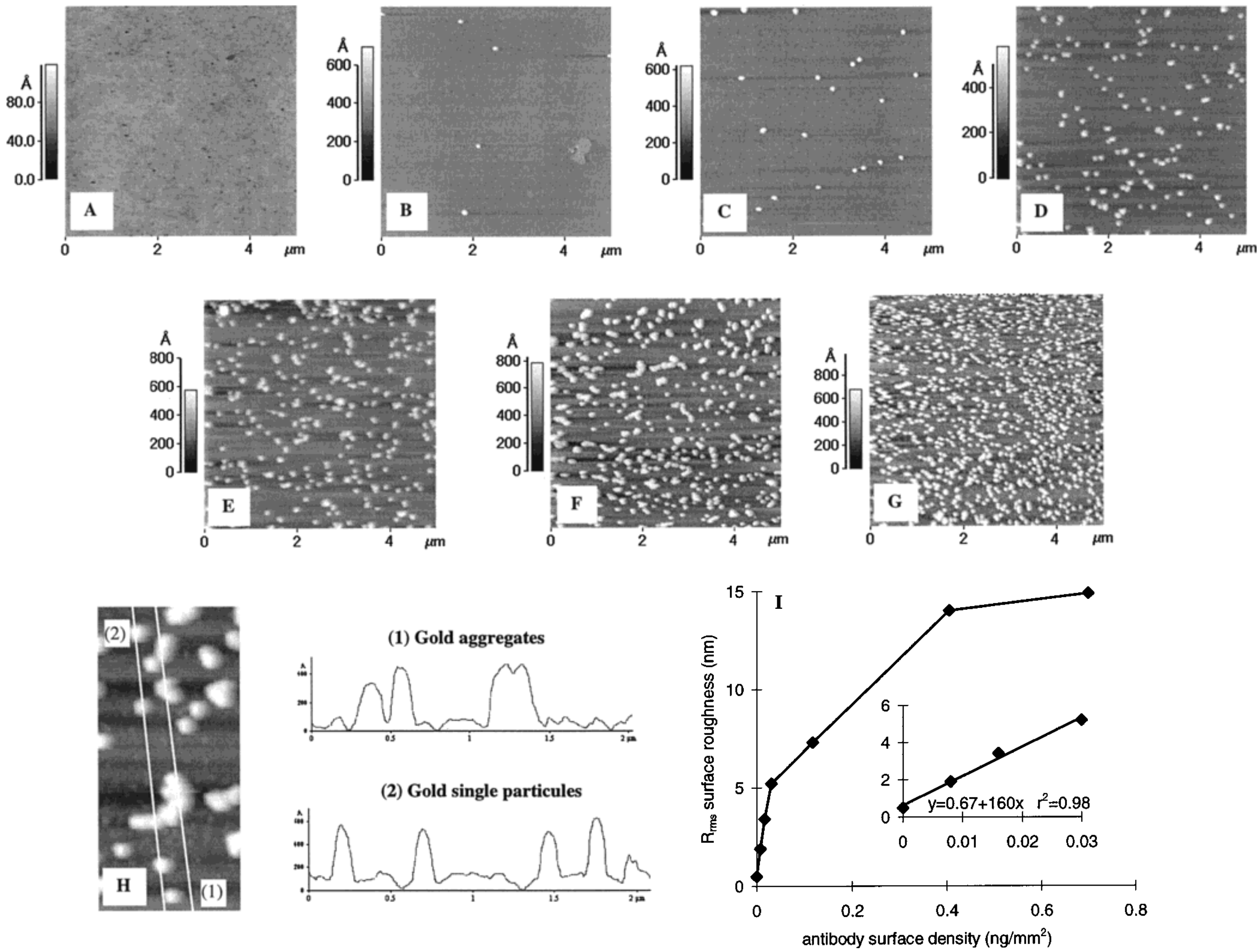

Figure 34. (A−H) Detection of immobilized anti-ferritin antibodies using gold-labeled conjugates by imaging with tapping mode SFM in air. The antibody densities are (A) 0, (B) 0.008, (C) 0.015, (D) 0.030, (E) 0.117, (F) 0.404, and (G) 0.700 ng/mm^2. (H) Zoom-in on part F showing the cross-section of individual gold particles and of gold aggregates. (I) Calibration curve for the SFM detection of adsorbed capture antibodies after binding with gold-labeled colloidal conjugates. Variations of surface roughness as a function of antibody surface density were measured. The inset shows a lower antibody surface density range. Reprinted with permission from ref 30. Copyright 1997 American Chemical Society.

antigen-modified regions from ∼4 nm (left) to ∼8 nm (right) occurred upon addition of antibody, consistent with the formation of a single antigen−antibody layer. Addition of a nonspecific antibody (e.g., goat anti-bovine IgG) to the antigen arrays did not result in a subsequent height increase. Real-time monitoring revealed that the increase in height was complete in ∼5 min, consistent with earlier antigen−antibody binding studies.[379]

The ability of SFM to quantitatively detect specific antigen−antibody binding has also been demonstrated through the use of gold-labeled antibodies.[30,380] Initial work[30] measured the increase in surface roughness resulting from the binding of 40 nm colloidal gold conjugated with antibody to the surface bound antigen. Images obtained from surfaces of increasing antigen surface density exposed to gold-labeled antibodies are shown in Figure 34A−H. A correlation was found between the antigen surface density and the SFM-measured surface roughness following gold-labeled antibody binding, as evidenced in the calibration curve shown in Figure 34I. This methodology was found to be 40 times more sensitive than radioimmunoassay (RIA) or ELISA methods conducted on similar surfaces. By observing the changes in surface roughness on anti-ferritin antibody surfaces upon binding of ferritin, a relatively large antigen (MW 500 000), it was possible to determine antigen concentration in solution directly without the use of labels, although this method was less sensitive than RIA or ELISA. Recent work has focused on using gold-labeled antibodies to detect antigen in solution using a sandwich assay format, and directly counting the number of bound gold particles.[380] The number of gold particles observed correlated well with the concentration of antigen in solution. By adding a preconcentration step, a concentration as low as 0.015 ng/mL could be detected, which is comparable to that of most standard assays.

Enzyme activity has been assayed in situ using SFM.[381] Using TM-SFM, height fluctuations of ∼1 nm that lasted for ∼50 ms were observed on the top of lysozyme protein layers in the presence of a substrate. These transients were interpreted as conformational changes of the lysozyme during the hydrolysis of a substrate. Under all other conditions, including the presence of substrate with an inhibitor, fluctuations in height were not observed. To verify that the cantilever could reliably detect the proposed small conformational changes, an estimation of the energy required to bend the cantilever by 1 nm was performed. The enthalpy of hydrolysis for the substrate was found to supply ample energy to move the cantilever 1 nm, substantiating the role of the enzymatic reaction in the SFM-observed height fluctuations.

Another form of probe microscopy, scanning electrochemical microscopy (SECM), has also been exploited for use in immunoassays. In SECM, the probe tip functions as a microelectrode, sensing local electrochemical phenomena. SECM has been used to visualize immobilized antigens[382] and enzymes[383,384] on surfaces. Furthermore, single molecules have been detected using SECM.[385] A sandwich immunoassay for the presence of carcinoembryonic antigen (CEA) on a glass substrate has been carried out using SECM.[386] The glass substrate was modified by a layer of anti-CEA, followed by the deposition of microspots of CEA solution. The spotted surface was then exposed to a solution containing anti-CEA labeled with horseradish peroxidase (HRP). The HRP catalyzed the oxidation of the reduced form of an electron-transfer mediator, ferrocenylmethanol (FMA), by H_2O_2. The reduction current of enzymatically produced FMA^+ was detected at the SECM tip, "visualizing" the immobilized CEA antigen. A correlation was observed between the reduction current and the concentration of CEA, with as little as 10 000 CEA molecules detected in a 40 μm spot.

Recent work has extended this method to a dual immunoassay format for the detection of human chorionic gonadotropin (HCG) and human placental lactogen (HPL), both of which are polypeptide hormones diagnostic of pregnancy.[387] Anti-HCG and anti-HPL were microspotted next to each other on a glass substrate, followed by exposure to HCG and/or HPL. Exposure of the microspots to HRP-labeled anti-HCG and anti-HPL with FMA and H_2O_2 allowed visualization of the immobilized antigens, as shown in Figure 35.

SECM has also been used to measure the membrane permeability of a living animal cell.[388] The SECM tip was scanned across the cell exterior at a fixed potential to reduce oxygen. Since oxygen is necessary for cell respiration, the amount of oxygen reduction current decreases when imaging is done in close proximity to a living cell due to the local depletion of oxygen. Upon exposure to KCN, the reduction current increased with time when scanning was done over a live cell, indicating a decrease in oxygen consumption. Cyanide ion is known to bind strongly to cytochrome oxidase, thus blocking electron transport in respiration and causing fatal damage to the cell. From the time-dependent changes in reduction current, the membrane permeability to CN^- was estimated at 10^{-7} cm/s.

In summary, the many favorable attributes of SFM make it an attractive technique to study biochemical phenomena on length scales unattainable by most methods. The potential gains toward a greater understanding of biological structure and function using

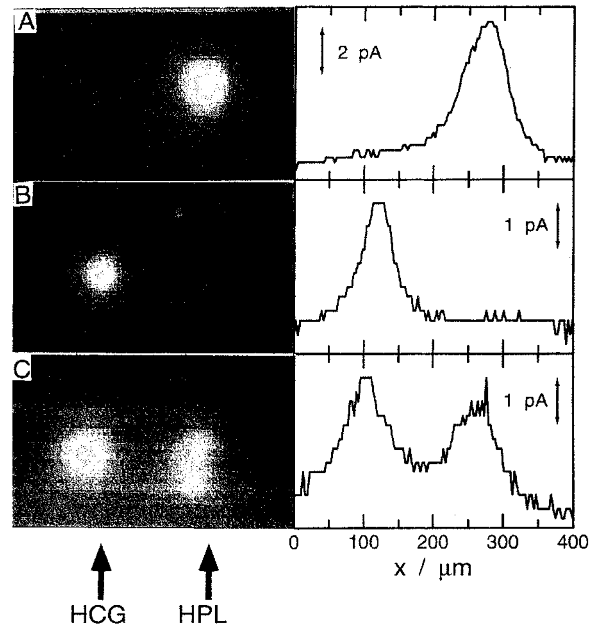

Figure 35. SECM images of substrates microspotted with anti-HCG (left) and anti-HPL (right) in 1.0 mM FMA + 0.5 mM H_2O_2 + 0.1 M KCl + 0.1 M phosphate buffer solutions (pH 7.0) and their cross-sectional current profiles. (A) Treated with HPL. (B) treated with HCG. (C) treated with a mixture of HPL and HCG. Potential 0.05 V vs Ag/AgCl. Reprinted with permission from ref 387. Copyright 1997 Elsevier Science.

SFM are clear. The continued improvement in instrument performance and scan speed, and the integration of tip arrays as discussed in the following section, should enable SFM to become a larger player in the field of biotechnology.

V. What Is Next?

As is evident, SFM has opened in-roads to explore a wide range of critical and previously inaccessible issues in the physical and life sciences. What then are the next instrumentation advances that will enhance the performance of the technique and drive new technologies and research opportunities? In completing our review, these advances are briefly examined in this section within the context of using SFM as a tool for analysis, and include issues related to resolution, sampling speed, throughput, sampling area, and detection sensitivity and specificity.

A. Resolution

Although commercially available tips can be consistently prepared from hard materials such as Si or Si_3N_4 with a radius of curvature on the order of 30–50 nm, the tip shape and contact area remain problematic, for example, when scanning features with high aspect ratios or when attempting to detect single-molecule interactions. In an emerging development aimed at reducing such problems, Dai and coworkers have attached multiwalled carbon nanotubes (MWNT) onto the end of Si_3N_4 tips.[389] Carbon nanotubes are tubular fullerenes that are macroscopically long in one dimension but are intrinsically nanoscopic and highly ordered in the other two dimensions. Figure 36 presents SEM images of a MWNT tip that

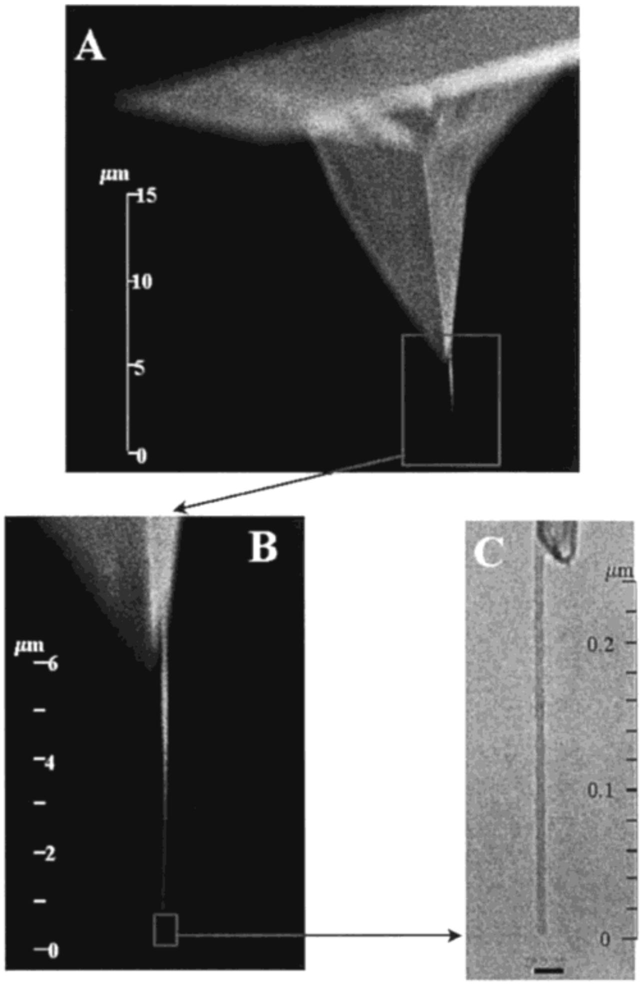

Figure 36. (A, B) Scanning electron micrographs of a multiwalled carbon nanotube bundle attached to the end of a pyramidal Si_3N_4 tip. (C) Transmission electron micrograph of the same tip. Reprinted with permission from ref 389. Copyright 1996 Macmillan Publishers Ltd.

is 250 nm in length but only 5 nm in diameter. The high aspect ratio (50) and small radius of curvature (∼9 nm) of these tips have clear advantages when features that undergo rapid changes in topography are imaged. In addition, nanotubes elastically buckle above a critical force (e.g., ∼5 nN for the MWNT similar to the one shown in Figure 36). This buckling limits the maximum force that can be applied at the microcontact as well as reduces the likelihood of damage from "crashing" the tip into the sample.

Single-walled nanotubes (SWNT) have also recently been attached to tips, resulting in an estimated tip radius of only 3 nm.[390] This decrease in the tip–sample microcontact has reduced the lateral resolution in TM-SFM from 15 nm using conventional tips[71] to 3 nm.[390] These developments, coupled with strategies for the chemical modification of such materials,[212,391,392] represent an important step toward enhancing resolution, imaging contrast, and the ability to image compliant materials nondestructively. Existing approaches to the fabrication of this type of tip are, however, very labor intensive, and the development of more effective preparative procedures are needed before their use becomes commonplace. In a very recent development, Lieber and co-workers report the development of a technique for growing individual carbon nanotubes at the end of a silicon tip.[393] This approach is more amenable to large-scale fabrication, possibly leading to wider use of such tips.

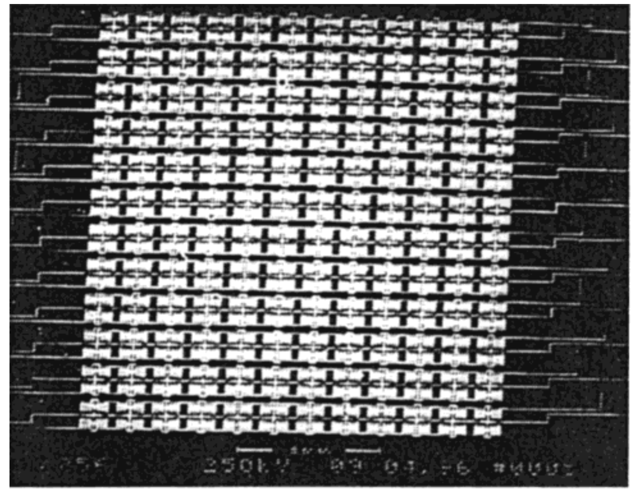

Figure 37. A microfabricated array of 144 SFM tips. Reprinted from ref 62 with permission of N. MacDonald, Cornell University.

B. Throughput

Several strategies are currently being explored to increase the analysis speed and sample throughput of SFM. While an exact evaluation must consider issues such as resolution and sample topography, a rough generalization indicates that commercially available instrumentation can presently image an area in excess of 0.01 mm^2 in about 5 min. Approaches to reduce acquisition times that utilize existing hardware have been discussed briefly earlier in this review. However, to make significant in-roads in this area, alternative concepts must be devised and implemented. To this end, efforts are underway that employ tip arrays and high-speed scanning mechanisms to image larger areas at higher scan rates.[394−397]

In one recent example, the Quate laboratory is addressing throughput via an automated cantilever array that allows high-speed, constant-force imaging.[398] This group has designed an array of 50 cantilevers that increases sample throughput by more than 2 orders of magnitude. In addition, this concept has also been used to increase the accessible scan area,[399] with the record now standing at 4 mm^2. The potential capability for high-throughput microfabrication, which has strong relevance to the fabrication of biochip arrays, was also demonstrated by using four of the cantilevers in a 50 element array. The largest tip array constructed to date has 144 cantilevers, and was fabricated by MacDonald and co-workers.[62] An example of this array is shown in Figure 37, and is only a glimpse of things to come.

C. Specificity

One of the greatest limitations to the use of SFM in chemical analysis is its lack of chemical content. Although significant headway has been realized in the past few years through concepts based on adhesion and friction, the chemical information obtained is deduced indirectly from these types of characterizations. A recent report by Rugar and co-workers, which describes the merger of SFM and NMR, may dramatically change this situation. NMR is one of the most powerful and widely used analytical techniques today. Rugar and co-workers showed that this merger has the capability to detect $\sim 10^{13}$ protons in a sample of ammonium nitrate that was mounted on an ultrathin Si_3N_4 cantilever.[400] This cantilever has a spring constant of 10^{-3} N/m, $\sim$1/30 that of typical cantilevers. Such a cantilever is capable of detecting forces of less than 10^{-15} N. While issues related to miniaturization and spatial resolution (2.6 μm) are a few of the major hurdles to overcome, the potential benefits of harnessing the power of NMR and SFM as an analysis tool will, without question, attract a great deal of interest.

D. Closing Remarks

In this review we have briefly summarized the development of SFM as a tool for analysis. However, this work covers only a fraction of the literature in the broader field of proximal probe microscopies. A recent review notes that more than 5400 papers have appeared on this general topic from late 1995 to late 1997.[316] Thus, coverage of many intriguing areas was not tractable; many of these topics have been reviewed in another recent thematic issue of the Journal.[401] In addition, we have only mentioned in passing topics such as microfabrication or micromanipulation,[402] both of which are of clear importance to the advancement of SFM as a tool in the analytical sciences (as opposed to a surface characterization tool). In work soon to appear from our laboratory,[403] a tip has been used to construct immunoassay addresses of submicrometer dimension, advancing the density of addresses for our height-based concept for high-speed immunoassays.[152] Resch and co-workers have used a tip to build and translate multidimensional structures of 30 nm gold colloids on silane-modified silicon surfaces.[404] Using custom-made software, Resch and co-workers demonstrated the deliberate movement and rotation of a gold colloid dimer that was formed by connecting two colloids together through a dithiol coupling agent. Taken together, the unprecedented levels of sample interrogation and manipulation addressable with the advent of SFM will open a new pathway in the design of nanoscale landscapes and new avenues in the analytical sciences.

VI. Acknowledgments

Portions of the works cited from the author's laboratory were supported by the U.S. Department of Energy and by the National Science Foundation (Grant AIR-9601789). The Ames Laboratory is operated for the U.S. Department of Energy under Contract No. W-7405-eng-82.

VII. References

(1) Keller, R. A. *Chem. Rev.* **1999**, *99*, 2929.
(2) Kneipp, K. *Chem. Rev.* **1999**, *99*, 2957.
(3) Dunn, R. C. *Chem. Rev.* **1999**, *99*, 2891.
(4) Orden, A. V.; Machara, N. P.; Goodwin, P. M.; Keller, R. A. *Anal. Chem.* **1998**, *70*, 1444.
(5) Demas, J. N.; Wu, M.; Goodwin, P. M.; Affleck, R. L.; Keller, R. A. *Appl. Spectrosc.* **1998**, *52*, 755.
(6) Enderlein, J.; Keller, R. A. *Appl. Spectrosc.* **1997**, *51*, 443.
(7) Wu, M.; Goodwin, P. M.; Ambrose, W. P.; Keller, R. A. *J. Phys. Chem.* **1996**, *100*, 17406.
(8) Keller, R. A.; Ambrose, W. P.; Goodwin, P. M.; Jett, J. H.; Martin, J. C.; Wu, M. *Appl. Spectrosc.* **1996**, *50*, 12A.
(9) Ambrose, W. P.; Goodwin, P. M.; Martin, J. C.; Keller, R. A. *Phys. Rev. Lett.* **1994**, *72*, 160.
(10) Tellinghuisen, J.; Goodwin, P. M.; Ambrose, W. P.; Martin, J. C.; Keller, R. A. *Anal. Chem.* **1994**, *66*, 64.
(11) Tan, W.; Yeung, E. S. *Anal. Chem.* **1997**, *69*, 4242.
(12) Nie, S.; Chiu, D. T.; Zare, R. N. *Anal. Chem.* **1995**, *67*, 2849.
(13) Nie, S.; Chiu, D. T.; Zare, R. N. *Science* **1994**, *266*, 1018.
(14) Petit-Dominguez, M. D.; Shen, H.; Heineman, W. R.; Seliskar, C. J. *Anal. Chem.* **1997**, *69*, 703.
(15) Hofbauer, M.; Heineman, W. R.; Kreishman, G. P.; Steckhan, E. *Anal. Chem.* **1999**, *71*, 399.
(16) Hu, Z.; Seliskar, C. J.; Heineman, W. R. *Anal. Chem.* **1998**, *70*, 5230.
(17) Swaile, B. H.; Blubaugh, E. A.; Seliskar, C. J.; Heineman, W. R. *Anal. Chem.* **1998**, *70*, 4326.
(18) Barroso-Fernandez, B.; Lee-Alvarez, M. T.; Heineman, W. R. *Anal. Chim. Acta* **1998**, *370*, 221.
(19) Gavin, P. F.; Ewing, A. G. *J. Microcolumn Sep.* **1998**, *10*, 357.
(20) Swanek, B. R.; Franklin, D.; Ewing, A. G. *Chem. Anal.* **1998**, *146*, 355.
(21) Kennedy, R. *Chem. Rev.* **1999**, *99*, 3081.
(22) Lyon, L. A.; Musick, M. D.; Natan, M. J. *Anal. Chem.* **1998**, *70*, 5177.
(23) Brown, K. R.; Natan, M. J. *Langmuir* **1998**, *14*, 726.
(24) Keating, C. D.; Musick, M. D.; Lyon, L. A.; Brown, K. R.; Baker, B. E.; Pena, D. J.; Feldheim, D. L.; Mallouk, T. E.; Natan, M. J. *ACS Symp. Ser.* **1997**, *679*, 7.
(25) Feldstein, M. J.; Keating, C. D.; Liau, Y.-H.; Natan, M. J.; Scherer, N. F. *J. Am. Chem. Soc.* **1997**, *119*, 9.
(26) Seraphin, A. A.; Ngiam, S.-T.; Kolenbrander, K. D. *J. Appl. Phys.* **1996**, *80*, 6429.
(27) Koper, O. B.; Lagadic, I.; Volodin, A.; Klabunde, K. J. *Chem. Mater.* **1997**, *9*, 2468.
(28) Emory, S. R.; Haskins, W.; Nie, S. *J. Am. Chem. Soc.* **1998**, *120*, 8009.
(29) Emory, S. R.; Nie, S. *J. Phys. Chem. B.* **1998**, *102*, 493.
(30) Perrin, A.; Lanet, V.; Theretz, A. *Langmuir* **1997**, *13*, 2557.
(31) Sweedler, J. V. *Chem. Rev.* **1999**, *99*, 3133.
(32) Waters, L. C.; Jacobson, S. C.; Kroutchinina, N.; Khandurina, J.; Foote, R. S.; Ramsey, J. M. *Anal. Chem.* **1998**, *70*, 5172.
(33) Jacobson, S. C.; Culbertson, C. T.; Daler, J. E.; Ramsey, J. M. *Anal. Chem.* **1998**, *70*, 3476.
(34) Kutter, J. P.; Jacobson, S. C.; Matsubara, N.; Ramsey, J. M. *Anal. Chem.* **1998**, *70*, 3291.
(35) Fister, J. C.; Jacobson, S. C.; Davis, L. M.; Ramsey, J. M. *Anal. Chem.* **1998**, *70*, 431.
(36) Kutter, J. P.; Jacobson, S. C.; Ramsey, J. M. *Anal. Chem.* **1997**, *69*, 5165.
(37) Suenram, R. D.; Grabow, J. U.; Zuban, A.; Leonov, I. *Rev. Sci. Instrum.* **1999**, *70*, 2127.
(38) Ibrahim, M. S.; Lofts, R. S.; Jahrling, P. B.; Henchal, E. A.; Weedn, V. W.; Northrup, M. A.; Belgrader, P. *Anal. Chem.* **1998**, *70*, 2013.
(39) Binnig, G.; Rohrer, H. *Helv. Phys. Acta* **1982**, *55*, 726.
(40) Binnig, G.; Quate, C. F.; Gerber, C. *Phys. Rev. Lett.* **1986**, *56*, 930.
(41) Hallmark, V. N.; Chiang, S.; Rabolt, J. F.; Swalen, J. D.; Wilson, R. J. *Phys. Rev. Lett.* **1987**, *59*, 2879.
(42) Ohtani, H.; Wilson, R. J.; Chiang, S.; Mate, C. M. *Phys. Rev. Lett.* **1988**, *60*, 2398.
(43) Widrig, C. A.; Alves, C. A.; Porter, M. D. *J. Am. Chem. Soc.* **1991**, *113*, 2805.
(44) Poirier, G. E. *Chem. Rev.* **1997**, *97*, 1117.
(45) Clemmer, C. R.; Beebe, T. P., Jr. *Science* **1991**, *251*, 640.
(46) Weisenhorn, A. L.; Gaub, H. E.; Hansma, H. G.; Sinsheimer, R. L.; Kelderman, G. L.; Hansma, P. K. *Scanning Microsc.* **1990**, *4*, 511.
(47) Hansma, H. G.; Sinsheimer, R. L.; Gould, S. A. C.; Weisenhorn, A. L.; Gaub, H. E.; Hansma, P. K. AIP Conference Proceedings, Santa Barbara, CA, 1991.
(48) Hansma, H. G.; Vesenka, J.; Siegerist, C.; Kelderman, G.; Morrett, H.; Sinsheimer, R. L.; Elings, V.; Bustamante, C.; Hansma, P. K. *Science* **1992**, *256*, 1180.
(49) Hansma, H. G.; Pietrasanta, L. *Curr. Opin. Chem. Biol.* **1998**, *2*, 579.
(50) Hansma, H. G. *J. Vac. Sci. Technol., B* **1996**, *14*, 1390.
(51) Winograd, N. *Anal. Chem.* **1993**, *65*, 622A.
(52) Benninghoven, A.; Hagenhoff, B.; Niehuis, E. *Anal. Chem.* **1993**, *65*, 630A.

(53) Tarlov, M. J.; Burgess, D. R. F., Jr.; Gillen, G. *J. Am. Chem. Soc.* **1993**, *115*, 5305.
(54) Lopez, G. P.; Biebuyck, H. A.; Whitesides, G. M. *Langmuir* **1993**, *9*, 1513.
(55) Wollman, E. W.; Frisbie, C. D.; Wrighton, M. S. *Langmuir* **1993**, *9*, 1517.
(56) *Scanning Tunneling Microscopy and Spectroscopy: Theory, Techniques, and Applications*; Bonnell, D. A., Ed.; VCH Publishers: New York, 1993.
(57) Shiku, H.; Dunn, R. C. *Anal. Chem.* **1999**, *71*, 23A.
(58) Hollars, C. W.; Dunn, R. C. *Biophys. J.* **1998**, *75*, 342.
(59) Talley, C. E.; Lee, M. A.; Dunn, R. C. *Appl. Phys. Lett.* **1998**, *72*, 2954.
(60) Talley, C. E.; Cooksey, G. A.; Dunn, R. C. *Appl. Phys. Lett.* **1996**, *69*, 3809.
(61) Lal, R.; John, S. A. *Am. J. Physiol. (Cell Physiol.)* **1994**, *35*, C1.
(62) Service, R. F. *Science* **1996**, *274*, 723.
(63) Yu, E. T. *Mater. Sci. Eng. R* **1996**, *R17*, 147.
(64) Feenstra, R. M.; Griffith, J. E. In *Semiconductor Characterization*; Bullis, W. M., Seiler, D. G., Diebold, A. C., Eds.; AIP Press: Woodbury, NY, 1996; p 295.
(65) *Procedures in Scanning Probe Microscopies*; Colton, R. J., Engel, A., Frommer, J. E., Gaub, H. E., Gewirth, A. A., Guckenberger, R., Rabe, J., Heckl, W. M., Parkinson, B., Eds.; John Wiley & Sons: New York, 1998.
(66) Burnham, N. A.; Colton, R. J. In *Scanning Tunneling Microscopy and Spectroscopy*; Bonnell, D. A., Ed.; VCH Publisher: New York, 1993; p 191.
(67) Bhushan, B. In *Handbook of Micro/Nano Tribology*; Bhushan, B., Ed.; CRC Press: Boca Raton, FL, 1995; p 3.
(68) Ogletree, D. F.; Carpick, R. W.; Salmeron, M. *Rev. Sci. Instrum.* **1996**, *67*, 3298.
(69) Magonov, S. N.; Reneker, D. H. *Annu. Rev. Mater. Sci.* **1997**, *27*, 175.
(70) Noy, A.; Sanders, C. H.; Vezenov, D. V.; Wong, S. S.; Lieber, C. M. *Langmuir* **1998**, *14*, 1508.
(71) Finot, M. O.; McDermott, M. T. *J. Am. Chem. Soc.* **1997**, *119*, 8564.
(72) Whangbo, M.-H.; Bar, G.; Brandsch, R. *Surf. Sci.* **1998**, *411*, L794.
(73) Magonov, S. N.; Elings, V.; Whangbo, M.-H. *Surf. Sci.* **1997**, *375*, L385.
(74) Radmacher, M.; Tillmann, R. W.; Fritz, M.; Gaub, H. E. *Science* **1992**, *257*, 1900.
(75) Salmeron, M. *MRS Bull.* **1993**, *18*, 20.
(76) Maivald, P.; Butt, H. J.; Gould, S. A. C.; Prater, C. B.; Drake, B.; Gurley, J. A.; Elings, B. B.; Hansma, P. K. *Nanotechnology* **1991**, *2*, 103.
(77) Kiridena, W.; Jain, V.; Kuo, P. K.; Liu, G.-Y. *Surf. Interface Anal.* **1997**, *25*, 383.
(78) Martin, Y.; Abraham, D. W.; Wickramasinghe, H. K. *Appl. Phys. Lett.* **1988**, *52*, 1103.
(79) Stern, J. E.; Terris, B. D.; Mamin, H. J.; Rugar, D. *Appl. Phys. Lett.* **1988**, *53*, 2717.
(80) Terris, B. D.; Stern, J. E.; Ruger, D.; Mamin, H. J. *Phys. Rev. Lett.* **1989**, *63*, 2669.
(81) Nonnenmacher, M.; O'Boyle, M. P.; Wickramasinghe, H. K. *Appl. Phys. Lett.* **1991**, *58*, 2921.
(82) Inoue, T.; Yokoyama, H. *Thin Solid Films* **1994**, *243*, 399.
(83) Fujihira, M.; Kawate, H. *Thin Solid Films* **1994**, *242*, 163.
(84) Hu, J.; Xiao, X.-D.; Ogletree, D. F.; Salmeron, M. *Science* **1995**, *268*, 267.
(85) Thomas, R. C.; Tangyunyong, P.; Houston, J. E.; Michalske, T. A.; Crooks, R. M. *J. Phys. Chem.* **1994**, *98*, 4493.
(86) During, U.; Zuger, O.; Stalder, A. *J. Appl. Phys.* **1992**, *72*, 1778.
(87) Albrecht, T. R.; Grutter, P.; Horne, D.; Rugger, D. *J. Appl. Phys.* **1991**, *69*, 668.
(88) Saenz, J. J.; Garcia, N.; Grutter, P.; Meyer, E.; Heinzelmann, H.; Wiesendanger, R.; Rosenthaler, L.; Hidber, H. R.; Guntherodt, H.-J. *J. Appl. Phys.* **1987**, *62*, 4293.
(89) Martin, Y.; Williams, C. C.; Wickramasinghe, H. K. *J. Appl. Phys.* **1987**, *61*, 4723.
(90) Martin, Y.; Wickramasinghe, H. K. *Appl. Phys. Lett.* **1987**, *50*, 1455.
(91) Giessibl, F. J. *Science* **1995**, *267*, 68.
(92) Sugawara, Y.; Ueyama, H.; Uchihashi, T.; Ohta, M.; Morita, S.; Suzuki, M.; Mishima, S. *Appl. Surf. Sci.* **1997**, *113*−*114*, 364.
(93) Kitamura, S.; Suzuki, K.; Iwatsuki, M. *Jpn. J. Appl. Phys.* **1998**, *37*, 3765.
(94) Israelachvili, J. N. *Intermolecular and Surface Forces*, 2nd ed.; Academic Press: London, 1991.
(95) Ohnesorge, F.; Binnig, G. *Science* **1993**, *260*, 1451.
(96) Oden, P. I.; Tao, N. J.; Lindsay, S. M. *J. Vac. Sci. Technol., B* **1993**, *11*, 137.
(97) Xu, S.; Laibinis, P. E.; Liu, G.-Y. *J. Am. Chem. Soc.* **1998**, *120*, 9356.
(98) Sheiko, S. S.; Moller, M.; Reuvekam, E. M. C. M.; Zandbergen, H. W. *Phys. Rev. B* **1993**, *48*, 5675.
(99) Sarid, D. *Scanning Force Microscopy: With Applications to Electric, Magnetic and Atomic Forces*; Oxford University Press: New York, 1994.
(100) Meyer, G.; Amer, N. M. *Appl. Phys. Lett.* **1990**, *57*, 2089.
(101) Marti, O.; Colchero, J.; Mlynek, J. *Nanotechnology* **1990**, *1*, 141.
(102) Overney, R.; Meyer, E. *MRS Bull.* **1993**, *18*, 26.
(103) Hazel, J. L.; Tsukruk, V. V. *Trans. ASME* **1998**, *120*, 814.
(104) Sader, J. E.; Larson, I.; Mulvaney, P.; White, L. R. *Rev. Sci. Instrum.* **1995**, *66*, 3789.
(105) Neumeister, J. M.; Ducker, W. A. *Rev. Sci. Instrum.* **1994**, *65*, 2527.
(106) Warmack, R. J.; Zheng, X.-Y.; Thundat, T.; Allison, D. P. *Rev. Sci. Instrum.* **1994**, *65*, 394.
(107) Chen, G. Y.; Warmack, R. J.; Thundat, T.; Allison, D. P. *Rev. Sci. Instrum.* **1994**, *65*, 2532.
(108) Butt, H.-J.; Siedle, P.; Seifert, K.; Fendler, K.; Seeger, T.; Bamberg, E.; Weisenhorn, A. L.; Goldie, K.; Engel, A. *J. Microsc.* **1993**, *169*, 75.
(109) Labardi, M.; Allegrini, M.; Salerno, M.; Frediani, C.; Ascoli, C. *Appl. Phys. A* **1994**, *59*, 3.
(110) Lüthi, R.; Meyer, E.; Haefke, H.; Howald, L.; Gutmannsbauer, W.; Guggisberg, M.; Bammerlin, M.; Güntherodt, H.-J. *Surf. Sci.* **1995**, *338*, 247.
(111) Cleveland, J. P.; Manne, S.; Bocel, D.; Hansma, P. K. *Rev. Sci. Instrum.* **1993**, *64*, 403.
(112) Walters, D. A.; Cleveland, J. P.; Thomson, N. H.; Hansma, P. K.; Wendman, M. A.; Gurley, G.; Elings, V. *Rev. Sci. Instrum.* **1996**, *67*, 3583.
(113) Putman, C.; Igarashi, M.; Kaneko, R. *Jpn. J. Appl. Phys.* **1995**, *34*, L264.
(114) Marti, O.; Colchero, J.; Mlynek, J. In *Nanosources and Manipulation of Atoms Under High Fields and Temperatures*; Binh, V. T., Ed.; Kluwer Academic Publishers: Dordrecht, The Netherlands, 1993; p 253.
(115) Lantz, M. A.; O'Shea, S. J.; Hoole, A. C. F.; Welland, M. E. *Appl. Phys. Lett.* **1997**, *70*, 970.
(116) Carpick, R. W.; Ogletree, D. F.; Salmeron, M. *Appl. Phys. Lett.* **1997**, *70*, 1548.
(117) Griffith, J. E.; Grigg, D. A. *J. Appl. Phys.* **1993**, *74*, R 83.
(118) Atamny, F.; Baiker, A. *Surf. Sci.* **1995**, *323*, L314.
(119) Griffith, J. E.; Grigg, D. A.; Vasile, M. J.; Russell, P. E.; Fitzgerald, E. A. *J. Vac. Sci. Technol., A* **1992**, *10*, 674.
(120) Carpick, R. W.; Agrait, N.; Ogletree, D. F.; Salmeron, M. *Langmuir* **1996**, *12*, 3334.
(121) Odin, C.; Aime, J. P.; Kaakour, Z. E.; Bouhacina, T. *Surf. Sci.* **1994**, *317*, 321.
(122) Vesenka, J.; Miller, R.; Henderson, E. *Rev. Sci. Instrum.* **1994**, *65*, 2249.
(123) Oesterschulze, E.; Scholz, W.; Mihalcea, C.; Albert, D.; Sobisch, B.; Kulisch, W. *Appl. Phys. Lett.* **1997**, *70*, 435.
(124) Boisen, A.; Hansen, O.; Bouwstra, S. *J. Micromech. Microeng.* **1996**, *6*, 58.
(125) Mihalcea, C.; Scholz, W.; Werner, S.; Muenster, S.; Oesterschulze, E.; Kassing, R. *Appl. Phys. Lett.* **1996**, *68*, 3531.
(126) Frisbie, C. D.; Rozsnyai, L. F.; Noy, A.; Wrighton, M. S.; Lieber, C. M. *Science* **1994**, *265*, 2071.
(127) Green, J.-B. D.; McDermott, M. T.; Porter, M. D.; Siperko, L. M. *J. Phys. Chem.* **1995**, *99*, 10960.
(128) van der Vegte, E. W.; Hadziioannou, G. *Langmuir* **1997**, *13*, 4357.
(129) Knapp, H. F.; Wiegrabe, W.; Heim, M.; Eschrich, R.; Guckenberger, R. *Biophys. J.* **1995**, *69*, 708.
(130) Ulman, A. *An Introduction to Ultrathin Organic Films: From Langmuir*−*Blodgett to Self-Assembly*; Academic Press: San Diego, 1991.
(131) McDermott, M. T.; Green, J.-B. D.; Porter, M. D. *Langmuir* **1997**, *13*, 2504.
(132) Wenzler, L. A.; Moyes, G. L.; Beebe, T. P., Jr. *Rev. Sci. Instrum.* **1996**, *67*, 4191.
(133) Barrat, A.; Silberzan, P.; Bourdieu, L.; Chatenay, D. *Europhys. Lett.* **1992**, *20*, 633.
(134) Nakagawa, T.; Ogawa, K.; Kurumizawa, T. *J. Vac. Sci. Technol., B* **1994**, *12*, 2215.
(135) Nakagawa, T.; Ogawa, K.; Kurumizawa, T.; Ozaki, S. *Jpn. J. Appl. Phys.* **1993**, *32*, L294.
(136) Alley, R. L.; Komvopoulos, K.; Howe, R. T. *J. Appl. Phys.* **1994**, *76*, 5731.
(137) Nakagawa, T. *Jpn. J. Appl. Phys.* **1997**, *36*, L162.
(138) Ito, T.; Namba, M.; Buhlmann, P.; Umezawa, Y. *Langmuir* **1997**, *13*, 4323.
(139) Thundat, T.; Zheng, X.-Y.; Chen, G. Y.; Sharp, S. L.; Warmack, R. J.; Schowalter, L. J. *Appl. Phys. Lett.* **1993**, *63*, 2150.
(140) McGovern, M. E.; Kallury, K. M. R.; Thompson, M. *Langmuir* **1994**, *10*, 3607.
(141) Ducker, W. A.; Senden, T. J.; Pashley, R. M. *Nature* **1991**, *353*, 239.
(142) Ducker, W. A.; Senden, T. J.; Pashley, R. M. *Langmuir* **1992**, *8*, 1831.

(143) Kim, S.; Park, S.-K.; Park, C.; Jeon, I. C. *J. Vac. Sci. Technol., B* **1996**, *14*, 1318.
(144) Li, Y. Q.; Tao, N. J.; Pan, J.; Garcia, A. A.; Lindsay, S. M. *Langmuir* **1993**, *9*, 637.
(145) Karaman, M. E.; Meagher, L.; Pashley, R. M. *Langmuir* **1993**, *9*, 1220.
(146) Lee, G. U.; Kidwell, D. A.; Colton, R. J. *Langmuir* **1994**, *10*, 354.
(147) Hu, K.; Fan, F.-R. F.; Bard, A. J.; Hillier, A. C. *J. Phys. Chem. B* **1997**, *101*, 8298.
(148) Hegner, B.; Wagner, P.; Semenza, G. *Surf. Sci.* **1993**, *291*, 39.
(149) Wagner, P.; Hegner, M.; Guntherodt, H.-J.; Semenza, G. *Langmuir* **1995**, *11*, 3867.
(150) DeRose, J. A.; Thundat, T.; Nagahara, L. A.; Lindsay, S. M. *Surf. Sci.* **1991**, *256*, 102.
(151) Wagner, P.; Nock, S.; Spudich, J. A.; Volkmuth, W. D.; Chu, S.; Cicero, R. L.; Wade, C. P.; Lindford, M. R.; Chidsey, C. E. D. *J. Struct. Biol.* **1997**, *119*, 189.
(152) Jones, V. W.; Kenseth, J. R.; Porter, M. D.; Mosher, C. L.; Henderson, E. *Anal. Chem.* **1998**, *70*, 1233.
(153) Bezanilla, M.; Manne, S.; Laney, D. E.; Lyubchenko, Y. L.; Hansma, H. G. *Langmuir* **1995**, *11*, 655.
(154) Hansma, H. G.; Laney, D. E. *Biophys. J.* **1996**, *70*, 1933.
(155) Thomson, N. H.; Kasas, S.; Smith, B.; Hansma, H. G.; Hansma, P. K. *Langmuir* **1996**, *12*, 5905.
(156) Domke, J.; Rotsch, C.; Hansma, P. K.; Jacobson, K.; Radmacher, M. *Book of Abstracts*, 212th National Meeting of the American Chemical Society, Orlando, FL, 1996; p 178.
(157) Clemmer, C. R.; Beebe, T. P., Jr. *Scanning Microsc.* **1992**, *6*, 319.
(158) Bar, G.; Rubin, S.; Parikh, A. N.; Swanson, B. I.; Zawodzinski, T. A., Jr.; Whangbo, M.-H. *Langmuir* **1997**, *13*, 373.
(159) Droz, E.; Taborelli, M.; Descouts, P.; Wells, T. N. C.; Werlen, R. C. *J. Vac. Sci. Technol., B* **1996**, *14*, 1422.
(160) Green, J.-B. D.; McDermott, M. T.; Porter, M. D. *J. Phys. Chem.* **1996**, *100*, 13342.
(161) Hayes, W. A.; Kim, H.; Yue, X.; Perry, S.; Shannon, C. *Langmuir* **1997**, *13*, *2511*.
(162) Hegner, M.; Wagner, P.; Semenza, G. *FEBS Lett.* **1993**, *336*, 452.
(163) Hegner, M.; Dreir, M.; Wagner, P.; Semenza, G.; Guntherodt, H. J. *J. Vac. Sci. Technol., B* **1996**, *14*, 1418.
(164) Huang, J.; Hemminger, J. C. *J. Am. Chem. Soc.* **1993**, *115*, 3342.
(165) Xu, X.; Cruchon-Dupeyrat, S. J. N.; Garno, J. C.; Liu, G.-Y.; Jennings, G. K.; Yong, T.-H.; Laibinis, P. E. *J. Chem. Phys.* **1998**, *108*, 5002.
(166) Putnam, A.; Blackford, B. L.; Jericho, M. H.; Watanabe, M. O. *Surf. Sci.* **1989**, *217*, 276.
(167) Chidsey, C. E. D.; Loiacono, D. N.; Sleator, T.; Nakahara, S. *Surf. Sci.* **1988**, *200*, 45.
(168) Golan, Y.; Margulis, L.; Rubinstein, I. *Surf. Sci.* **1992**, *264*, 312.
(169) Lewis, M.; Tarlov, M. *J. Am. Chem. Soc.* **1995**, *117*, 9574.
(170) Zhang, Y.; Terrill, R.; Tanzer, T.; Bohn, P. *J. Am. Chem. Soc.* **1998**, *120*, 2654.
(171) Bhatia, S. K.; Hickman, J. J.; Ligler, F. S. *J. Am. Chem. Soc.* **1992**, *114*, 4432.
(172) Bhatia, S. K.; Teixeira, J. L.; Anderson, M.; Shriver-Lake, L. C.; Calvert, J. M.; Georger, J. H.; Hickman, J. J.; Dulcey, C. S.; Schoen, P. E.; Ligler, F. S. *Anal. Biochem.* **1993**, *208*, 197.
(173) Mooney, J. F.; Hunt, A. J.; McIntosh, J. R.; Liberko, C. A.; Walba, D. M.; Rogers, C. T. *Proc. Natl. Acad. Sci. U.S.A.* **1996**, *93*, 12287.
(174) Fodor, S. P. A.; Read, J. L.; Pirrung, M. C.; Stryer, L.; Lu, A. T.; Solas, D. *Science* **1991**, *251*, 767.
(175) Sigrist, H.; Collioud, A.; Clemence, J.-F.; Gao, H.; Luginbuhl, R.; Sanger, M.; Sundarababu, G. *Opt. Eng.* **1995**, *34*, 2339.
(176) Luginbuhl, R.; Collioud, A.; Siegenthaler, H.; Sigrist, H. In *Forces in Scanning Probe Methods*; Gutherodt, H.-J., Ed.; Kluwer Academic Publishers: Dordrecht, The Netherlands, 1995; p 615.
(177) Morgan, H.; Pritchard, D. J.; Cooper, J. M. *Biosens. Bioelectron.* **1995**, *10*, 841.
(178) Pritchard, D. J.; Morgan, H.; Cooper, J. M. *Angew. Chem., Int. Ed. Engl.* **1995**, *34*, 91.
(179) Dontha, N.; Nowall, W. B.; Kuhr, W. G. *Anal. Chem.* **1997**, *69*, 2619.
(180) Szostak, J. W. *Chem. Rev.* **1997**, *97*, 347.
(181) Kumar, A.; Whitesides, G. M. *Appl. Phys. Lett.* **1993**, *63*, 2002.
(182) Kumar, A.; Biebuyck, H. A.; Whitesides, G. M. *Langmuir* **1994**, *10*, 1498.
(183) Wilbur, J. L.; Biebuyck, H. A.; MacDonaold, J. C.; Whitesides, G. M. *Langmuir* **1995**, *11*, 825.
(184) Xia, Y.; Kim, E.; Zhao, X.-M.; Rogers, J. A.; Prentiss, M.; Whitesides, G. M. *Science* **1996**, *273*, 347.
(185) Xia, Y.; Whitesides, G. M. *Langmuir* **1997**, *13*, 2059.
(186) Xia, Y.; Venkateswaran, N.; Qin, D.; Tien, J.; Whitesides, G. M. *Langmuir* **1998**, *14*, 363.
(187) Wong, S.-S.; Takano, H.; Porter, M. D. *Anal. Chem.* **1998**, *70*, 5209.
(188) Larsen, N. B.; Biebuyck, H.; Delamarche, E.; Mitchel, B. *J. Am. Chem. Soc.* **1997**, *119*, 3017.
(189) Werts, M. P. L.; van der Vegte, E. W.; Hadziioannou, G. *Langmuir* **1997**, *13*, 4939.
(190) James, C. D.; Davis, R. C.; Kam, L.; Craighead, H. G.; Isaacson, M.; Turner, J. N.; Shain, W. *Langmuir* **1998**, *14*, 741.
(191) Bernard, A.; Delamarche, E.; Schmid, H.; Michel, B.; Bosshard, H. R.; Biebuyck, H. *Langmuir* **1998**, *14*, 2225.
(192) Kim, E.; Xia, Y.; Whitesides, G. M. *Nature* **1995**, *376*, 581.
(193) Kim, E.; Xia, Y.; Whitesides, G. M. *J. Am. Chem. Soc.* **1996**, *118*, 5722.
(194) Kim, E.; Whitesides, G. M. *J. Phys. Chem. B* **1997**, *101*, 855.
(195) Delamarche, E.; Schmid, H.; Michel, B.; Biebuyck, H. *Adv. Mater.* **1997**, *9*, 741.
(196) Delamarche, E.; Bernard, A.; Schmid, H.; Michel, B.; Biebuyck, H. *Science* **1997**, *276*, 779.
(197) Delamarche, E.; Bernard, A.; Schmid, H.; Bietsch, A.; Michel, B.; Biebuyck, H. *J. Am. Chem. Soc.* **1998**, *120*, 500.
(198) Israelachvili, J. N.; Tabor, D. *Proc. R. Soc. London, A* **1972**, *331*, 19.
(199) Israelachvili, J. N.; Tabor, D. *Prog. Surf. Membr. Sci.* **1973**, *7*, 1.
(200) Butt, H.-J.; Jaschke, M.; Ducker, W. *Bioelectrochem. Bioenerg.* **1995**, *38*, 191.
(201) Toikka, G.; Hayes, R. A. *J. Colloid Interface Sci.* **1997**, *191*, 102.
(202) Larson, I.; Drummond, C. J.; Chan, D. Y. C.; Grieser, F. *Langmuir* **1997**, *13*, 2109.
(203) Braithwaite, G. J. C.; Howe, A.; Luckham, P. F. *Langmuir* **1996**, *12*, 4224.
(204) Yoon, R.-H.; Flinn, D. H.; Rabinovich, Y. I. *J. Colloid Interface Sci.* **1997**, *185*, 363.
(205) Lin, X.-Y.; Creuzet, F.; Arribart, H. *J. Phys. Chem.* **1993**, *97*, 7272.
(206) Raiteri, R.; Martinoia, S.; Grattarola, M. *Biosens. Bioelectron.* **1996**, *11*, 1009.
(207) Huttl, G.; Beyer, D.; Muller, E. *Surf. Interface Anal.* **1997**, *25*, 543.
(208) Hillier, A. C.; Kim, S.; Bard, A. J. *J. Phys. Chem.* **1996**, *100*, 18808.
(209) Arai, T.; Fujihara, M. *J. Vac. Sci. Technol., B* **1996**, *14*, 1378.
(210) Gewirth, A.; Niece, B. *Chem. Rev.* **1997**, *97*, 1129.
(211) Ishino, T.; Hieda, H.; Tanaka, K.; Gemma, N. *Jpn. J. Appl. Phys.* **1994**, *33*, 4718.
(212) Vezenov, D. V.; Noy, A.; Rozsnyai, L. F.; Lieber, C. M. *J. Am. Chem. Soc.* **1997**, *119*, 2006.
(213) Reiner, E. S.; Radke, C. J. *Adv. Colloid Interface Sci.* **1993**, *58*, 87.
(214) van der Vegte, E. W.; Hadziioannou, G. *J. Phys. Chem., B* **1997**, *101*, 9563.
(215) Hu, K.; Bard, A. J. *Langmuir* **1997**, *13*, 5114.
(216) *CRC Handbook of Chemistry and Physics*, 72nd ed.; Lide, D. R., Ed.; CRC Press: Boca Raton, FL, 1991.
(217) Bain, C. D.; Whitesides, G. M. *Langmuir* **1989**, *5*, 1370.
(218) Hu, K.; Pyati, R.; Bard, A. J. *Anal. Chem.* **1998**, *70*, 2870.
(219) Larson, I.; Chan, D. Y. C.; Drummond, C. J.; Grieser, F. *Langmuir* **1997**, *13*, 2429.
(220) Horn, R. G.; Israelachvili, J. N. *J. Chem. Phys.* **1981**, *75*, 1400.
(221) Israelachvili, J. H.; Pashley, R. M. *Nature* **1982**, *300*, 341.
(222) O'Shea, S. J.; Welland, M. E.; Rayment, T. *Appl. Phys. Lett.* **1992**, *60*, 2356.
(223) McGonigal, G. C.; Bernhardt, R. H.; Yeo, Y. H.; Thomson, D. J. *J. Vac. Sci. Technol., B* **1991**, *9*, 1107.
(224) O'Shea, S. J.; Welland, M. E.; Pethica, J. B. *Chem. Phys. Lett.* **1994**, *223*, 336.
(225) Han, W.; Lindsay, S. M. *Appl. Phys. Lett.* **1998**, *72*, 1656.
(226) Derjaguin, B. V.; Muller, V. M.; Toporov, Y. P. *J. Colloid Interface Sci.* **1975**, *53*, 314.
(227) Johnson, K. L.; Kendall, K.; Roberts, A. D. *Proc. R. Soc. London, A* **1971**, *324*, 301.
(228) Noy, A.; Vezenov, D. V.; Lieber, C. M. *Annu. Rev. Mater. Sci.* **1997**, *27*, 381.
(229) Horn, R. G.; Israelachvili, J. N.; Pribac, F. *J. Colloid Interface Sci.* **1987**, *115*, 480.
(230) Thomas, R. C.; Houston, J. E.; Crooks, R. M.; Kim, T.; Michalske, T. A. *J. Am. Chem. Soc.* **1995**, *117*, 3830.
(231) Israelachvili, J. N. *J. Vac. Sci. Technol., A* **1992**, *10*, 2961.
(232) Thomas, R. C.; Houston, J. E.; Michalske, T. A.; Crooks, R. M. *Science* **1993**, *259*, 1883.
(233) Pimentel, G. C.; McClellan, A. L. *The Hydrogen Bond*; W. H. Freeman and Co.: San Francisco, CA, 1960.
(234) Binggeli, M.; Mate, C. M. *Appl. Phys. Lett.* **1994**, *65*, 415.
(235) Thundat, T.; Zheng, X.-Y.; Chen, G. Y.; Warmack, R. J. *Surf. Sci. Lett.* **1993**, *294*, L939.
(236) Fujihira, M.; Aoki, D.; Okabe, Y.; Takano, H.; Hokari, H.; Frommer, J.; Nagatani, Y.; Sakai, F. *Chem. Lett.* **1996**, *1996*, 499.
(237) Noy, A.; Frisbie, C. D.; Rozsnyai, L. F.; Wrighton, M. S.; Lieber, C. M. *J. Am. Chem. Soc.* **1995**, *117*, 7943.
(238) Sinniah, S. K.; Steel, A. B.; Miller, C. J.; Reutt-Robey, J. E. *J. Am. Chem. Soc.* **1996**, *118*, 8925.
(239) Feldman, K.; Tervoort, T.; Smith, P.; Spencer, N. D. *Langmuir* **1998**, *14*, 4, 372.

(240) Hoh, J. H.; Cleveland, J. P.; Prater, C. B.; Revel, J.-P.; Hansma, P. K. *J. Am. Chem. Soc.* **1992**, *114*, 4917.
(241) *CRC Handbook of Materials Science*; Lynch, C. T., Ed.; CRC Press: Boca Raton, FL, 1975.
(242) Han, T.; Williams, J. M.; Beebe, T. P., Jr. *Anal. Chim. Acta* **1995**, *307*, 365.
(243) Williams, J. M.; Han, T.; Beebe, T. P., Jr. *Langmuir* **1996**, *12*, 1291.
(244) Wenzler, L. A.; Moyes, G. L.; Raikar, G. N.; Hansen, R. L.; Harris, J. M.; Beebe, T. P., Jr.; Wood, L. L.; Saavedra, S. S. *Langmuir* **1997**, *13*, 3761.
(245) Wenzler, L. A.; Moyes, G. L.; Olson, L. G.; Harris, J. M.; Beebe, T. P., Jr. *Anal. Chem.* **1997**, *69*, 2855.
(246) Butt, H.-J. *Biophys. J.* **1991**, *60*, 1438.
(247) Weisenhorn, A. L.; Maivald, P.; Butt, H.-J.; Hansma, P. K. *Phys. Rev. B* **1992**, *45*, 11226.
(248) van der Werf, K. O.; Putman, C. A. J.; de Grooth, B. G.; Greve, J. *Appl. Phys. Lett.* **1994**, *65*, 1195.
(249) He, H. X.; Li, C. Z.; Song, J. Q.; Mu, T.; Wang, L.; Zhang, H. L.; Liu, Z. F. *Mol. Cryst. Liq. Cryst.* **1997**, *294*, 99.
(250) He, H. X.; Li, C. Z.; Wang, J. M.; Xu, X. J.; Liu, Z. F. *Acta Phys.-Chim. Sin.* **1997**, *13*, 293.
(251) Zhang, H.; He, H.-X.; Mu, T.; Liu, Z.-F. *Thin Solid Films* **1998**, *327*−*329*, 778.
(252) Tsukruk, V. V.; Bliznyuk, V. N. *Langmuir* **1998**, *14*, 446.
(253) Allinger, N. L.; Cava, M. P.; de Jongh, D. C.; Johnson, C. P.; Lebel, N. A.; Stevens, C. L. *Organic Chemistry*; Worth Publishers: New York, 1980.
(254) Lee, T. R.; Carey, R. I.; Biebuyck, H. A.; Whitesides, G. M. *Langmuir* **1994**, *10*, 741.
(255) Abbott, N. L.; Whitesides, G. M. *Langmuir* **1994**, *10*, 1493.
(256) Hudson, J. E.; Abruna, H. D. *J. Am. Chem. Soc.* **1996**, *118*, 6303.
(257) Carpick, R. W.; Salmeron, M. *Chem. Rev.* **1997**, *97*, 1163.
(258) Miyamoto, T.; Kaneko, R.; Ando, Y. *J. Tribol.* **1990**, *112*, 567.
(259) Radmacher, M.; Cleveland, J. P.; Fritz, M.; Hansma, H. G.; Hansma, P. K. *Biophys. J.* **1994**, *66*, 2159.
(260) Mizes, H. A.; Loh, K.-G.; Miller, R. J. D.; Ahuja, S. K.; Grabowski, E. F. *Appl. Phys. Lett.* **1991**, *59*, 2901.
(261) Berger, C. E. H.; van der Werf, K. O.; Kooyman, R. P. H.; de Grooth, B. G.; Greve, J. *Langmuir* **1995**, *11*, 4188.
(262) Hoh, J.; Revel, J.-P.; Hansma, P. K. *Nanotechnology* **1991**, *2*, 119.
(263) Rosa-Zeiser, A.; Weilandt, E.; Hild, S.; Marti, O. *Meas. Sci. Technol.* **1997**, *8*, 1333.
(264) Rosa, A.; Hild, S.; Marti, O. *Polym. Rep.* **1996**, *37*, 616.
(265) Miyatani, T.; Horii, M.; Rosa, A.; Fujihira, M.; Marti, O. *Appl. Phys. Lett.* **1997**, *71*, 2632.
(266) Ishino, T.; Hieda, H.; Tanaka, K.; Gemma, N. *J. Electroanal. Chem.* **1997**, *438*, 225.
(267) Radmacher, M.; Fritz, M.; Cleveland, J. P.; Walters, D. A.; Hansma, P. K. *Langmuir* **1994**, *10*, 3809.
(268) Radmacher, M.; Fritz, M.; Kacher, C. M.; Cleveland, J. P.; Hansma, P. K. *Biophys. J.* **1996**, *70*, 556.
(269) Willemsen, O. H.; Snel, M. M. E.; van der Werf, K. O.; de Grooth, B. G.; Greve, J.; Hinterdorfer, P.; Gruber, H. J.; Schindler, H.; van Kooyk, Y.; Figdor, C. G. *Biophys. J.* **1998**, *75*, 2220.
(270) Ludwig, M.; Dettmann, W.; Gaub, H. E. *Biophys. J.* **1997**, *72*, 445.
(271) Allen, S.; Chen, X.; Davies, J.; Davies, M. C.; Dawkes, A. C.; Edwards, J. C.; Roberts, C. J.; Tendler, S. J. B.; Willaims, P. M. *Appl. Phys. A* **1998**, *66*, S255.
(272) Chen, X.; Davies, M. C.; Roberts, C. J.; Tendler, S. J. B.; Williams, P. M.; Davies, J.; Dawkes, A. C.; Edwards, J. C. *Langmuir* **1997**, *13*, 4106.
(273) Baselt, D. R.; Baldeschwieler, J. D. *J. Appl. Phys.* **1994**, *76*, 33.
(274) Maganov, S. N.; Whangbo, M.-H. *Surface Analysis with STM and AFM*; VCH−Wiley: Weinheim, Germany, 1996.
(275) Tsukruk, V. V. *Rubber Chem. Technol.* **1997**, *70*, 430.
(276) Roberts, C. J.; Davies, M. C.; Shakesheff, K. M.; Tendler, S. J. B.; Williams, P. M. *Trends Polym. Sci.* **1996**, *4*, 420.
(277) Kajiyama, T.; Tanaka, K.; Ge, S. R.; Takahara, A. *Prog. Surf. Sci.* **1996**, *52*, 1.
(278) Magonov, S. N. *Polym. Sci., Ser. B* **1996**, *38*, 143.
(279) *Scanning Probe Microscopy of Polymers*; Ratner, B. D., Tsukruk, V. V., Eds.; American Chemical Society: Washington, DC, 1998; Vol. 694.
(280) Goh, M. C. *Adv. Chem. Phys.* **1995**, *91*, 1.
(281) Kendall, K. *Nature* **1986**, *319*, 203.
(282) Pollock, H. M. In *Fundamentals of Friction: Macroscopic and Microscopic Processes*; Singer, I. L., Pollock, H. M., Eds.; Kluwer Academic Publishers: Dordrecht, The Netherlands, 1992; p 77.
(283) Israelachvili, J. N. In *Handbook of Micro/Nanotribology*; Bhushan, B., Ed.; CRC Press: Boca Raton, FL, 1995; p 267.
(284) Zhou, Y.; Fan, H.; Fong, T.; Lopez, G. P. *Langmuir* **1998**, *14*, 660.
(285) Lio, A.; Charych, D. H.; Salmeron, M. *J. Phys. Chem. B* **1997**, *101*, 3800.
(286) Koutso, V.; van der Vegte, E. W.; Grim, P. C. M.; Hadziioannou, G. *Macromolecules* **1998**, *31*, 116.
(287) Werts, M. P. L.; van der Vegte, E. W.; Grayer, V.; Esselink, E.; Tsitsilanis, C.; Hadziioannou, G. *Adv. Mater.* **1998**, *10*, 452.
(288) Overney, R. M.; Meyer, E.; Frommer, J.; Brodbeck, D.; Luthi, R.; Howald, L.; Guntherodt, H.-J.; Fujihira, M.; Takano, H.; Gotoh, Y. *Nature* **1992**, *359*, 133.
(289) Overney, R. M.; Meyer, E.; Frommer, J.; Guntherodt, H.-J.; Fujihjira, M.; Takano, H.; Gotoh, Y. *Langmuir* **1994**, *10*, 1281.
(290) Dufrene, Y. F.; Barger, W. R.; Green, J.-B. D.; Lee, G. U. *Langmuir* **1997**, *13*, 4779.
(291) Chi, L. F.; Gleiche, M.; Fuchs, H. *Langmuir* **1998**, *14*, 875.
(292) Cohen, S. R.; Weissbuch, I.; Popovitz-Biro, R.; Majewski, J.; Mauder, H. P.; Lavi, R.; Leiserowitz, L.; Lahav, M. *Isr. J. Chem.* **1996**, *36*, 97.
(293) Fujihira, M.; Takano, H. *J. Vac. Sci. Technol., B* **1994**, *12*, 1860.
(294) Xiao, X.-D.; Hu, J.; Charych, D. H.; Salmeron, M. *Langmuir* **1996**, *12*, 235.
(295) Lio, A.; Morant, C.; Ogletree, D. F.; Salmeron, M. *J. Phys. Chem. B* **1997**, *101*, 4767.
(296) Last, J. A.; Ward, M. D. *Adv. Mater.* **1996**, *8*, 730.
(297) Last, J. A.; Hillier, A. C.; Hooks, D. E.; Maxson, J. B.; Ward, M. D. *Chem. Mater.* **1998**, *10*, 422.
(298) Nisman, R.; Smith, P.; Vansco, G. J. *Langmuir* **1994**, *10*, 1667.
(299) McKendry, R.; Theoclitou, M.-E.; Rayment, T.; Abell, C. *Nature* **1998**, *391*, 566.
(300) Wang, J.; Kenseth, J. R.; Jones, V. W.; Green, J.-B. D.; McDermott, M. T.; Porter, M. D. *J. Am. Chem. Soc.* **1997**, *119*, 12796.
(301) Baselt, D. R.; Baldeschwieler, J. D. *J. Vac. Sci. Technol., B* **1992**, *10*, 2316.
(302) Haustead, G.; Gladfelter, W. L.; Weberg, E. B. *Langmuir* **1994**, *10*, 4295.
(303) Tamayo, J.; Garcia, R. *Langmuir* **1996**, *2*, 4430.
(304) Leclere, P.; Lazzaroni, R.; Bredas, J. L.; Yu, J. M.; Dubois, P.; Jerome, R. *Langmuir* **1996**, *12*, 4317.
(305) Magonov, S. N.; Eling, V.; Whangbo, M.-H. *Surf. Sci.* **1997**, *375*, L385.
(306) Anezykowski, B.; Kruger, D.; Fuchs, H. *Phys. Rev. B.* **1996**, *53*, 15485.
(307) Burgess, J. D.; Jones, V. W.; Porter, M. D.; Rhoten, M. C.; Hawkridge, F. M. *Langmuir* **1998**, *14*, 6628.
(308) Chi, L. F.; Jacobi, S.; Fuchs, H. *Thin Solid Films* **1996**, *284*−*285*, 403.
(309) Lu, J.; Guggisberg, M.; Luthi, R.; Kubon, M.; Scandella, L.; Gerber, C.; Meyer, E.; Guntherodt, H.-J. *Appl. Phys.* **1998**, *A66*, S273.
(310) Piner, R. D.; Mirkin, C. A. *Langmuir* **1997**, *13*, 6864.
(311) Tian, F.; Xiao, X.; Loy, M. M. T.; Wang, C.; Bai, C. *Langmuir* **1999**, *15*, 244.
(312) Xu, L.; Salmeron, M. *J. Phys. Chem. B* **1998**, *102*, 7210.
(313) Dai, Q.; Hu, J.; Freedman, A.; Robinson, G. N.; Salmeron, M. *J. Phys. Chem.* **1996**, *100*, 9.
(314) Hu, J.; Xiao, X.-D.; Salmeron, M. *Appl. Phys. Lett.* **1995**, *67*, 476.
(315) Allen, S.; Davies, M. C.; Roberts, C. J.; Tendler, S. J. B.; Williams, P. M. *TIBTECH* **1997**, *15*, 101.
(316) Bottomley, L. A. *Anal. Chem.* **1998**, *70*, 425R.
(317) Hansma, H. G.; Kim, K. J.; Laney, D. E.; Garcia, R. A.; Argaman, M.; Allen, M. J.; Parsons, S. M. *J. Struct. Biol.* **1997**, *119*, 99.
(318) Hoh, J. H.; Hansma, P. K. *Trends Cell Biol.* **1992**, *2*, 208.
(319) Leggett, G. L.; Davies, M. C.; Jackson, D. E.; Tendler, S. J. B. *J. Electron Spectrosc. Relat. Phenom.* **1996**, *81*, 249.
(320) Vinckier, A.; Semenza, G. *FEBS Lett.* **1998**, *430*, 12.
(321) Leckband, D.; Israelachvili, J.; Schmitt, F.-J.; Knoll, W. *Science* **1992**, *255*, 1419.
(322) Helm, C.; Knoll, W.; Israelachvili, J. *Proc. Natl. Acad. Sci. U.S.A.* **1991**, *88*, 8169.
(323) Evans, E.; Berk, D.; Leung, A. *Biophys. J.* **1991**, *59*, 838.
(324) Wang, N.; Butler, J.; Ingber, D. *Science* **1993**, *260*, 1124.
(325) Cluzel, P.; Lebrun, A.; Heller, C.; Lavery, R.; Viovy, J.-L.; Chatenay, D.; Caron, F. *Science* **1996**, *271*, 792.
(326) Ashkin, A.; Dziedzic, J.; Yamane, T. *Nature* **1987**, *330*, 769.
(327) Smith, S.; Cui, Y.; Bustamante, C. *Science* **1996**, *271*, 795.
(328) Svoboda, K.; Schmidt, C.; Schnapp, B.; Block, S. *Nature* **1993**, *365*, 721.
(329) Finer, J.; Simmons, R.; Spudich, J. *Nature* **1994**, *368*, 113.
(330) Kuo, S.; Sheetz, M. *Science* **1993**, *260*, 232.
(331) Lee, G. U.; Chrisey, L. A.; Colton, R. J. *Science* **1994**, *266*, 771.
(332) Dammer, U.; Anselmetti, D.; Dreier, M.; Hegner, M.; Huber, W.; Hurst, J.; Misevic, G.; Guntherodt, H.-J. In *Forces in Scanning Probe Methods*; Guntherodt, H.-J., Ed.; Kluwer Academic Publishers: Dordrecht, The Netherlands, 1995; p 625.
(333) Moy, V. T.; Florin, E.-L.; Gaub, H. E. *Colloids Surf. A* **1994**, *93*, 343.
(334) Moore, A.; Williams, P. M.; Davies, M. C.; Jackson, D. E.; Roberts, C. J.; Tendler, S. J. B. *J. Chem. Soc., Perkin Trans.* **1998**, *2*, 253.
(335) Grubmuller, H.; Heymann, B.; Tavan, P. *Science* **1996**, *271*, 997.
(336) Fritz, J.; Anselmetti, D.; Jarchow, J.; Fernandez-Busquets, X. *J. Struct. Biol.* **1997**, *119*, 165.
(337) Florin, E.-L.; Rief, M.; Lehmann, H.; Ludwig, M.; Dornmair, C.; Moy, V. T.; Gaub, H. E. *Biosens. Bioelectron.* **1995**, *10*, 895.

(338) Florin, E.-L.; Moy, V. T.; Gaub, H. E. *Science* **1994**, *264*, 415.
(339) Chilkoti, A.; Boland, T.; Ratner, B. D.; Stayton, P. S. *Biophys. J.* **1995**, *69*, 2125.
(340) Allen, S.; Davies, J.; Dawkes, A. C.; Davies, M. C.; Edwards, J. C.; Parker, M. C.; Roberts, C. J.; Sefton, J.; Tendler, S. J. B.; Williams, P. M. *FEBS Lett.* **1996**, *390*, 161.
(341) Moy, V. T.; Florin, E.-L.; Gaub, H. E. *Science* **1994**, *266*, 257.
(342) Hinterdorfer, P.; Baumgartner, W.; Gruber, H. J.; Schilcher, K.; Schindler, H. *Proc. Natl. Acad. Sci. U.S.A.* **1996**, *93*, 3477.
(343) Dammer, U.; Hegner, M.; Anselmetti, D.; Wagner, P.; Dreier, M.; Huber, W.; Guntherodt, H.-J. *Biophys. J.* **1996**, *70*, 2437.
(344) Ludwig, M.; Moy, V. T.; Rief, M.; Florin, R.-L.; Gaub, H. E. *Microsc. Microanal. Microstruct.* **1994**, *5*, 321.
(345) Pierce, M.; Stuart, J.; Pungor, A.; Dryden, P.; Hlady, V. *Langmuir* **1994**, *10*, 3217.
(346) Hoh, J. H.; Hillner, P. E.; Hansma, P. K. *Proc. Microsc. Soc. Am.* **1994**, *52*, 1054.
(347) Han, W.; Lindsay, S. M.; Jing, T. *Appl. Phys. Lett.* **1996**, *69*, 4111.
(348) Stuart, J. K.; Hlady, V. *Langmuir* **1995**, *11*, 1368.
(349) Allen, S.; Chen, X.; Davies, J.; Davies, M. C.; Dawkes, A. C.; Edwards, J. C.; Roberts, C. J.; Sefton, J.; Tendler, S. J. B.; Williams, P. M. *Biochemistry* **1997**, *36*, 7457.
(350) Chen, X.; Patel, N.; Davies, M. C.; Roberts, C. J.; Tendler, S. J. B.; Williams, P. M.; Davies, J.; Dawkes, A. C.; Edwards, J. C. *Appl. Phys. A* **1998**, *66*, S631.
(351) Dammer, U.; Popescu, O.; Wagner, P.; Anselmetti, D.; Guntherodt, H.-J.; Misevic, G. N. *Science* **1995**, *267*, 1173.
(352) Vinckier, A.; Gervasoni, P.; Zaugg, F.; Ziegler, U.; Lindner, P.; Groscurth, P.; Pluckthun, A.; Semenza, G. *Biophys. J.* **1998**, *74*, 3256.
(353) Nakajima, H.; Kunioka, Y.; Nakano, K.; Shimizu, K.; Seto, M.; Ando, T. *Biochem. Biophys. Res. Commun.* **1997**, *234*, 178.
(354) Rief, M.; Oesterhelt, F.; Heymann, B.; Gaub, H. E. *Science* **1997**, *275*, 1295.
(355) Rief, M.; Gautel, M.; Oesterhelt, F.; Fernandez, J. M.; Gaub, H. E. *Science* **1997**, *276*, 1109.
(356) Mitsui, K.; Hara, M.; Ikai, A. *FEBS Lett.* **1996**, *385*, 29.
(357) Noy, A.; Vezenov, D. V.; Kayyem, J. F.; Meade, T. J.; Lieber, C. M. *Chem. Biol.* **1997**, *4*, 519.
(358) Boland, T.; Ratner, B. D. *Proc. Natl. Acad. Sci. U.S.A.* **1995**, *92*, 5297.
(359) Laney, D. E.; Garcia, R. A.; Parsons, S. M.; Hansma, H. G. *Biophys. J.* **1997**, *72*, 806.
(360) Thundat, T.; Allison, D. P.; Warmack, R. J.; Doktycz, M. J.; Jacobson, K. B.; Brown, G. M. *J. Vac. Sci. Technol., A* **1993**, *11*, 824.
(361) Thundat, T.; Allison, D. P.; Warmack, R. J.; Ferrell, T. R. *Ultramicroscopy* **1992**, *42*−*44*, 1101.
(362) Han, W.; Dlakic, M.; Zhu, Y. J.; Lindsay, S. M.; Harrington, R. E. *Proc. Natl. Acad. Sci. U.S.A.* **1997**, *94*, 10565.
(363) Han, W.; Lindsay, S. M.; Dlakic, M.; Harrington, R. E. *Nature* **1997**, *386*, 563.
(364) Argaman, M.; Golan, R.; Thomson, N. H.; Hansma, H. G. *Nucleic Acids Res.* **1997**, *25*, 4379.
(365) Hansma, H. G.; Bezanilla, M.; Nudler, E.; Hansma, P. K.; Hoh, J.; Kashlev, M.; Firouz, N.; Smith, B. L. *Probe Microsc.* **1998**, *1*, 127.
(366) Allison, D. P.; Kerper, P. S.; Doktycz, M. J.; Thundat, T.; Modrich, P.; Larimer, F. W.; Johnson, D. K.; Hoyt, P. R.; Mucenski, M. L.; Warmack, R. J. *Genomics* **1997**, *41*, 379.
(367) Bezanilla, M.; Drake, B.; Nudler, E.; Kashlev, M.; Hansma, P. K.; Hansma, H. G. *Biophys. J.* **1994**, *67*, 2454.
(368) Fang, Y.; Spisz, T. S.; Wiltshire, T.; D'Costa, N. P.; Bankman, I. N.; Reeves, R. H.; Hoh, J. H. *Anal. Chem.* **1998**, *70*, 2123.
(369) Coury, J. E.; McFail-Isom, L.; Williams, L. D.; Bottomley, L. A. *J. Vac. Sci. Technol., A* **1995**, *13*, 1746.
(370) Coury, J. E.; McFail-Isom, L.; Williams, L. D.; Bottomley, L. A. *Proc. Natl. Acad. Sci. U.S.A.* **1996**, *93*, 12283.
(371) Hansma, H. G.; Weisenhorn, A. L.; Gould, S. A. C.; Sinsheimer, R. L.; Gaub, H. E.; Stucky, G. D.; Zaremba, C. M.; Hansma, P. K. *J. Vac. Sci. Technol., B* **1991**, *9*, 1282.
(372) Pope, L. H.; Davies, M. C.; Roberts, C. J.; Tendler, S. J. B.; Williams, P. M. *Anal. Commun.* **1998**, *35*, 5H.
(373) Han, W.; Mou, J.; Sheng, J.; Yang, J.; Shao, Z. *Biochemistry* **1995**, *34*, 8215.
(374) Zhang, Y.; Sheng, S. J.; Shao, Z. *Biophys. J.* **1996**, *71*, 2168.
(375) Heim, M.; Steigerwald, R.; Guckenberger, R. *J. Struct. Biol.* **1997**, *119*, 212.
(376) Quist, A. P.; Bergman, A. A.; Reimann, C. T.; Oscarsson, S. O.; Sundqvist, B. U. R. *Scanning Microsc.* **1995**, *9*, 395.
(377) Masai, J.; Sorin, T.; Kondo, S. *J. Vac. Sci. Technol., A* **1990**, *8*, 713.
(378) Mazzola, L. T.; Fodor, S. P. A. *Biophys. J.* **1995**, *68*, 1653.
(379) Browning-Kelley, M. E.; Wadu-Mesthrige, K.; Hari, V.; Liu, G. Y. *Langmuir* **1997**, *13*, 343.
(380) Perrin, A.; Theretz, A.; Mandrand, B. *Anal. Biochem.* **1998**, *256*, 200.
(381) Radmacher, M.; Fritz, M.; Hansma, H. G.; Hansma, P. K. *Science* **1994**, *265*, 1577.
(382) Wittstock, G.; Yu, K.; Halsall, H. B.; Ridgway, T. H.; Heineman, W. R. *Anal. Chem.* **1995**, *67*, 3578.
(383) Pierce, D. T.; Unwin, P. K.; Bard, A. J. *Anal. Chem.* **1992**, *64*, 1795.
(384) Pierce, D. T.; Bard, A. J. *Anal. Chem.* **1993**, *65*, 3598.
(385) Fan, F.-R. F.; Bard, A. J. *Science* **1995**, *267*, 871.
(386) Shiku, H.; Matsue, T.; Uchida, I. *Anal. Chem.* **1996**, *68*, 1276.
(387) Shiku, H.; Hara, Y.; Matsue, T.; Uchida, I.; Yamauchi, T. *J. Electroanal. Chem.* **1997**, *438*, 187.
(388) Yasukawa, T.; Kondo, Y.; Uchida, I.; Matsue, T. *Chem. Lett.* **1998**, 767.
(389) Dai, H.; Hafner, J. H.; Rinzler, A. G.; Colbert, D. T.; Smalley, R. E. *Nature* **1996**, *384*, 147.
(390) Wong, S. S.; Harper, J. D.; Lansbury, P. T., Jr.; Lieber, C. M. *J. Am. Chem. Soc.* **1998**, *120*, 603.
(391) Wong, S. S.; Woolley, A. T.; Joselevich, E.; Cheung, C. L.; Lieber, C. M. *J. Am. Chem. Soc.* **1998**, *120*, 8557.
(392) Wong, S. S.; Joselevich, E.; Woolley, A. T.; Cheung, C. L.; Lieber, C. M. *Nature* **1998**, *394*, 52.
(393) Hahner, G.; Marti, A.; Spencer, N. D. *Tribol. Lett.* **1997**, *3*, 359.
(394) Minne, S. C.; Flueckiger, P.; Soh, H. T.; Quate, C. F. *J. Vac. Sci. Technol., B* **1995**, *13*, 1380.
(395) Ried, R. P.; Mamin, H. J.; Terris, B. D.; Fan, L. S.; Rugar, D. *Microelectromech. Syst.* **1997**, *6*, 294.
(396) Brugger, J.; Buser, R. A.; de Rooij, N. F. *J. Micromech. Microeng.* **1992**, *2*, 218.
(397) Fuji, T.; Watanabe, S.; Suzuki, M.; Fujiu, T. *J. Vac. Sci. Technol., B* **1995**, *13*, 1119.
(398) Minne, S. C.; Yaralioglu, G.; Manalis, S. R.; Zesch, J.; Atalar, A.; Quate, C. F. *Appl. Phys. Lett.* **1998**, *72*, 2318.
(399) Minne, S. C.; Adams, J. D.; Yaralioglu, G.; Manalis, S. R.; Atalar, A.; Quate, C. F. *Appl. Phys. Lett.* **1998**, *73*, 1742.
(400) Rugar, D.; Zuger, O.; Hoen, S.; Yannoni, C. S.; Vieth, H.-M.; Kendrick, R. D. *Science* **1994**, *264*, 1560.
(401) *Chem. Rev.* **1997**, *97*, 2463−2706.
(402) Nyffenegger, R. M.; Penner, R. M. *Chem. Rev.* **1997**, *97*, 1195.
(403) Kenseth, J.; Jones, V.; Porter, M. Unpublished results.
(404) Resch, R.; Baur, C.; Bugacov, A.; Koel, B. E.; Madhukar, A.; Requicha, A. A. G.; Will, P. *Langmuir* **1998**, *14*, 6613.

CR9801317